



**THERMALLY ACTIVATED, VARIABLE BLAZED GRATING FOR  
COHERENT BEAM STEERING**

THESIS

Matthew T. Johnson, First Lieutenant, USAF

AFIT/GEO/ENG/07-04

**DEPARTMENT OF THE AIR FORCE  
AIR UNIVERSITY**

***AIR FORCE INSTITUTE OF TECHNOLOGY***

---

---

**Wright-Patterson Air Force Base, Ohio**

APPROVED FOR PUBLIC RELEASE; DISTRIBUTION UNLIMITED

The views expressed in this thesis are those of the author and do not reflect the official policy or position of the United States Air Force, Department of Defense, or the U.S. Government.

AFIT/GEO/ENG/07-04

**THERMALLY ACTIVATED, VARIABLE BLAZED GRATING FOR  
COHERENT BEAM STEERING**

THESIS

Presented to the Faculty

Department of Electrical and Computer Engineering

Graduate School of Engineering and Management

Air Force Institute of Technology

Air University

Air Education and Training Command

In Partial Fulfillment of the Requirements for the

Degree of Master of Science in Electro-Optics

Matthew T. Johnson, BSEE

First Lieutenant, USAF

March 2007

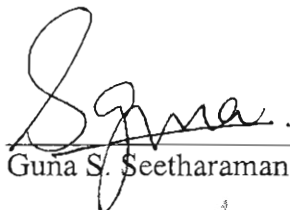
APPROVED FOR PUBLIC RELEASE; DISTRIBUTION UNLIMITED

**THERMALLY ACTIVATED, VARIABLE BLAZED GRATING FOR  
COHERENT BEAM STEERING**

Matthew T. Johnson, BSEE

First Lieutenant, USAF

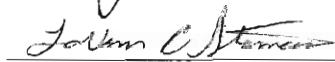
Approved:



Guna S. Seetharaman, PhD (Chairman)

5 MAR 07

Date



LaVern A. Starman, PhD, Maj, USAF (Member)

5 Mar 07

Date



Michael A. Marciniak, PhD (Member)

5 Mar 07

Date



Edward A. Watson, PhD (Member)

5 Mar 07

Date

## **Abstract**

The ability to perform non-mechanical optical beam steering is of critical importance in laser communication and remote sensing; it is as vital as a phased-array antenna is for RADAR. Directed energy transmission and direction-selective reception increase performance and produce tactical advantage in DoD applications. However, specific geometric features of non-mechanical beam steering devices must be designed in proportion to the wavelength of the monochromatic light to be steered. Also, the ability to handle higher energies by reducing the energy per unit requires large areas of uniform properties on the micrometer scale. These challenges have been addressed in the past using liquid crystals (LC) to produce a peak steering angle of 4 degrees, albeit limited by problems due to the fringing field effect. Recent advances in micro-fabrication techniques, including the synthesis and manipulation of certain electro- and thermo-optic materials, hold new opportunities for efficient beam steering solutions.

The objective of this thesis research is to demonstrate thermally controllable beam steering, and enable further investigation of efficiency and response time and their dependence on geometry. The design, fabrication and performance of such a thermally-activated, non-mechanical beam steering device is demonstrated for the first time herein. The elastomeric media, polydimethylsiloxane (PDMS), was used as the active, phase-controlling agent. Its temperature-dependent index of refraction was employed in a reflection-mode device by depositing it on a stair-step-approximated, blazed grating. The

periodic nature of the device contains the reflected beam within discrete, angular orders. The proof-of-concept device is modeled, tested and analyzed to explain its observed performance. Angular control of up to 1.2 degrees has been experimentally demonstrated. This approach promises simplicity of design and fabrication without the fringing field affect of LCs, allowing larger, discrete angular control. Moreover, the underlying fabrication is less expensive and can more easily be scaled to larger areas.

## **Acknowledgments**

First and foremost I would like to thank my loving wife for supporting me at home and enduring all the evenings and Saturdays I spent at school instead of with her and our daughter. I would also like to express my sincere appreciation to my advisor, Dr. Guna Seetharaman, for his many ideas, guidance, and teaching not only on this thesis effort, but on how to effectively research and contribute in the technical field.

I would like to thank Maj LaVern Starman for providing my optical equipment and funds for the photoresist mask and gold, and Dr. Marciniak for lending me what is possibly the best ‘office’ I will ever have. Similarly, I would like to express my gratitude to Dr. Bunning, Dr. Natarajan and Mr. Tondiglia from AFRL/MLPJE for graciously providing me the key material of this investigation, polydimethylsiloxane (PDMS), and for access to and help with their laboratory facilities. Thanks also to Maj Kading for patiently training and assisting me with the electron beam evaporator. Lastly, I would like to thank Capt Glauvitz and Lt Allard for their time and energy given in listening to my ideas and helping me think through them on the white board.

Matthew T. Johnson

## Table of Contents

	Page
Abstract.....	iv
Acknowledgments.....	vi
Table of Contents.....	vii
List of Figures.....	ix
List of Tables .....	xv
I. Introduction .....	1
1.1 Chapter Overview.....	2
1.2 Background.....	2
1.3 Liquid Crystals .....	4
1.4 Polydimethylsiloxane .....	7
1.5 Research Focus.....	8
1.6 Summary.....	9
II. Background .....	10
2.1 Chapter Overview.....	10
2.2 Theory.....	10
2.3 Literature Review .....	18
2.4 Summary.....	30
III. Fabrication .....	31
3.1 Chapter Overview.....	31
3.2 Design.....	31
3.3 Fabrication.....	34
3.4 Measurements.....	46
IV. Modeling/Experimental Setup .....	50
4.3 Experimental Setup .....	58
4.4 Summary.....	61
V. Results and Analysis .....	62
5.1 Chapter Overview.....	62
5.2 Initial Modeling Results .....	62
5.3 Experimental Results.....	67
5.5 Summary.....	72
VI. Conclusions and Future Work .....	75



6.1 Chapter Overview.....	75
6.2 Achievements .....	75
6.3 Recommendations for Future Work .....	76
6.4 Summary.....	85
Appendix A: Mask Design.....	87
Appendix B: MATLAB <sup>®</sup> Code.....	89
Appendix C: Alternative Fabrication Method and Results.....	93
Appendix D: Modeling and Experimental Results of the 5x25 Sample .....	97
Appendix E: Temperature-Variance Modeling .....	99
Bibliography .....	102
Vita .....	107

## List of Figures

	Page
Figure 1. Beam steering shown by constructive interference and wavefront tilting through an angled phase shift (cyan prism). (A) The phase front from the triangle point slightly lags that of the circle point, causing constructive interference along the red arrow. (B) Ray 2 lags ray 1 by a phase $\phi$ . Their OPL difference is then $\lambda\phi/2\pi$ , which changes the wavefront angle and direction of propagation. ....	3
Figure 2. (A) LC birefringence where $n_o$ is the fast axis, $n_e$ the slow axis and $\theta$ the angle from the direction of propagation to the fast axis. (B) Plot of $n_{eff}$ vs. $\theta$ for $n_o = 1.49$ and $n_e = 1.65$ on the right. ....	4
Figure 3. (A) Side view of LC device in ‘off’ and ‘on’ states. (B) The phase shift is controlled by the magnitude of the RMS voltage applied [6]. ....	5
Figure 4. Voltage profile (black stair-step) vs. actual phase profile (solid blue) [6]. The dashed red line lines surround the undesired flyback region. ....	6
Figure 5. A PDMS prism used for beam steering. Its index of refraction decreases with temperature, steering the ray a distance $\Delta y$ when heated [12]. ....	8
Figure 6. The $\xi$ and transmittance, $t_A$ , axes are defined at the aperture plane. The $x$ and intensity, $I$ , axes are defined at the detection plane. ....	11
Figure 7. Normalized intensity vs. angle for (A) $\psi = 2\pi/25 \mu\text{m}$ (phase shift/period) and (B) $\psi = 3\pi/25 \mu\text{m}$ with $\lambda = 632.8 \text{ nm}$ . The dashed green line shows the far-field Fraunhofer diffraction pattern for a single period ( $25 \mu\text{m}$ ). The dotted blue line shows the interference pattern for 10 periods, and the solid red line shows the combined far-field intensity. (C), (D) The same information is plotted to show the exaggerated steering angles. Coded in Mathcad <sup>TM</sup> . ....	13
Figure 8. Wavefronts from a multiple-slit diffraction aperture are shown to constructively combine in the zero (A), first (B) and second (C) order direction [16]. ....	14
Figure 9. (A) Unfolded phase profile for the design wavelength and for a larger wavelength where the reset phase difference is less than $2\pi$ . (B) The flyback region, $\Lambda_F$ , is due to the space needed to reset the phase [2]. ....	16
Figure 10. Stair-step design to approximate a continuous phase gradient [20]. ....	17

Figure 11. (A) Beam steering concept for a transmission-mode LC phased array. Voltages are applied at transparent electrodes to adjust the wavefront phase profile in steps. (B) Beam steering results (expanded to show Gaussian profile) for first-order diffraction using periods of $\infty$ , 16, 8 and 4 electrodes, corresponding to the superimposed beam profiles from left to right [25].	21
Figure 12. LC transmission-mode blazed grating beam deflector. The LC index is electrically controlled to match the PMMA (ON) for no diffraction, or contrast with the PMMA (OFF) for first-order diffraction. A stack of two layers is shown to provide 4 discrete steering angles [27].	22
Figure 13. Lightconnect's diffractive MEMS concept. (A) In the 'OFF' state, the incident light is equally reflected off the Al micromirror array and Al-coated substrate. The total path difference is $2\lambda$ , so the beams constructively interfere in the 0 <sup>th</sup> order direction. (B) In the 'ON' state the micromirrors are deflected down by $\lambda/4$ . The light reflected off the substrate is then $\lambda/2$ out of phase with that reflected off the micromirrors, causing light to be diffracted to the first orders [32].	24
Figure 14. (A) The GLV <sup>TM</sup> works much like Lightconnect's variable optical attenuator. (B) A polychromator with individually addressable electrodes to select the diffracted wavelength [34].	25
Figure 15. (A) MEMS OPA with tunable period. The comb actuators stretch the grating period while the leaf springs (B) allow the deformation [37].	26
Figure 16. (A) Architecture for creating and 2D wavefront control. (B) Electrically addressed spatial light modulator (EASLM) pixilation without the Fourier filter. (C) With the filter, the high-frequency components of the pixilation are negated. The result is a smoothed profile for activation of the optically addressed spatial light modulator (OASLM) [14].	28
Figure 17. Optical phased arrays cascaded in the AZ and EL direction [6].	28
Figure 18. Continuous, wide-angle, beam steering methods. (A) A coarse-steering holographic glass plate is sandwiched between two fine-steering LC devices. (B) The angle from a fine-steering, LC device is amplified by multiple, polarization-dependent, birefringent prisms [6].	30
Figure 19. (A) At room temperature the PDMS forms an even layer on top of the step profile. The steps are offset by integer multiples of $\lambda$ to guide the beam into the zero order. (B) As the sample is heated, the PDMS is expected to expand more where it is thickest. The phase shift over each	

step would then increase linearly, allowing higher order diffraction at increasing temperatures.....	34
Figure 20. (A) Multiple layers for an LCD display [43] vs. (B), the relatively simple design for a thermally controllable VBG. ....	35
Figure 21. Metal deposition process. Layers of LOR3A™ and 1805 photoresist are deposited, exposed and developed. The deposited metal is left only at the desired location after the lift-off procedure [43]. ....	36
Figure 22. Deposition of second metal layer. (A) The LOR and PR are deposited and exposed to the second-step pattern. (B) The sample is developed. (C) The metal is deposited and lifted off where the PR remains, leaving the second step. ....	37
Figure 23. (A) If the LOR3A™ layer is not thick enough, the metal layer above the 1805 PR will contact the layer on the substrate. The metal will adhere to the substrate and not lift off. (B) If the LOR3A™ layer is not developed long enough, a thin layer could remain under the metal. In this case, all of the metal will be lifted with the LOR3A™. ....	39
Figure 24. Chrome mask for photolithographic patterning of VBGs. A close up of the 12 <sup>th</sup> array pattern is shown on the right with numbering and alignment markers on the corners (mask details in Appendix A). ....	41
Figure 25. 10x50 sample before the final metallization. The final metal layer will be deposited in the bright yellow spot, where the resist has been developed and the gold surface is exposed. ....	42
Figure 26. Line quality of 2 μm lines at a 10 μm period. The 30-second development shows slight roughness on the edges. The 45 second development shows better line quality, but the line width is slightly decreased due to the slow, unwanted development of the sidewalls. The 60-second development shows gaps where the LOR3A™ was undercut beneath the 1805. ....	43
Figure 27. Samples after metallization and agitation in ACE. Successful (A), unsuccessful (B) and partially successful (C) results (100x zoom). ....	45
Figure 28. Cross-sectional view of three samples combined. The heights show the average of six measurements for each step. Data taken from Zygo® interferometer. ....	47
Figure 29. Top view with step width measurements for three samples. Images taken from SEM. ....	48

Figure 30. (A) A good array of seven periods is circled in the 5x25 sample. (B) The laser beam was focused to this area (view from top right) during testing. The usable area was approximately 150 $\mu\text{m}$ wide for all samples.....	49
Figure 31. Conformal fill of PDMS. The top of the PDMS is shown slightly conformed to the edges of the top gold step. Modeling in Coventorware®.....	52
Figure 32. (A) Temperature model of gold layer on top of heated substrate. The temperature variance is less than 0.1°. (B) The top of the PDMS is heated to only 193 °C when the gold is heated to 200° C. Modeling in Coventorware®.....	53
Figure 33. The width and spatial separation of each step for different samples (not to scale). Note that certain steps in the 10x50 and 5x25 samples are modeled in the flyback region as well. Widths correspond to the SEM measurements shown in Figure 29. Modeled in MATLAB® and combined.....	57
Figure 34. Setup one. The laser beam is focused towards the desired spot on the sample, which is laying on a hot plate. The light is diffracted off into different orders, each of which is diverging. The intensity in each order is then determined by the power detector as the hot plate temperature is increased.....	58
Figure 35. The beam is incident normal to the x axis and at the angle $\theta$ between the z and y axis. The reflected beam is diffracted at multiples of angle $\theta_{\text{order}}$ between the z and x axis.....	59
Figure 36. Setup two. The diverging beams are sent through lens 2 to converge towards the CCD camera. ....	60
Figure 37. Far-field diffraction pattern modeled for the two samples at 20 °C. The angular intensity is shifted towards the negative first order for both.....	63
Figure 38. Far-field diffraction pattern modeled for the three samples at 199 °C. The intensity shifts slightly to the right at a higher temperature due to the negative value of $\beta_{\text{PDMS}}$ . ....	64
Figure 39. A side view of the 10x30 and 10x50 diffraction pattern across the $y = 0^\circ$ line modeled at 20 °C. Three subsidiary maxima are shown between the zero and negative first orders for the 10x30 sample, and one for the 10x50. This correctly corresponds to the number of periods modeled for each (five and three).....	65

Figure 40. The modeled beam profiles of the 10x30 and 10x50 samples are shown across the x-axis when directed into the negative first order. They are modeled for ideal widths and heights (A), ideal heights and actual widths (B), and actual heights and widths (C). The dotted lines in part A show the region of integration for calculating the intensity in the negative first order. ....	66
Figure 41. Experimental results of setup one for the 10x30 (A) and 10x50 (B) sample. Both samples appear to start near the zero-order at 25 °C, and shift towards the first-order angle as the temperature increases. ....	68
Figure 42. (A) Beam profile of reflection off the 10x30 sample at 20 °C. It is confined mainly to the zero order. (B) At 199 °C, the beam is partially shifted to the first order angle of 1.26°. (C) Far-field intensity model of the 10x30 sample with $n_{\text{PDMS}} = 1.29$ and $\beta_{\text{PDMS}} = -0.00012 \text{ } ^\circ\text{C}^{-1}$ at 20 °C and (D) 199 °C. These models correspond well with the experimental beam profiles shown in A and B. ....	71
Figure 43. (A) Beam profile of reflection off the 10x50 sample at 20 °C. It is initially between the zero and first order. (B) At 199 °C, the majority of the beam is shifted to the first order angle of 0.75°. (C) Far-field intensity models of the 10x50 sample at 20 °C and (D) 199 °C with $n_{\text{PDMS}} = 1.29$ and $\beta_{\text{PDMS}} = -0.00012$ . These models correspond well with the experimental beam profiles shown in A and B. ....	72
Figure 44. Data and error bars used for a previous determination of $\beta_{\text{PDMS}}$ are shown in black [12]. The dashed red line shows the experimentally-determined $\beta_{\text{PDMS}}$ value falls within the error bars of the previous research. ....	74
Figure 45. (A) Cross section showing a PDMS layer fabricated to align with the top part of the blazed grating. (B) Upon heating the PDMS would expand more where it's thicker, allowing $\alpha_{\text{PDMS}}$ to factor into the OPL equation. ....	78
Figure 46. Beam condensing methods. A dual lens system (A) and anamorphic prisms (B). ....	79
Figure 47. Thick PDMS layers are surrounded by isolated Joule-heaters on three sides, maximizing the dynamic response. ....	81
Figure 48. (A) Transmission spectrum of PDMS [53]. (B) Radiated heating of the PDMS layers by diffractive gratings. The red radiation is incident on more slits, so it creates a tighter fringe pattern. ....	82
Figure 49. Replication of microchannels in PDMS using a Si master [58]. ....	84

Figure 50. Alternative fabrication method. Metal is deposited on top of the patterned PR. The metal is left and another layer is added for the next step. ....	93
Figure 51. Microscope pictures before the second metallization step. Although the periods matched, the 5K zoom shows the sample was not aligned exactly in the x and y directions. The 100x zoom shows good alignment for the second step, with the new 1818 PR layer covering half of the first-step mesa.....	94
Figure 52. Step profile of 5x15 (blue) and 10x30 (magenta) samples fabricated using the alternative method. Because the Zygo ® interferometer was not able to capture the entire profile at this small scale, the expected profile is added (lighter colors). ....	94
Figure 53. Experimental intensity measurements from the 10x30 sample, fabricated with the alternate method. There is a shift towards the negative third order with increasing temperature.....	95
Figure 54. Experimental results of setup one for the 5x25 sample. The intensity seems to be a little towards the first order at 20 °C, then shifts slightly towards the negative first order with increasing temperature. ....	97
Figure 55. Beam profile of reflection off the 5x25 sample at 20 and 199 °C.....	98
Figure 56. (A) Mesh model for 10x50 sample. (B) Model of temperature gradient when the substrate is heated to 473 °K (200 °C). The black arrows show where the temperature gradient was extracted for calculation of the OPL through each step. Modeled in Coventorware™.....	99
Figure 57. The temperature vs. height (z) from the gold bottom is shown for each step. ....	100
Figure 58. (A) The far-field intensity pattern modeled when the temperature gradient is included and (B) when a constant temperature is used. A slightly decreased steering angle of the envelope function is shown when the temperature gradient is included. ....	101

## **List of Tables**

	Page
Table 1. Fabrication processes.....	35
Table 2. LOR3A™ thickness and deviation averages. ....	38
Table 3. PDMS material properties [41], [48]. ....	51
Table 4. MATLAB® coding parameters and definitions. ....	55
Table 5. Calculated and modeled efficiencies for diffraction into the first order.....	67
Table 6. Efficiencies in each order at different temperatures. ....	73



# **THERMALLY ACTIVATED, VARIABLE BLAZED GRATING FOR COHERENT BEAM STEERING**

## **I. Introduction**

Phased array technology was first used for rapid radar-steering in World War II. The military applications for this technology continue to present themselves, more recently in the visible/near-infrared spectrum. The benefits of this technology were recognized as early as 1971, when its potential for random access, high resolving power and extreme steering angle accuracy was noted in comparison to mechanical methods [1]. Further, optical phased array (OPA) technology enables a simple, lightweight and affordable means of steering and splitting coherent radiation.

There are several military applications for OPA technology: delivering laser beams to targets, long-range laser communications (lasercom), remote sensing (LADAR) and defensive infrared countermeasures. Moreover, OPAs can potentially be used for wavefront modulation in holographic imaging and adaptive optics (AO). Liquid crystal (LC) OPAs have been considered for use in LADAR since before 1995 [2] and are currently being developed into lasercom [3] and AO systems [4].

Current OPA technology is limited to a field of regard (FOR) of approximately four degrees for high efficiency. This limitation is caused by the minimum achievable period for LCs due to the ‘fringing field’ effect, which is discussed in more detail below. The proposed device offers a method of circumventing this affect, opening the potential to surpass the current state of the art limitations in non-mechanical beam steering.

The device presented is an OPA, but is classified more specifically as a variable blazed grating (VBG). This is because its phase gradient changes (with temperature) but its periodicity is fixed. The background, fabrication, modeling and characterization for this novel, thermally-controlled VBG will be discussed herein.

## **1.1 Chapter Overview**

This introduction chapter will briefly discuss some of the basic theory behind phased array beam steering. The basic operation of LC devices to achieve this affect is then presented, followed by a discussion of the device limitations. A basic outline of the scope and objectives of this thesis will then follow.

## **1.2 Background**

### ***1.2.1 Phased Array Beam Steering***

Phased arrays can be understood as operating on the principle of constructive interference or wavefront propagation as shown in Figure 1. A plane wave is incident upon an angled, higher index, transparent material, or prism. The spherical phase front from the triangle point then slightly lags that from the circle point because it travels a higher optical path length (OPL). The beams then constructively interfere in the direction of the red arrow, where their phase fronts match.

The same phenomenon can be explained as the prism linearly altering the wavefront of the incident plane wave as in Figure 1B. The wavefront can be understood as the surface of the incident radiation having the same phase, which would be perfectly

flat in a plane wave. The wave travels orthogonally to its wavefront, so the prism steers the beam by linearly altering its phase profile.

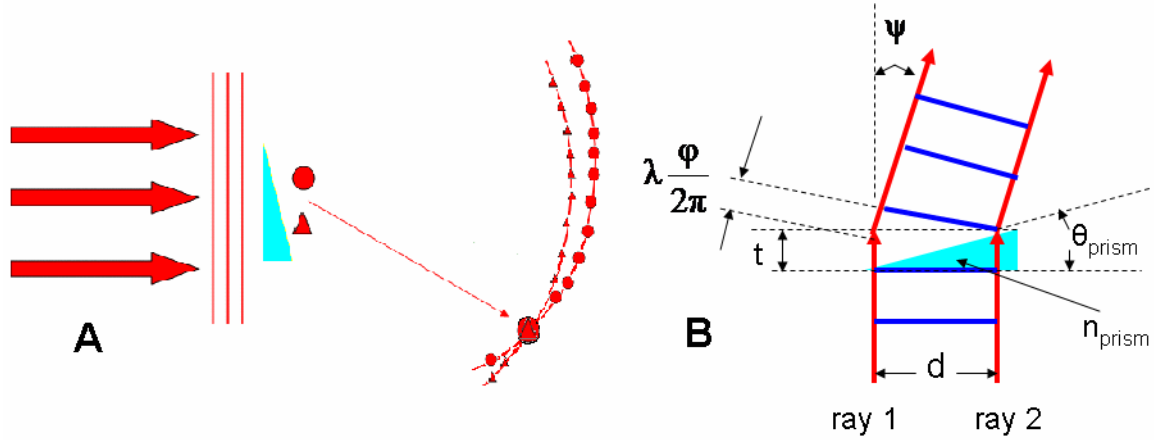


**Figure 1.** Beam steering shown by constructive interference and wavefront tilting through an angled phase shift (cyan prism). (A) The phase front from the triangle point slightly lags that of the circle point, causing constructive interference along the red arrow. (B) Ray 2 lags ray 1 by a phase  $\phi$ . Their OPL difference is then  $\lambda\phi/2\pi$ , which changes the wavefront angle and direction of propagation.

The steered angle,  $\psi$ , can be determined geometrically in various forms:

$$\psi = \sin^{-1}\left(\frac{\lambda\phi}{2\pi d}\right) = \sin^{-1}\left[\frac{(n_{\text{prism}} - 1)t}{d}\right] = \sin^{-1}\left[(n_{\text{prism}} - 1)\tan(\theta_{\text{prism}})\right] \quad (1.1)$$

where  $\lambda$  is the free-space wavelength (m),  $\phi$  is the phase lag of ray 2 with respect to ray 1,  $d$  is the distance between rays (m),  $n_{\text{prism}}$  is the prism index of refraction,  $t$  is the thickness increase of prism over  $d$  (m), and  $\theta_{\text{prism}}$  is the prism angle. As shown, the wavelength falls out of the equation. The steering angle of a prism is therefore constant for all wavelengths, assuming the dispersion coefficient ( $dn_{\text{prism}}/d\lambda$ ) is zero.

### 1.3 Liquid Crystals

The majority of phased array beam steering to date has been accomplished by exploiting the electrically controllable birefringence (index of refraction difference between molecular axes) of liquid crystals (LCs). Figure 2A shows the birefringence properties of LCs where  $n_o$  is the index of refraction along the fast axis,  $n_e$  along the slow axis and  $\theta$  the angle from the direction of ray propagation to the fast axis.

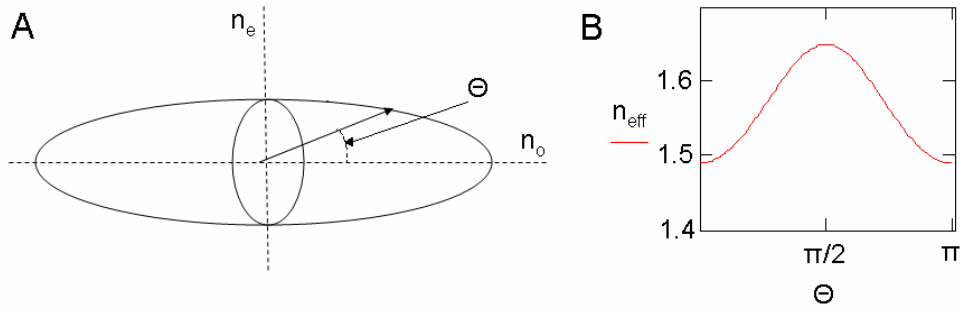


**Figure 2.** (A) LC birefringence where  $n_o$  is the fast axis,  $n_e$  the slow axis and  $\theta$  the angle from the direction of propagation to the fast axis. (B) Plot of  $n_{\text{eff}}$  vs.  $\theta$  for  $n_o = 1.49$  and  $n_e = 1.65$  on the right.

The ray propagation vector shows the exaggerated magnitude of the speed of light traveling through the LC in that direction, which is inversely proportional to the index of refraction. This is also shown in Figure 2B, where the effective index of refraction ( $n_{\text{eff}}$ ) is plotted against  $\theta$ . The molecular structure of LCs is essentially symmetric along the  $n_o$  and  $n_e$  axes, and longer along the  $n_e$  axis. This is why LCs are correctly displayed as rods instead of circles.

The key property of LCs that allows electrical control is their permanent dipole moment. This is due to the dielectric anisotropy,  $\Delta\epsilon$ , which is the difference between the dielectric constants along either axis ( $\epsilon_{\parallel} - \epsilon_{\perp}$ ) [5]. For example, a molecule with a

positive  $\Delta\epsilon$  value has a dipole moment along its slow axis,  $n_e$ , because  $\epsilon_{\parallel}$  is the dielectric constant in that direction. This property can be exploited to alter the effective OPL (or phase) as shown in Figure 3.

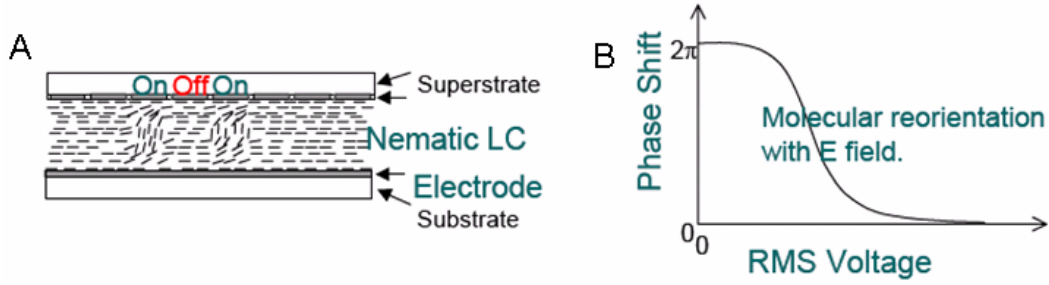


**Figure 3.** (A) Side view of LC device in ‘off’ and ‘on’ states. (B) The phase shift is controlled by the magnitude of the RMS voltage applied [6].

In the ‘off’ state, the OPL is greatest because  $n_{\text{eff}}$  is at its maximum value,  $n_e$ . In the ‘on’ state, the OPL is decreased because  $n_{\text{eff}}$  goes towards the  $n_o$  value over a portion of the device. The LCs are allowed to return to their original positions after the voltage is dropped because the ends of the device have been homeotropically aligned (by a rubbing or UV exposure procedure) to hold the LCs on the end in their position.

One of the major challenges with LC technology is reducing the time it takes for the LC to respond to an applied electric field. This response time has been found to increase by the square of the LC thickness. The minimum thickness to achieve a  $2\pi$  phase shift is set by the birefringence difference ( $n_e - n_o$ ) of the particular LC. To minimize the required thickness, LCs are often used in the reflective, rather than transmission mode. The effective OPL through the LC is then doubled for reflective mode due to the light traveling through the material twice. This allows the thickness of the LC to be cut in half, decreasing the response time by a factor of four.

### 1.3.1 Fringing Field Effect

Individually addressable elements on the order of half a wavelength are necessary for large-angle steering. This is relatively easier to achieve with microwave than optical systems. Where a typical high range resolution signal is on the order of one cm, the optical spectrum of 300-700 nm is about 20,000 times smaller! As stated, the major problem arising from scaling down LC elements to optical wavelengths is the fringing field effect. This affect serves to smooth the ramp within the period. This results in a desirable smoothing affect along the stair-steps, but it also smooths the transition between periods from the  $2\pi$  to 0 reset. This results in a flyback region, where the phase profile is sloped with the opposite blaze direction. This significantly detracts from the overall efficiency. An illustration of this effect is shown in Figure 4.

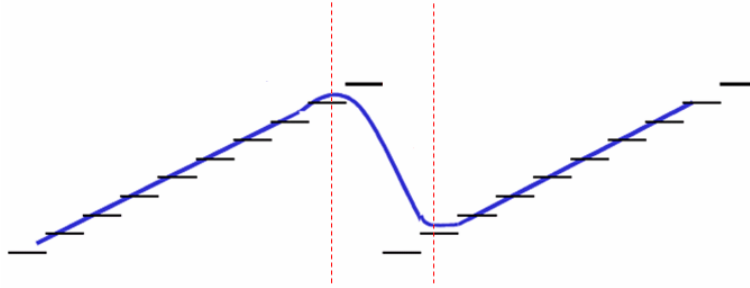


**Figure 4.** Voltage profile (black stair-step) vs. actual phase profile (solid blue) [6]. The dashed red line lines surround the undesired flyback region.

The fringing field affect can be reduced by decreasing the thickness of the LC layer, but the birefringence of the LCs determines the minimum thickness necessary to enable the maximum  $2\pi$  phase shift. The maximum birefringence of LCs combined with the fringing field affect then sets the minimum period-width, with which decent diffraction efficiency is possible.

### ***1.3.2 State of the Art***

Boulder Nonlinear System's spatial light modulator provides a good measure of the current state of the art in this technology [7]. The distance between addressable pixels (pixel pitch) on their 1 x 12,288 Linear Series model is 1.6  $\mu\text{m}$ . It can provide high-efficiency LC beam steering at periods no less than 10  $\mu\text{m}$ , which translates to a maximum steering angle of about 4° for optical wavelengths. Typical efficiencies for reflection-mode devices are in the range of 60-70% due to diffraction efficiency, reflectivity and fill factor [8].

Much larger steering angles are possible, but with a drastic cost in efficiency. For example, an LC device has steered a beam 47.6° by single-step addressing (on-off-on-off) of an OPA with a 6  $\mu\text{m}$  period. This angle was achieved in the 7<sup>th</sup> order; however, with an efficiency of only 2% [9].

Current LC beam steering technology does offer very precise angular control ( $6 \times 10^{-5}^\circ$  [8]), which is necessary for accuracy at high ranges. This precision is key for many military-related areas of interest; which is why NASA is currently integrating such technology into aerospace applications [10].

### **1.4 Polydimethylsiloxane**

Rather than LCs, the elastomeric media, polydimethylsiloxane (PDMS), is used as the active, phase-controlling agent. It is the most widely used and available silicon-based organic polymer [11]. It was initially chosen for its high rate of thermal expansion, but its temperature-dependent index of refraction ended up as the key parameter.

PDMS has been used for temperature-dependent beam steering on the macro-scale [12], as shown in Figure 5. The PDMS index of refraction decreases with increasing temperature. Its direction through and from the PDMS therefore changes, based on Snell's law, steering the beam. A similar concept, with the major exceptions of reflection-mode and micro-scale operation, is presented to achieve greater efficiency, control and response time.

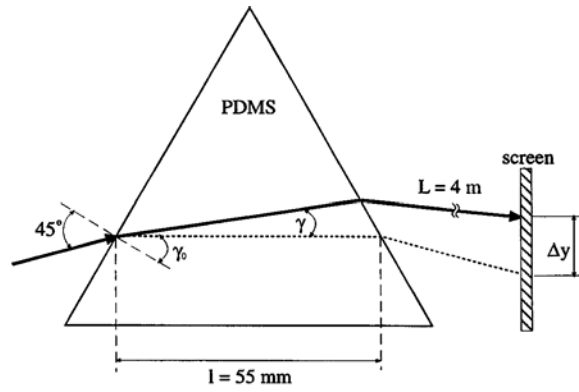


**Figure 5.** A PDMS prism used for beam steering. Its index of refraction decreases with temperature, steering the ray a distance  $\Delta y$  when heated [12].

### 1.5 Research Focus

This research is dedicated in part to addressing the limitations caused by the fringing field effect. The focus of the following research will be on the theory, fabrication, modeling and experimental characterization of a thermally-controlled VBG. Multiple, stair-step-approximated designs have been fabricated with varying step widths. The devices are modeled and optically tested to determine the intensity and efficiency in



the angular orders with varying temperature. Some figures of merit beyond the scope of this research include Joule/radiation heating and response time.

## **1.6 Summary**

In conclusion, this chapter has provided a brief refresher or introduction into the subject. Chapter II will focus on diffraction theory, a brief timeline of the major advances in OPA technology and the current state of the art. In Chapter III, the design, methods and results of the fabrication process will be discussed. The modeling and experimental setup will be presented in Chapter IV, followed by the results and analysis of both in Chapter V. Finally, Chapter VI will provide conclusions from this research, as well as recommendations for future work.

## II. Background

### 2.1 Chapter Overview

This chapter provides the background physics and historical setting of this research and its applications. The current state of the art in OPA beam steering is then reviewed. Common, non-diffractive beam steering methods, such as microlens arrays, Risley prisms and gimbaled micromirrors are not discussed.

### 2.2 Theory

OPA beam steering is governed by the constructive and destructive interference of light waves. This interference is best described mathematically by diffraction theory. Efficiencies can also be derived from the practical considerations of design and fabrication anomalies. The diffraction effects can be incorporated together, along with efficiency percentages, to obtain the theoretical far-field intensity.

#### *2.2.1 Diffraction*

If the actively reflecting/transmitting area of each element is understood as the transmittance function, diffraction theory can be applied to determine the overall interference pattern. The far-field diffraction affects from the element widths, phase shifting and periodicity is presented.

##### *2.2.1.1 Single Aperture Diffraction Pattern*

The far-field intensity pattern of a given transmittance function simplifies to its Fourier transform. The transmittance,  $t_A(\xi)$ , can be defined [13] for a rect function:

$$t_A(\xi) = \text{rect}\left(\frac{\xi}{a}\right) \quad (2.1)$$

where  $\xi$  is the aperture plane coordinate in the x-direction,  $a$  is the width, and the y-coordinate is irrelevant for one-dimensional arrays. This function defines a single rectangle with a transmittance of one across its width. This function is shown after convolution with an even-impulse pair,  $\delta(\xi \pm w/2)$ , in the left side of Figure 6.

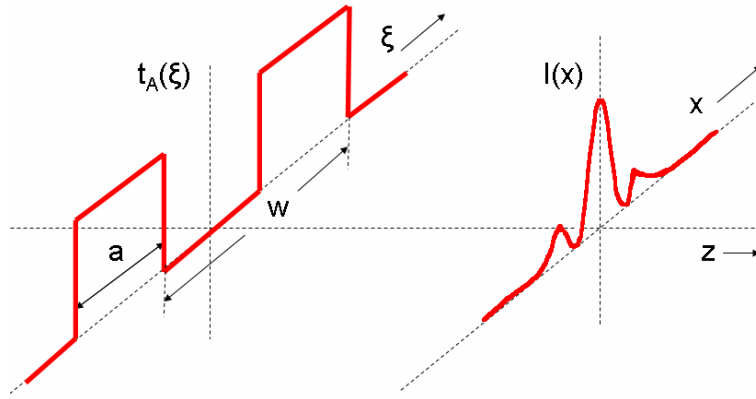


**Figure 6.** The  $\xi$  and transmittance,  $t_A$ , axes are defined at the aperture plane. The  $x$  and intensity,  $I$ , axes are defined at the detection plane.

The complex far-field amplitude,  $U(x)$ , can be determined by the Fraunhofer diffraction equation. This is assuming  $a$  is significantly larger than the free-space wavelength [14],  $\lambda$ , and the length along the direction of propagation,  $z$ , is sufficiently large [13]. It is based [13] on the transmittance function with an added phase component:

$$U(x) = \frac{e^{\frac{j2\pi z}{\lambda}} e^{\frac{j\pi}{\lambda z}(x^2)}}{j\lambda z} \mathcal{F}\{t_A(\xi)\}_{f_x = x/\lambda z} \quad (\text{V/m}) \quad (2.2)$$

where  $\mathcal{F}$  represents the Fourier transform with the  $f_x$  variable as defined. Solving the Fourier transform [13], the intensity of the field,  $I(x)$ , is the squared magnitude of the complex field:

$$I(x) = \frac{A^2}{\lambda^2 z^2} \text{sinc}^2\left(\frac{ax}{\lambda z}\right) \left(W/m^2\right) \quad (2.3)$$

where  $A$  is the aperture area (although the  $y$ -component is otherwise ignored). The phase terms of  $U(x)$  outside of the Fourier transform are excluded in equation 2.3 because  $I(x)$  is taken as the time average. This intensity pattern is shown graphically as the dashed green in Figure 7.

#### ***2.2.1.2 Phase/Spatial Shifting***

Since the aperture and far-field have a Fourier relation, a linear phase shift in the aperture results in a spatial shift in the far-field. This can be described [13] mathematically:

$$\mathcal{F}\{e^{j2\pi\psi x}\} = \delta(f_x - \psi) \quad (2.4)$$

where  $\psi$  is the linear phase shift coefficient and  $\delta$  is the Dirac delta function. The delta function shows that the resulting far-field is spatially shifted, proportionally to  $\psi$ .

Translating a linear phase shift at the aperture into the far-field intensity, equation 2.3 and 2.4 can be combined:

$$I(x) = \frac{A^2}{\lambda^2 z^2} \text{sinc}^2\left[a\left(\frac{\pi x}{\lambda z} - \frac{\psi}{2}\right)\right] \left(W/m^2\right) \quad (2.5)$$

This spatial shifting is illustrated in Figure 7B, as the single-aperture diffraction pattern (dashed blue line) is shifted farther for the higher  $\psi$  value.

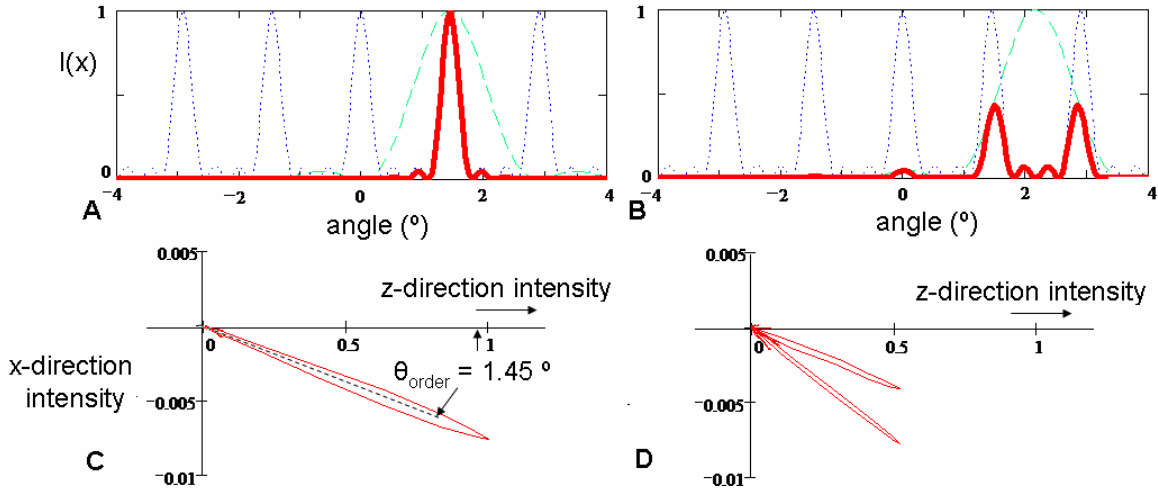


**Figure 7.** Normalized intensity vs. angle for (A)  $\psi = 2\pi/25 \mu\text{m}$  (phase shift/period) and (B)  $\psi = 3\pi/25 \mu\text{m}$  with  $\lambda = 632.8 \text{ nm}$ . The dashed green line shows the far-field Fraunhofer diffraction pattern for a single period ( $25 \mu\text{m}$ ). The dotted blue line shows the interference pattern for 10 periods, and the solid red line shows the combined far-field intensity. (C), (D) The same information is plotted to show the exaggerated steering angles. Coded in Mathcad™.

### 2.2.1.3 Multiple Aperture Interference

Now let us consider the effects of multiple apertures, separated by a period,  $w$ , as shown in Figure 6. The spatial offset for each period in the aperture plane is translated to a phase difference in the far-field due to the Fourier relation. The resulting interference sum of  $N$  periods is illustrated graphically in Figure 8 where  $N=5$ . It can be described mathematically [15] in the complex far-field:

$$U(x) = \frac{1 - e^{jN2\pi f_x w}}{1 - e^{j2\pi f_x w}} (\text{V/m}) \quad (2.6)$$

Using Euler's formula to translate the exponential into a trigonometric equation and squaring, the intensity is found [15]:

$$I(x) = \left[ \frac{\sin(N\pi f_x w)}{\sin(\pi f_x w)} \right]^2 (W/m^2) \quad (2.7)$$

Graphically, this is described by peaks at orders with angular separation,  $\theta_{\text{order}}$ :

$$\theta_{\text{order}} = \sin^{-1} \left( \frac{\lambda}{w} \right) \quad (2.8)$$

The peaks at these orders are represented by the dotted blue line in Figure 7. Higher  $N$  values provide sharper modal selection, as the lobe width for each peak is  $2\lambda/Nw$ . So  $\lambda$  determines the width of the Fraunhofer diffraction pattern,  $w$  and  $\lambda$  determine the angular separation of orders and  $N$  determines the angular confinement within those orders. Although  $\lambda$  does not affect the steered angle of the envelope function (dashed green line in Figure 7), it does affect the angular separation of orders when a periodicity is introduced into the aperture plane.

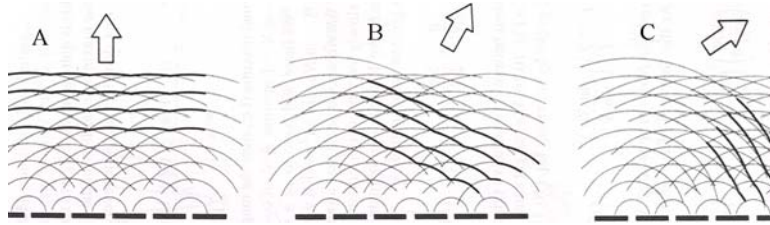


**Figure 8.** Wavefronts from a multiple-slit diffraction aperture are shown to constructively combine in the zero (A), first (B) and second (C) order direction [16].

#### 2.2.1.4 Combined Far-Field Pattern

Combining the aperture, linear phase-shift and array diffraction patterns, the intensity can be described:

$$I(x) = \frac{A^2}{\lambda^2 z^2} \text{sinc}^2 \left[ a\pi \left( \frac{x}{\lambda z} - \frac{\psi}{2\pi} \right) \right]^2 \left[ \frac{\sin(N\pi f_x w)}{\sin(\pi f_x w)} \right]^2 \quad (\text{W/m}^2) \quad (2.9)$$

This combined far-field pattern is shown as the solid red line in Figure 7 for an ideal, 10-period array where  $\psi = 2\pi/25$  and  $3\pi/25 \mu\text{m}^{-1}$ . When  $\psi = 2\pi/\text{period}$ , the single-period far-field pattern (dashed green line) is at its highest for the first order ( $1.45^\circ$  in this case), and its minimum for the other orders. The beam is steered entirely into the first order as shown by the solid red line in Figure 7A, given  $a = w$ . When  $\psi = 3\pi/\text{period}$ , however; the dashed green line has noticeable values at several orders. The beam is steered into these many orders, and the efficiency steered to any single order is significantly reduced.

The same combined diffraction pattern is also plotted in parts C and D of Figure 7. It is plotted in a polar,  $\log_{10}$  format according to the style preferred in antenna theory. The steered angle is exaggerated due to the exaggerated x-directional intensity axis.

### ***2.2.2 Practical Considerations***

The fundamental equations governing OPAs have been presented both mathematically and graphically. Some practical considerations from the design, fabrication and use of OPAs are now discussed.

#### ***2.2.2.1 $2\pi$ Reset Efficiency***

For practical fabrication, continuous phase profiles are rarely used. One exception is for very long range, high-precision laser steering when fine tuning of very small angles is desired; as in lasercom applications [17]. It thus becomes necessary to introduce resets at periods where the phase shift equals an integer multiple of  $2\pi$ .

One problem with introducing phase resets is that they are designed only for a specific wavelength. As shown in Figure 9A, there will be offsets in the wavefront for wavelengths that are not integer multiples of the design wavelength. These offsets effectively move the peak of the dashed green line shown in Figure 7 away from the blue, modal peaks. The resulting efficiency in the desired order is less, while the excess intensity is distributed into other orders.

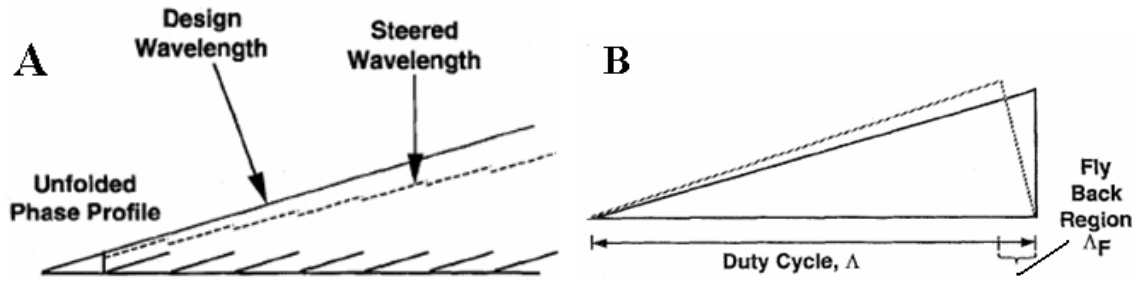


**Figure 9.** (A) Unfolded phase profile for the design wavelength and for a larger wavelength where the reset phase difference is less than  $2\pi$ . (B) The flyback region,  $\Delta F$ , is due to the space needed to reset the phase [2].

A given OPA using phase resets will therefore steer light most efficiently at the design wavelength, while diffracting different wavelengths into multiple orders. It should be noted; however, that several methods have been developed to steer broadband light with OPAs [18]. For example, the dispersion is decreased by designing the phase resets at integer multiples of the design wavelength ( $n\lambda$ ). As  $n$  increases, there are more wavelengths with integer multiples of the reset value, decreasing the dispersion.

#### 2.2.2.2 Flyback Region Efficiency

Diffraction effects also come into play when there exists a ‘flyback region’ or separation between the linear phase gradient, as shown in Figure 9B. The aperture size for each period is effectively reduced to  $\Lambda - \Delta F$ , where  $\Delta F$  is the width of the flyback



region and  $\Lambda$  is the period. The width of the far-field pattern for each period is therefore widened due to the Fourier relation, which allows diffraction into other, generally undesired, orders. Additionally, the light reflected from the flyback region goes in unwanted directions. The total flyback diffraction efficiency,  $\eta_\Lambda$ , can be approximated [19]:

$$\eta_\Lambda = \left(1 - \frac{\Lambda_F}{\Lambda}\right)^2 \quad (2.10)$$

A small flyback region is obviously desired, as larger values of  $\Lambda_F$  significantly reduce the efficiency. As mentioned earlier, minimizing this region has proven to be the major challenge for scaling down LC phased arrays.

### 2.2.2.3 Stair-step Efficiency

In an effort to design an approximately continuous phase profile, it is often most feasible to do so in incremental phase steps as shown in Figure 10.

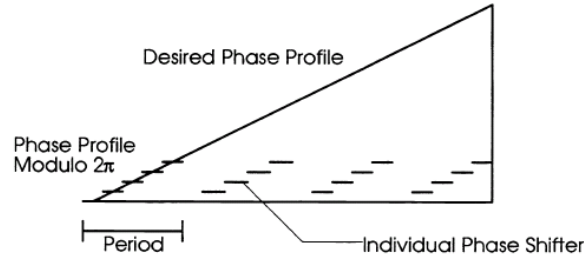


**Figure 10.** Stair-step design to approximate a continuous phase gradient [20].

This method is commonly used in LC beam steering, where each step represents a voltage-controllable pixel of the array. By expanding its periodic amplitude transmittance in a Fourier series, the stair-step diffraction efficiency is found [21]:

$$\eta_m = \text{sinc}^2\left(\frac{m\pi}{N}\right) \left[ \frac{\sin\left(\left[\frac{\phi}{2} - \pi m\right]\right)}{N \sin\left(\left[\frac{\phi}{2N} - \frac{\pi m}{N}\right]\right)} \right]^2 \quad (2.11)$$

where  $m$  is the order of interest,  $N$  is the number of steps and  $\phi$  is the phase change across each period. The first order efficiency,  $\eta_1$ , can be simplified [2]:

$$\eta_1 = \text{sinc}^2\left(\frac{\pi}{N}\right) \quad (2.12)$$

This concludes the theory section, much of which will be revisited in Chapter IV.

## 2.3 Literature Review

LC phase control has historically been the primary means of implementing OPA technology. A brief timeline of the significant advances in this technology will now be discussed. The state of the art of LC and other OPA-enabling technologies, such as diffractive microelectromechanical systems (MEMS) and coarse steering, will be presented next.

### 2.3.1 Early Years

The phased array concept was first exploited by Luis Alvarez for a rapidly-steerable radar system in World War II, and its applications have since led to several Nobel prizes [22]. Similarly, the applications of this technology to the visible spectrum are of much interest for military applications. This is shown by its research having been primarily led and funded by the Navy, Air Force, DARPA and NASA. The primary applications have been laser targeting, lasercom, LADAR and AO. One major difference between radar phased arrays and OPAs is that the latter are space-fed. Radar phased

arrays create and steer, while OPAs steer an already-formed beam by either transmission or reflection.

Phased array technology was first applied to the visible spectrum as early as 1971, when Meyer fabricated a 1-D OPA using LC phase shifting [23] for the Navy. The diffracted beam widths and steering angles agreed well with theory, and phased array beam steering was proven applicable to the visible spectrum. The experiment did have severe limitations though. The spacing was on the order of 0.5 mm, approximately 800 wavelengths, allowing a steering angle of only  $0.073^\circ$ . Although micro-manufacturing technology has come a long way since 1972, fabricating OPAs with periods less than a wavelength, as necessary for large steering angles, continues to be a challenge.

Another OPA approach was tested shortly after, demonstrating continuous steering using a different material, Lithium Niobate [2]. The benefits of OPA beam steering over the conventional, mechanical means were then acknowledged: random access, high resolving, extreme accuracy, fast response time and no shift of frequency as with acousto-optic deflectors [2]. Although the potential for OPAs was realized, the limited fabrication technology put further research off for two decades.

### ***2.3.2 The 90's***

The OPA technology of the 1990's continued to exploit LC birefringence. Much effort was being directed towards LC displays (LCDs) during this time. LCDs exploit the voltage-dependent polarization properties of LCs to achieve amplitude modulation for various colors, creating a two-dimensional (2D) image. Such a display was used to affect a discrete (stair-step) blazed grating phase ramp in 1994 [2]. The limited phase-

modulation range (up to  $1.3\pi$ ) and large spacing limited it to low efficiency and angle ( $<0.1^\circ$ ).

Although not very successful, the report does serve to demonstrate how the extensive R&D of LCDs has helped with the fabrication techniques and knowledge base for LC beam steering applications. Not the least of these developments was that of indium tin oxide (ITO) transistors. This transparent, colorless conductor offers the ability to control the electric field through the LC layer with minimal optical obstruction.

A blazed grating approach with LC beam steering was also shown in 1994 [24]. Rather than the usual stair-step approximation, a linear phase gradient using reflective LCs was achieved by operating in the linear voltage-phase region (see Figure 3B). The technique promised good steering angles (up to  $5^\circ$  in theory) owing to the smaller pixel spacing (as low as  $5\text{ }\mu\text{m}$ ). Its efficiency was improved due to the continuous phase ramp, but was still limited to 1-9% due to fabrication difficulties and the small region of linear voltage-phase relation.

A major design breakthrough was funded by the Air Force (Electro-Optics Division of the Sensors Directorate, Air Force Research Laboratory (AFRL), Wright-Patterson AFB, OH) and achieved in 1996 by Dorschner *et al.* [25]. A classic (stair-step) LC phase shifter was designed with small spacings ( $<10\text{ }\mu\text{m}$ ) and a near-unity fill factor to achieve performance approaching the theoretical diffraction limits. The fabrication process allowing the high fill factor was similar to that of LC displays, except with higher quality components. The design concept is shown in Figure 11A, where the applied voltages correspond to the nonlinear phase shifts desired for each step.

The experimental results showed higher efficiency than that allowed by the stair-step efficiency because there were no hard boundaries within the LC film. The index-shift was therefore not sharp across electrodes, making the phase profile more continuous than modeled. The different beam steering angles shown in Figure 11B were achieved by altering the number of electrodes per period.

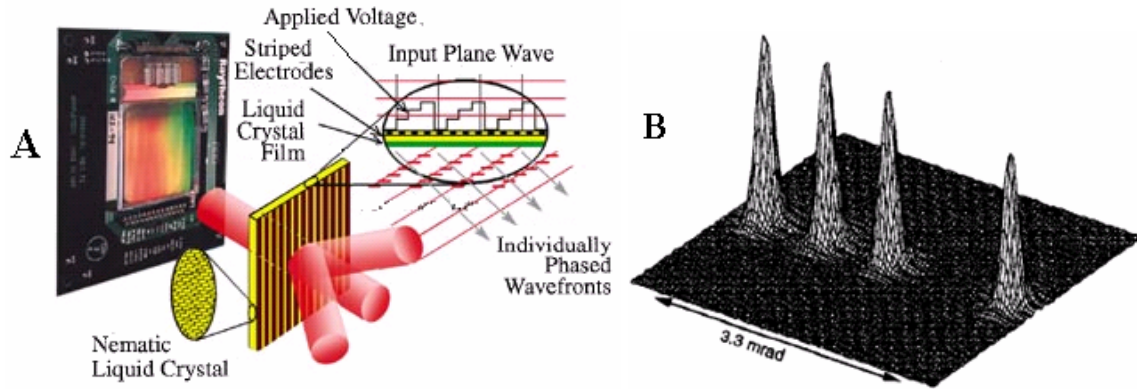


**Figure 11.** (A) Beam steering concept for a transmission-mode LC phased array. Voltages are applied at transparent electrodes to adjust the wavefront phase profile in steps. (B) Beam steering results (expanded to show Gaussian profile) for first-order diffraction using periods of  $\infty$ , 16, 8 and 4 electrodes, corresponding to the superimposed beam profiles from left to right [25].

The slightly decreasing peak values for the higher angles (shorter periods) are due to the flyback region becoming more pronounced for smaller periods, which is caused by the fringing field effect. Also, the stair-step efficiency is decreased for lower numbers of steps ( $N$ ) per period, as shown by Equation 2.12.

The next year, a VBG was demonstrated using micromirrors at the Air Force Institute of Technology [26]. This was the first MEMS VBG demonstrated. The device was fabricated using the 17th Multi-User MEMS Processes (MUMPs) run. It consisted

of an array of multiple mirrors whose tilt angle was electrostatically actuated. The tilt was adjusted to achieve diffraction into five orders (up to  $1.81^\circ$ ) with a maximum efficiency of 53%. The maximum diffraction order was limited only by the tilt angle, which was limited by the fabricated width : height ratio of the mirrors. The efficiency suffered due to the spacing between mirrors and the proportionally limited width of the reflective gold layer on top of the polysilicon mirrors. The device demonstrated a wide FOV, if not the widest, compared to other contemporary methods. The rigidity of its periodicity did; however, confine the reflected beam to five discrete steering angles.

A novel, transmission-mode design was demonstrated in 1998 with a blazed grating of the transparent material, poly-methyl methacrylate (PMMA). This grating was fabricated by a series of electron-beam lithography steps, etching away discrete sections one at a time [27]. An LC film was deposited on top of this grating, sandwiched by Indium Tin Oxide (ITO) electrodes and glass plates according to standard manufacturing processes (see Figure 12).

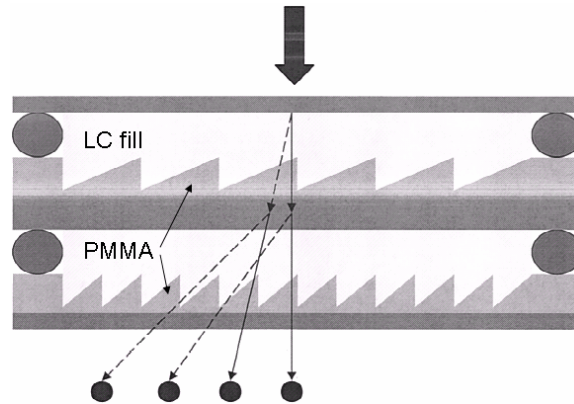


**Figure 12.** LC transmission-mode blazed grating beam deflector. The LC index is electrically controlled to match the PMMA (ON) for no diffraction, or contrast with the PMMA (OFF) for first-order diffraction. A stack of two layers is shown to provide 4 discrete steering angles [27].

The LC index of refraction is different from the PMMA in the ‘OFF’ state, resulting in strong first order diffraction with the correct grating parameters. In the ‘ON’ state, the LC index can be controlled to match the PMMA, negating the diffraction. Thus, the device acts as a binary switch to change the beam steering between the zero and first order. The device was modified in 2000 [28] and 2004 [29] by stacking four layers with different periods, enabling steering to 16 discrete directions. The periods of the additional layers are related proportionally by  $2^N$ , where N is the number of stacks, to enable operation at the same design wavelength.

The device proposed herein is most similar to this design. The major differences are the materials (PMMA and LC vs. gold and PDMS), activation (electrical vs. thermal) and mode (transmission vs. reflection).

### ***2.3.3 State of the Art in Non-Mechanical Beam Steering***

The scaling limitations of the promising LC beam steering technology, as discussed in Chapter I, were realized in the 21<sup>st</sup> century. For this reason, other mechanisms are necessary to magnify the angular limits of continuous steering. Currently, the state of the art for fine steering/switching control is achieved by LC devices and diffractive MEMS, while they must be combined with other coarse-steering mechanisms to achieve large angles.

#### ***2.3.3.1 Diffractive MEMS***

The limitations of LCs and their complex fabrication processes have led to the search for alternate means of achieving OPAs. Although MEMS have emerged only as recently as the 1980’s, they have demonstrated success and reliability in multiple and

various applications [30]. This is in part due to the mature, lithographic processes used in their fabrication.

Lightconnect has commercialized the MEMS OPA concept that was first conceived by the Stanford group in 1992 [31]. It currently packages the technology as variable optical attenuators and dynamic gain/channel equalizers. A diagram of the concept is shown in Figure 13.

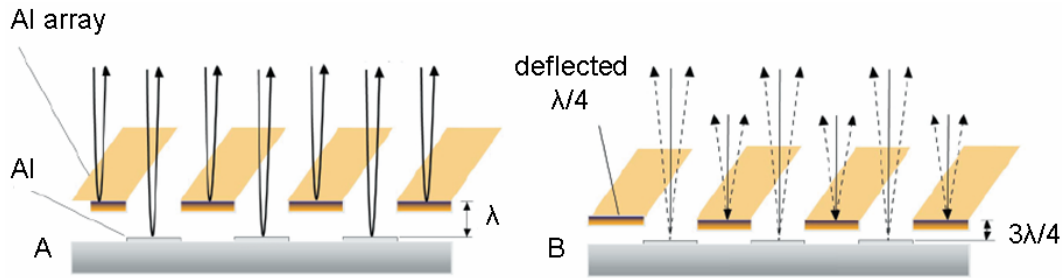


**Figure 13.** Lightconnect's diffractive MEMS concept. (A) In the ‘OFF’ state, the incident light is equally reflected off the Al micromirror array and Al-coated substrate. The total path difference is  $2\lambda$ , so the beams constructively interfere in the 0<sup>th</sup> order direction. (B) In the ‘ON’ state the micromirrors are deflected down by  $\lambda/4$ . The light reflected off the substrate is then  $\lambda/2$  out of phase with that reflected off the micromirrors, causing light to be diffracted to the first orders [32].

In the ‘OFF’ state shown in Figure 13A, the incident light is reflected off the Al micromirror array and the reference, Al-coated substrate. Freezing the lightwaves in time, the total path difference between the waves is  $2\lambda$ . The beams then constructively interfere in the zero order direction (straight reflection). In the ‘ON’ state shown in Figure 13B, the micromirrors are deflected down by  $\lambda/4$ . While the reference beam remains constant, the phase of the light wave reflected off the micromirror is shifted by  $\lambda/2$ . The two light waves are then  $\lambda/2$  out of phase, causing light to be diffracted into the



first orders. The OPAs function is then to switch an incident, coherent beam between the zero and first orders.

A very similar approach is taken by Silicon Light Machines, but it uses micromirrors for both the reference and variable reflected light waves as shown in Figure 14A. The grating light valve (GLV<sup>TM</sup>) has been highly marketed by Silicon Light Machines for its display applications, but has found use in blocking filters, dynamic gain equalizers and printers [33].

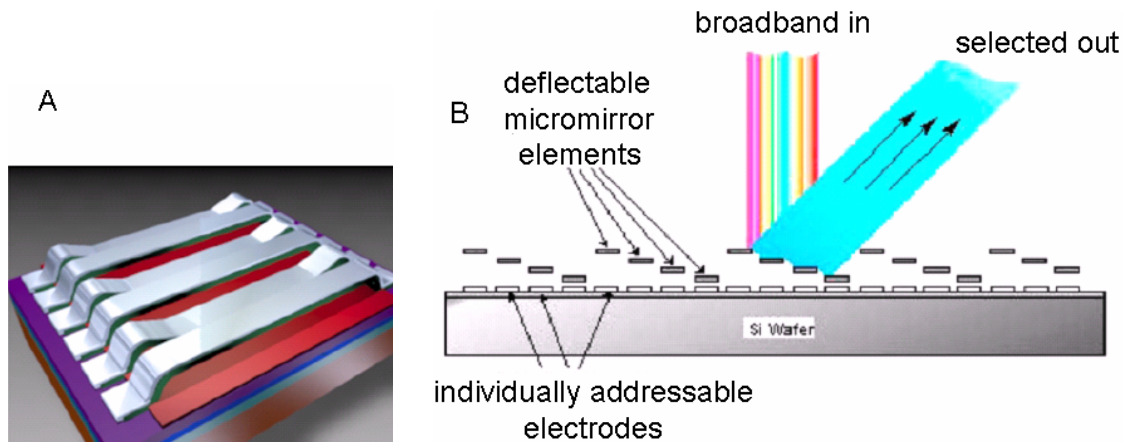


**Figure 14.** (A) The GLV<sup>TM</sup> works much like Lightconnect's variable optical attenuator. (B) A polychromator with individually addressable electrodes to select the diffracted wavelength [34].

The GLV uses the same binary-weighted pulse width light modulation for gray scale in display applications as Texas Instrument's digital micromirror device [35]. The major differences are that it is much faster (10 ns vs. 15  $\mu$ s for DMDs and 10 ms for LCDs), operates on a laser light source and uses a rapidly-scanned single row instead of a 2D matrix. The mirror ribbons have 0.5  $\mu$ m spacing and can be fabricated between 1-10  $\mu$ m wide with differing heights for operation at different wavelengths. The drawbacks of

this technology include the mechanical scanning, efficiency ( $\approx 70\%$ ) and the speckled image resulting from the coherent light source.

The polychromator operates in a similar way to function as a spectrometer. It was originally designed by a joint effort of Massachusetts Institute of Technology and Sandia National Laboratory [36] for distinguishing gaseous species. The individually addressable mirrors can be deflected at different heights to vary the blaze angle. The selected wavelength at which the phase shift equals  $2\pi$  per period is then efficiently diffracted in the specified direction.

While diffractive MEMS are generally confined to fixed periods by their fabrication, period-varying systems have recently been demonstrated. A free standing optical MEMS grating can be stretched by comb drives as shown in Figure 15 [37].

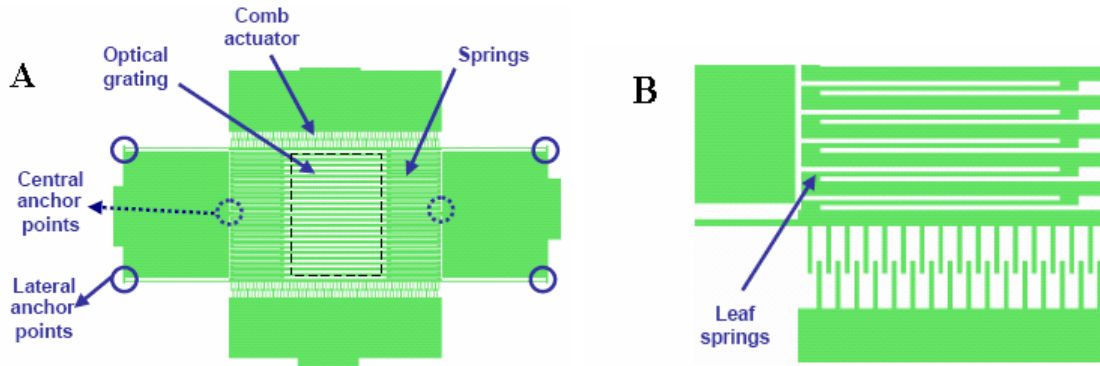


**Figure 15.** (A) MEMS OPA with tunable period. The comb actuators stretch the grating period while the leaf springs (B) allow the deformation [37].

When triggered, the comb actuators electrostatically pull the grating outward. The leaf springs are attached to the optical grating, central anchor points and the comb drive actuator. They act to absorb the stress and deformation of the stretching, allowing the optical grating to maintain uniformity while the period increases. The device was

able to achieve a 3% change in the period, allowing a spectral range of 150 nm centered at 5  $\mu\text{m}$ . The gratings are currently being modified to a blazed profile by use of an angled, dry-etching fabrication method. This is expected to improve the diffraction efficiency and allow operation at shorter wavelengths without scaling down the overall structure.

#### ***2.3.3.2 Steering in 2D***

While the previous methods shown have all been for one-dimensional beam steering, most applications require 2D. Such a system has been designed and tested by AFRL's Directed Energy Directorate [14] and is shown in Figure 16A. A laser is incident upon an electrically addressed spatial light modulator (EASLM), which controls the transmitted amplitude over each pixel. The beam is then transferred through a Fourier filter, which serves to negate its high frequency components. As shown in parts B and C of Figure 16, this smoothes the pixilation from the non-unity fill-factor of the EASLM.

The beam is then incident on an optically addressed spatial light modulator (OASLM). This consists of a photoconductive surface, which is sandwiched, along with the LC layer, between two AC-biased electrodes. The OASLM layer is optimized to provide a  $0 - 2\pi$  phase shift over the amplitude range (0 - 255) of the incident radiation pattern. For optimization, the EASLM control mechanism takes into account both the nonlinear phase response and the inherent aberrations of the OASLM.

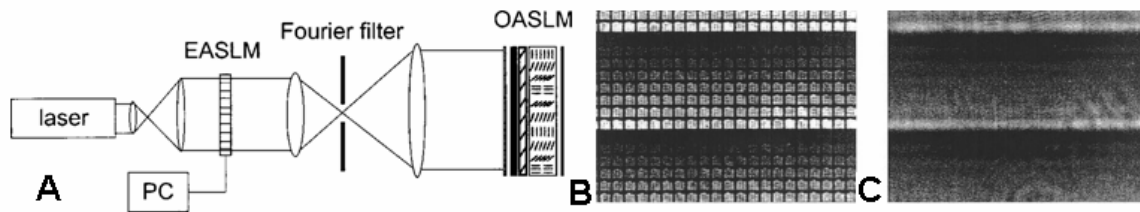


**Figure 16.** (A) Architecture for creating and 2D wavefront control. (B) Electrically addressed spatial light modulator (EASLM) pixilation without the Fourier filter. (C) With the filter, the high-frequency components of the pixilation are negated. The result is a smoothed profile for activation of the optically addressed spatial light modulator (OASLM) [14].

As shown in Figure 16B, a minimum of eight pixels is necessary for each  $2\pi$  reset to minimize the fringing field effect and ensure good efficiency. In this way, high-fidelity 2D wavefront control is accomplished with LC technology.

### 2.3.3.3 Stacking Single-Dimensional Control

Due to addressing constraints, it is sometimes more practical to steer beams one dimension at a time. If there were  $N$  rows and columns of small periods, it would be much more practical to address  $2N$  electrodes than  $N^2$  electrodes. A diagram of the currently preferred method is shown in Figure 17.

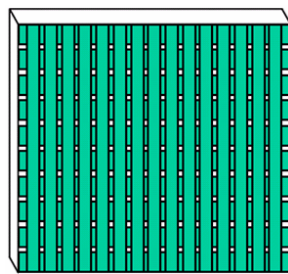


**Figure 17.** Optical phased arrays cascaded in the AZ and EL direction [6].

The concept works well for steering a single beam in a single, 2D direction; but becomes more difficult if the goal is to steer each pixel in a given 2D direction. This

could only be accomplished by time-division multiplexing or different methods of cascading.

#### ***2.3.3.4 Combining Fine and Coarse Steering***

As neither LC nor diffractive MEMS devices can yet provide continuous, high-efficiency, large-angle control, it becomes necessary to combine them with other methods to achieve this. The latest milestone came from Raytheon under the DARPA-sponsored Steered Agile Beams (STAB) effort. They demonstrated continuous, non-mechanical beam steering over a  $45^\circ \times 45^\circ$  field with an efficiency of 15-20% [6]. This was accomplished by sandwiching a coarse-steering holographic glass plate between two LC beam steering devices as shown in Figure 18A. The first fine-steering, LC device selects the holographic coarse steering direction, and the second one provides fine control within the coarse angles.

A similar approach was recently taken by Rockwell Scientific Company, also under the STAB effort, in which a  $\pm 20^\circ$  beam steering range was demonstrated. They employed an LC device for fine steering along with a series of prisms with polarization-dependent birefringence as shown in Figure 18. Each prism acts as a binary-steering mechanism with a controllable polarization rotator in front to choose which direction it steers.



## **III. Fabrication**

### **3.1 Chapter Overview**

This chapter presents an overview and details of the design and fabrication process. Each step is discussed with illustrations to aid in visualization of the process. Finally, the fabrication results are displayed and analyzed by various instruments: a microscope, Zygo® interferometer, scanning electronic microscope (SEM). An alternate fabrication method was performed and tested, which is presented in Appendix C.

### **3.2 Design**

The implemented design is similar to that of Xu Wang's shown in Figure 12, with the primary exception of the thermally activated material, polydimethylsiloxane (PDMS), used instead of LCs. This was chosen as the active material for its high thermal expansion rate, transparency and form. Its thermal expansion rate of  $310 \mu\text{m/m}\cdot\text{C}^\circ$  [38] is 20 times that of common rates, such as gold's. Its viscous, liquid form allows a simple, even deposition process with the ability to harden afterwards (when the curing agent is added).

#### ***3.2.1 Operation***

Multiple methods of fabricating blazed gratings through X-ray and electron-beam lithography have been presented in the literature [29], [39]. A photolithographic method was used instead to create a step-approximated blazed grating. This method was chosen to investigate the fabrication, modeling and optical response of discrete steps for related research [40].

The device was fabricated to achieve zero-order diffraction at room temperature, as shown in Figure 19A. The target thickness must then allow an integer multiple of wavelengths ( $\lambda$ ) to pass through PDMS at an off-perpendicular angle, at room temperature. The beam must be incident at an angle ( $\theta_{\text{incident}}$ ) to allow measurement of the reflection. The target thickness ( $t_{\text{target}}$ ) was then found:

$$t_{\text{target}} = \frac{m\lambda \cos(\theta_{\text{incident}})}{2n_{\text{PDMS}}} \quad (3.1)$$

where  $m$  is the integer number of wavelengths passing through the step-height OPL

The target thickness was calculated based on the AlInGaP wavelength of 660 nm, the room temperature index of refraction for PDMS ( $n_{\text{PDMS}} = 1.431$  [41]) and the incident angle of  $10^\circ$ . A planar fill of PDMS was also assumed, as shown in Figure 19A. The target thickness was found to be an integer multiple ( $m$ ) of 2,271 Å. Larger step heights were preferred for greater temperature sensitivity.

Based on preliminary calculations, a minimal step height was determined to allow the phase gradient to shift from one order to another within the temperature range of 20-200 °C. This height was 6813 Å ( $m=3$ ), but was experimentally found to be too large for the fabrication process. The target step height was then set to 4542 Å to allow an OPL of  $2\lambda$  for each step. Variations in step height, wavelength or  $n_{\text{PDMS}}$  will affect the phase gradient of the reflected beam. The phase difference across each step is a function of these parameters:

$$\Delta\Phi = 360 \times \text{mod} \left( \frac{2n_{\text{PDMS}} \text{height}}{\lambda \cos(\theta_{\text{incident}})} \right) \quad (3.2)$$



The mod function is used here to take the remainder of the equation, canceling out  $m$ . A greater step height (or smaller wavelength) is then expected to increase  $\Delta\Phi$  for each step, which increases the overall phase gradient of the reflected beam. This would effectively shift the reflected beam to the left, according to the view shown in Figure 19.  $\Delta\Phi$  is discussed specifically for the step-height variance in the measurements section of this chapter.

As the sample is heated, the PDMS is expected to expand more where it is thickest, as shown in Figure 19B. This is according [42] to the following equation:

$$\Delta L_{\text{PDMS}} = \alpha_{\text{PDMS}} \Delta T L \text{ (m)} \quad (3.3)$$

where  $\Delta L_{\text{PDMS}}$  is the length expanded,  $\alpha_{\text{PDMS}}$  is the thermal expansion rate in  $\mu\text{m}/\text{m}\cdot\text{C}^\circ$  and  $L$  is the original PDMS thickness. The expanded length is proportional to the original thickness. The possible change in  $\alpha_{\text{PDMS}}$  with temperature was not found in the literature. The phase shift over each step is then increased linearly with temperature, allowing diffraction into higher orders. Figure 19B shows the expected PDMS profile when heated to diffract into the first order. This occurs when the phase lead for each step is increased by  $72^\circ$ , or  $360^\circ/5$ .

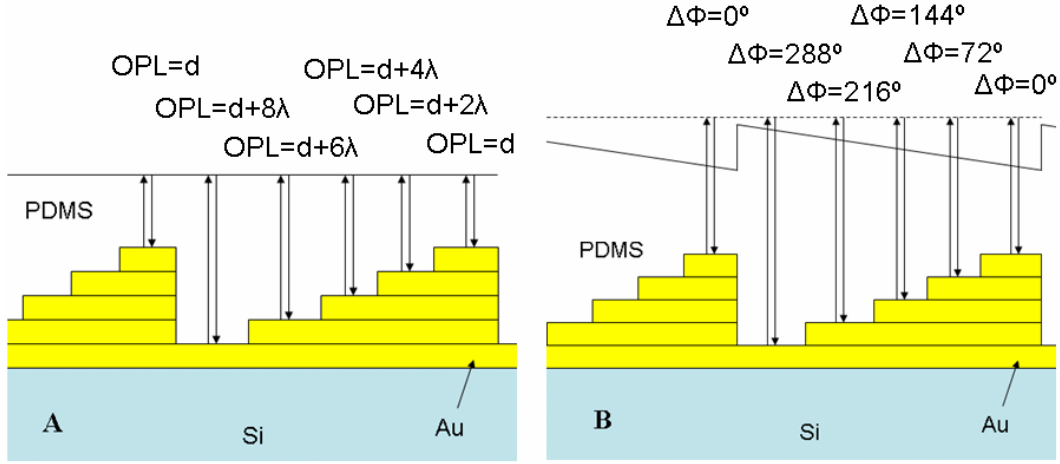


**Figure 19.** (A) At room temperature the PDMS forms an even layer on top of the step profile. The steps are offset by integer multiples of  $\lambda$  to guide the beam into the zero order. (B) As the sample is heated, the PDMS is expected to expand more where it is thickest. The phase shift over each step would then increase linearly, allowing higher order diffraction at increasing temperatures.

### 3.3 Fabrication

One of the significant advantages of the proposed thermally controlled VBG is the relative ease of its fabrication processes. Many steps were necessary, but they pale in comparison to standard LC device manufacturing processes: ITO transistor deposition, multiple depositions of silica on glass plates, rubbing to control alignment, glass substrates glued, LC insertion under pressure, lamination, *etc.* The multiple layers of an LCD are shown Figure 20A. These steps require bulky, expensive machinery and much time, but none of them are necessary for fabrication of the thermally controlled VBG (Figure 20B).

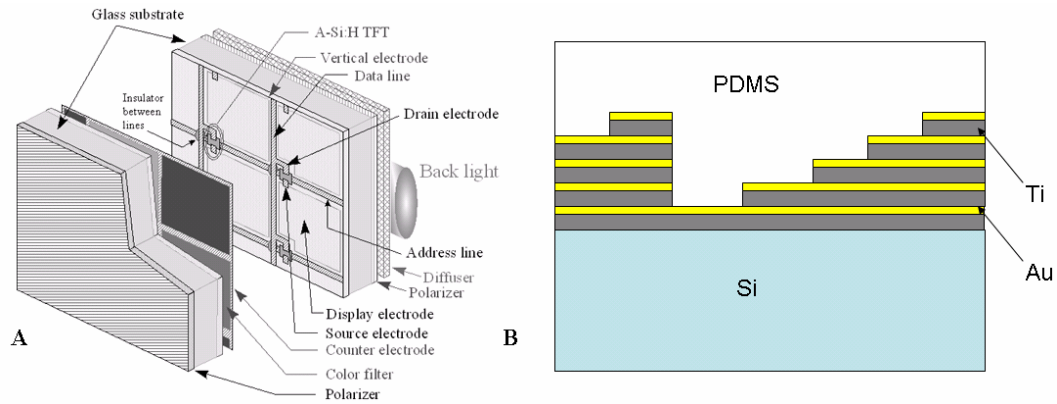


**Figure 20.** (A) Multiple layers for an LCD display [43] vs. (B), the relatively simple design for a thermally controllable VBG.

### 3.3.1 Process Overview

An overview of the photolithographic process for metal deposition is presented here. The process is broken apart into six major steps, as shown in Table 1 and Figure 21. This process was repeated from two to four times for the different step patterns. Each of these steps will be discussed in detail below, with the final, desired result shown in Figure 20B.

**Table 1. Fabrication processes.**

<b>Step</b>	<b>Process</b>
1	lift-off resist deposition
2	photoresist deposition
3	mask alignment/exposure
4	development
5	metal deposition
6	lift-off

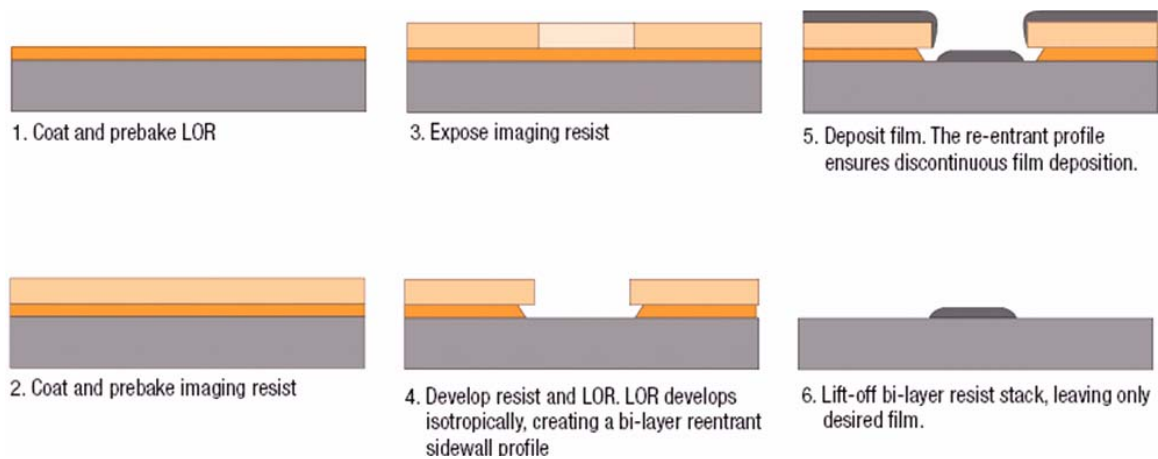


**Figure 21.** Metal deposition process. Layers of LOR3A™ and 1805 photoresist are deposited, exposed and developed. The deposited metal is left only at the desired location after the lift-off procedure [43].

The lift-off resist (LOR) and photoresist (PR) are first evenly deposited and baked dry (steps 1 and 2). The sample is then placed under a mask and exposed to UV radiation where the metal is to be deposited (step 3). Next, the sample is developed in a solution that releases the exposed imaging resist (step 4). The solution etches the LOR3A™ isotropically, creating a bi-layer reentrant sidewall profile. The metal is then evaporated onto the sample (step 5). The sidewall profile of the LOR allows a separation between the metal on the substrate and that on the PR as shown in Figure 21-5. The top layer is finally removed while the desired layer remains on the substrate (step 6).

A series of these processes must be performed in order to achieve the desired step profile. A cross-sectional view of such an additional process is illustrated in Figure 22, with an exaggerated z-scale (upward direction).

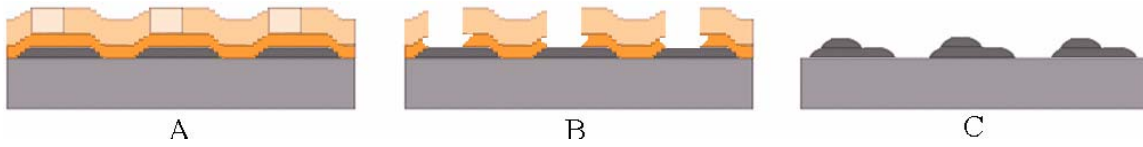


**Figure 22.** Deposition of second metal layer. (A) The LOR and PR are deposited and exposed to the second-step pattern. (B) The sample is developed. (C) The metal is deposited and lifted off where the PR remains, leaving the second step.

### ***3.3.2 Si preparation***

Before starting the processes described above, the Si samples were prepared. A 3” wafer was cut into 1¼-cm squares to fabricate separately. These were then cleaned with acetone, methanol and deionized water (DIW) before drying with Nitrogen. The samples were then taped on slides for insertion into the electron-beam evaporator (EBE).

The initial, bottom layer of titanium (Ti) and gold were then deposited on the samples. The thicknesses were 150 and 200 Å, respectively. Since Si and gold have different reflectivities, this initial deposition was to ensure the reflectance remained constant for each step across the device surface. In this case the Ti layer served as a bonding agent to aid the gold adhesion.

### ***3.3.3 Resist Deposition***

After cleaning, LOR3A™ (MicroChem) was deposited and spun to provide an even coating. The sample was then baked dry on a hot plate at 170 °C for two minutes. This cycle was repeated again for additional LOR3A™ layers. Next, 1805 PR (MicroChem) was deposited and spun at 4000 RPM for 30 seconds and baked at 100° C for one minute. This was in accordance with the standard recipe [44]. An important lesson here is the necessity of not straying far from the recommended baking temperatures and time. If either resist was heated too much or for too long, it would

often harden. This makes it resistant to the developing solution, which forbids the development process.

In order to ensure a clean lift-off (see Figure 21-5), the LOR3A™ layer should be thicker than the deposited metal. The LOR3A™ provider suggests it be 1.2 to 1.3 times the thickness of the metal deposited [43]. Since the target thickness was determined to be 4542 Å, a minimum LOR3A™ thickness of 5700 Å was determined necessary for clean lift-off. The provider has published thickness vs. RPM graphs for different LORs [43], but multiple tests were conducted to ensure the LOR3A™ thickness met the minimum requirement.

### ***3.3.3.1 LOR Thickness Tests***

Multiple layers of LOR3A™ were deposited on top of one another, spun and cured (heated) to increase the thickness. They were deposited at different spin speeds, exposed, developed and the 1805 was cleared using acetone. They were then examined under an Alpha-step IQ surface profiler. Two to four height measurements were taken from three different step areas on each sample to determine the thickness average and standard deviation. The results are shown in Table 2.

**Table 2. LOR3A™ thickness and deviation averages.**

<b>LOR3A™ layers</b>	<b>Spin speed (RPM)</b>	<b>Average thickness (Å)</b>	<b>Standard deviation (Å)</b>
1	1000	6003	510
1	2000	4871	243
2	2000	8053	179
2	4000	6085	120
3	4000	8184	139
4	4000	8383	150

### 3.3.3.2 PR quality factors

A few factors should be considered when determining the number of layers and spin speeds. They include thickness, edge-beads, uniformity and process time. The minimum required thickness is a key element for successful lift-off. If the LOR3A™ thickness is too small, the layer of metal on top of the 1805 PR and the layer on the substrate will contact. This will cause the entire layer of metal to adhere to substrate, as illustrated in Figure 23A.

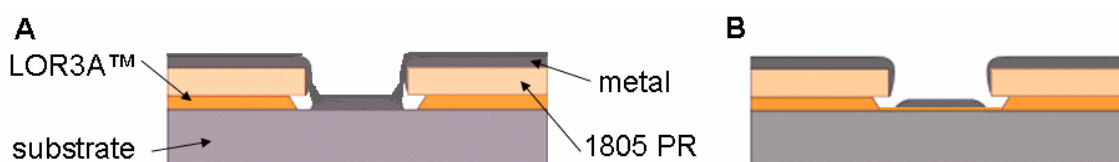


**Figure 23.** (A) If the LOR3A™ layer is not thick enough, the metal layer above the 1805 PR will contact the layer on the substrate. The metal will adhere to the substrate and not lift off. (B) If the LOR3A™ layer is not developed long enough, a thin layer could remain under the metal. In this case, all of the metal will be lifted with the LOR3A™.

Edge-beads posed another difficulty. When spun at lower RPM, the PR was much thicker on the outside edges of the sample than the middle. This would prevent the mask from contacting the center of the sample when exposing. A lack of contact here would often prevent the PR from developing at all. For this reason, the highest spin speed of 4000 RPM was chosen. The edge-beads developed using this speed were found to have negligible affects.

As shown in Table 2, the standard thickness deviation was less for higher spin speeds. The uniformity is important to ensure that the entire PR layer is above the minimum thickness. It is also a key factor in the modified fabrication method used, where the metal is left on top of the PR (see Appendix C).

On the other hand, higher spin speeds do require more fabrication time to achieve the same thickness. Since the PR thickness is less at higher RPM, three layers are needed at 4000 RPM to achieve the same thickness as two layers at 2000 RPM.

Both three and four layers of LOR3A™ were used to surpass the recommended minimum thickness. From Table 2, it is evident that there was not much difference in thickness between them. This is likely because the top layers do not adhere as well to the underlying LOR3A™ layers as they would to the substrate. The maximum achievable thickness was found to be approximately 8000 Å.

#### ***3.3.4 Exposure***

The chrome mask shown in Figure 24 was used to expose the array patterns (mask details in Appendix A). The positive mask was designed with metal where the gold is to be lifted off and no metal where the gold is to be deposited. Four VBGs with 5 or 10-μm spacing and two or four layers (steps) were patterned, corresponding to the markings on the plate. The four different patterns are referred to as 5x15, 10x30, 5x25 and 10x50. The first number refers to the step widths, and the second number the period, both in μm. Each cm<sup>2</sup> pattern was marked and numbered on the corners for alignment and tracking, as shown on the right of Figure 24.

The mask was placed in a Karl Süss MJB3 contact mask aligner. The plate heights were adjusted to ensure the mask and sample would be in contact during exposure. Each sample was then placed under its corresponding pattern and exposed. The UV intensity was set to 275 W/cm<sup>2</sup> at a wavelength of 405 nm. Prior analysis of 1805 PR showed the exposure time of 5.2 seconds to provide good line quality after



development [45]. Since the 1805 PR thickness was never adjusted (always a single layer at 4000 RPM), the same exposure time could be used consistently.

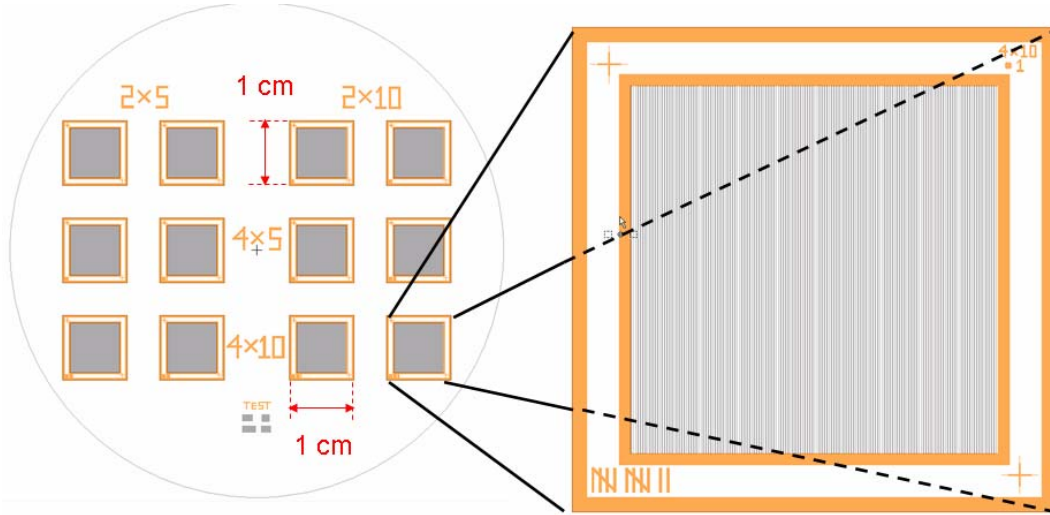


**Figure 24.** Chrome mask for photolithographic patterning of VBGs. A close up of the 12<sup>th</sup> array pattern is shown on the right with numbering and alignment markers on the corners (mask details in Appendix A).

#### 3.3.4.1 Mask Alignment

The most challenging part of the exposure process was correctly aligning the mask and samples. This was not an issue for the first step of course, because the pattern simply required centering on the chip. The challenge was in the precise alignment of layers on top of the first, which had to match at least within 1-2  $\mu\text{m}$  in the x direction, and precisely in angle.

The y-alignment was not critical. As long as the step pattern was aligned across the chip, a 10-50  $\mu\text{m}$  offset in the y-direction was negligible as the rest of the  $\text{cm}^2$  sample would still work. The x-direction alignment was critical, but only within each period. That is, if the 5x25 sample was off by a multiple of 25  $\mu\text{m}$  in the x direction, the step

pattern would still be correctly aligned. The angular alignment is also critical. A slight error in this will allow good alignment in one corner but not another. A picture of this x and y offset is shown in Figure 25 for the 10x50 sample. The steps are aligned fairly well in the angular and x direction, while the offset in the y direction is of minimal concern.

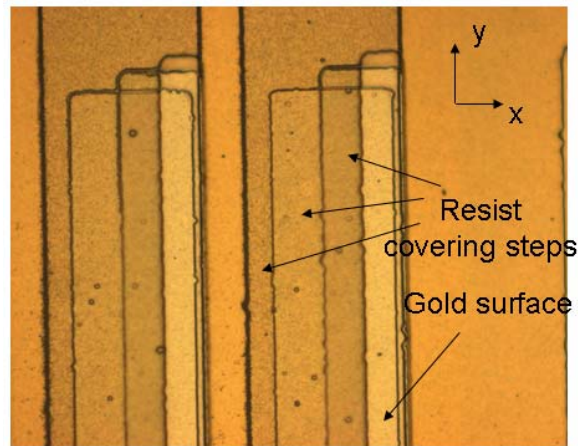


**Figure 25.** 10x50 sample before the final metallization. The final metal layer will be deposited in the bright yellow spot, where the resist has been developed and the gold surface is exposed.

The mask and sample were aligned by first matching one of the corner '+' signs (see Figure 24) in the x-y direction, then moving to the other corner '+' sign and aligning it by angular adjustment. After multiple repetitions of this process, the x, y and angular alignment were fine tuned. Most often, the thickest corner of the sample would contact first, causing the sample to shift unpredictably. This problem was lessened by taping the sample to the plate underneath. The limiting factors in alignment accuracy were therefore the maximum zoom of 20x combined with the unpredictable shift upon contact.

### 3.3.5 Development

The developing solution, LDD26W, dissolves the 1805 PR where it has been exposed. It then isotropically etches the LOR3A™ below it, as shown in Figure 21-4. Finding the preferred amount of time for development is an art. If the sample is not exposed long enough, the PR and/or LOR will not fully develop through to the underlying substrate. This would disallow the deposited gold from contacting the underlying layer where desired, as shown in Figure 23B. All the gold would lift-off in the final step.

On the other hand, if the sample is developed for too long, the line quality will deteriorate because the developer slowly eats away at the PR sidewalls and can undercut the LOR3A™. This sidewall etching and undercutting is shown in Figure 26 for longer developing times.

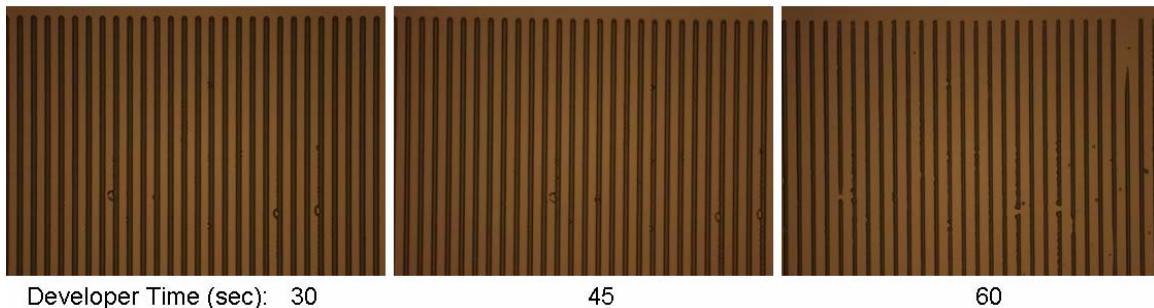


**Figure 26.** Line quality of 2  $\mu\text{m}$  lines at a 10  $\mu\text{m}$  period. The 30-second development shows slight roughness on the edges. The 45 second development shows better line quality, but the line width is slightly decreased due to the slow, unwanted development of the sidewalls. The 60-second development shows gaps where the LOR3A™ was undercut beneath the 1805.

The test shown in Figure 26 was done with a single layer of LOR3A™. Since additional layers were added to increase the thickness, more development time was

necessary. The time of 75 seconds was finally settled upon in order to ensure the LOR3A™ was developed through to the underlying gold.

#### ***3.3.5.1 Photolithographic Limits***

The photolithographic method used was found capable of creating 2- $\mu\text{m}$  thick lines of LOR3A™ and PR, as shown in Figure 26. A similar test showed that 2- $\mu\text{m}$  spacing between such layers was not achievable. The PR and LOR3A™ were not allowed to develop through the substrate under this width of exposure, no matter how long the development time. The minimum spacing required for the resist to appropriately develop was found to be 4  $\mu\text{m}$ .

#### ***3.3.6 Metallization***

Metallization was performed with a Denton Vacuum electron-beam evaporator (EBE). The samples were taped onto metal plates and placed in a vacuum chamber. High voltage (6 kV) and current (39 mA) was then applied to the metal, exciting evaporation onto the samples. A detector was placed in close proximity to the samples to determine the thickness of each deposition.

The deposition rates for Ti and gold were approximately 5  $\text{\AA}/\text{s}$ . Ti was used for the majority of the step thickness because it is less expensive. For each step, 4380  $\text{\AA}$  of Ti and 250  $\text{\AA}$  of gold were deposited sequentially, for a total thickness of 4630  $\text{\AA}$ . The detector showed thickness variations of less than one  $\text{\AA}$  per step (4629 – 4631  $\text{\AA}$ ). While the previously-determined target step height was 4542  $\text{\AA}$ , this different value (4630  $\text{\AA}$ ) was used as a target in the deposition process due to an initial calculation error in Equation 3.1.

This increased step height increased the OPL for each step height, which would increase the phase gradient of the reflected beam according to Equation 3.2. The envelope function would then be expected to initially (room temperature) peak to the left of the zero order. This is slightly towards the negative first order rather than at the zero order as designed for. This was not expected to alter the steering capabilities of the device; however, as long as all steps were fabricated with the same target thickness.

### ***3.3.7 Lift-Off***

The final lift-off step provides the long-awaited moment of truth. Figure 27 shows the three possible outcomes. In A, the metal is left where desired. In B, all of the metal has been lifted off, revealing an outline of LOR3A™ around where the gold was to be deposited. In C, some of the desired metal remains (left), but some has been inadvertently lifted off (right).

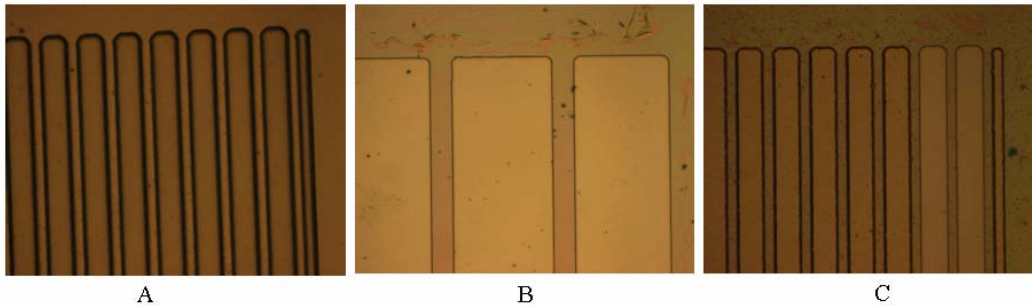


**Figure 27.** Samples after metallization and agitation in ACE. Successful (A), unsuccessful (B) and partially successful (C) results (100x zoom).

The lift-off technique was performed by first removing the samples from the metal plates. Being under extremely high heat in the EBE, this was sometimes difficult. If too much tape was used, the samples would often shatter before releasing. It was

found that very thin pieces of double-sided tape on opposite corners of the samples allowed easy removal.

The samples were then placed in acetone, and agitated in an ultrasonic bath. The acetone served to lift the 1805 PR, upon which the unwanted metal layer was lying. The agitation allowed the unwanted metal layers to be cleared from the sample. The remaining LOR3A™ layer was then removed by immersing the samples in Microposit Remover 1165, heated up to 90° C. This process brings the sample from steps five to six, as shown in Figure 21.

### ***3.3.8 PDMS Deposition***

The PDMS was prepared by combining a Sylgard® 184 silicone elastomer base with its curing agent. The silicon hydride in the curing agent reacts with the vinyl groups in the base to form a cross-linked, elastomeric solid [46]. The provider recommends a mixing ratio of 1:10 (curing agent : base). A ratio of 1:8 was used instead, based on guidance from an alternate source [47]. Due to the high viscosity of PDMS, it was spun at the high speed of 6000 RPM to create a thin, even coating. Based on standard RPM vs. thickness graphs of other materials [43] and values for PDMS [12], the PDMS layer was estimated to be approximately 15 µm thick.

## **3.4 Measurements**

Multiple views of the samples were taken after fabrication, but before the PDMS deposition. The sample heights were first measured with the Zygo® interferometer. The measurements were compiled into a single graph, as shown in Figure 28. The heights

shown were taken from the averages of six measurements for each step, and were used for modeling.

The average height of all steps was 4758 Å with a standard deviation of 213 Å between steps. This was greater than the target height of 4630 Å. The step height fluctuation is surprisingly high, considering the EBE displayed differences of only a few Å (4629-4631 Å) between deposition processes. According to Equation 3.2, the actual step-height deviation equates to an average phase lead between 0 and 68° per step at a 10° off-perpendicular incident beam angle.

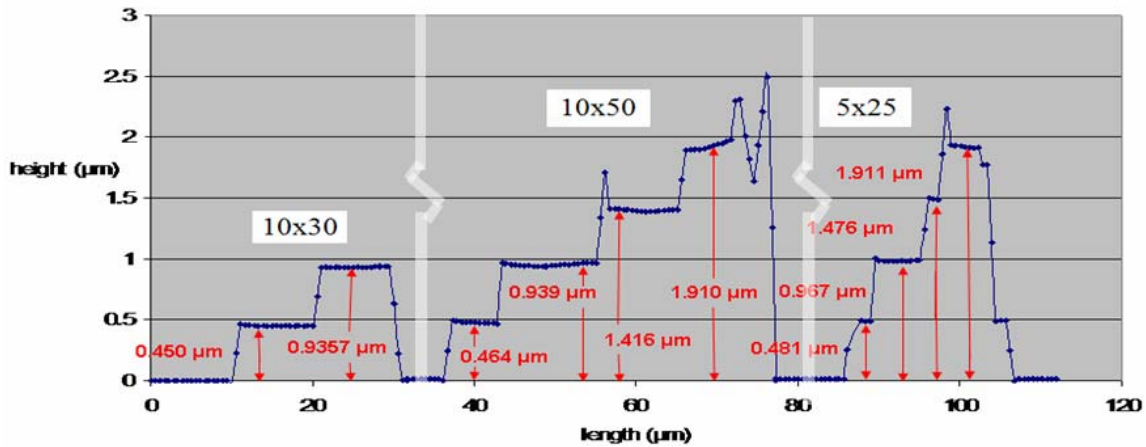


**Figure 28.** Cross-sectional view of three samples combined. The heights show the average of six measurements for each step. Data taken from Zygo® interferometer.

Since the Zygo® only sampled every 0.6 μm, it did not provide accurate step widths. These measurements were taken from the SEM instead, as shown in Figure 29, with their profiles aligned to those shown in Figure 28. Although not shown in the figure, the transition widths between steps were also taken to be included in modeling.

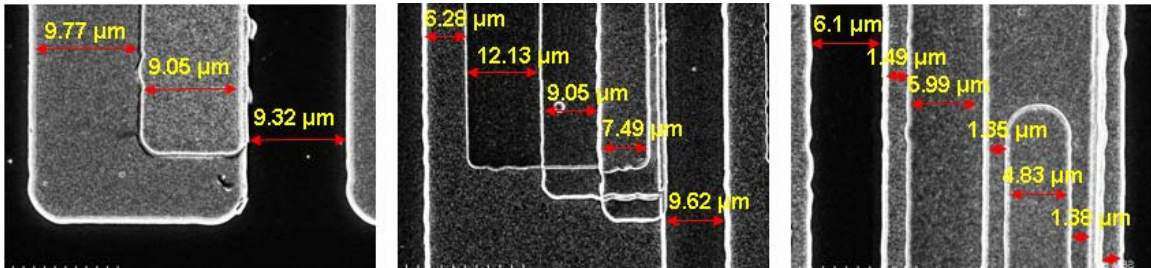


**Figure 29.** Top view with step width measurements for three samples. Images taken from SEM.

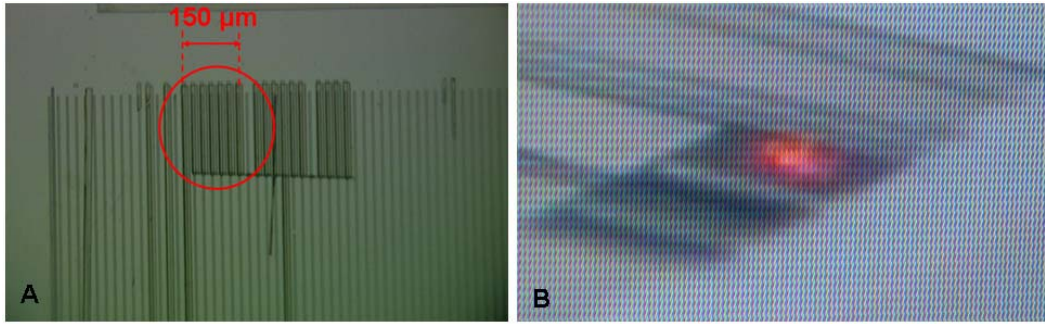
The 10x30 sample was aligned the best, with only a 4% discrepancy in step widths. The 10x50 and 5x25 were similarly aligned, both with a standard deviation of about 2  $\mu\text{m}$ . This was only a 25% width fluctuation for the 10x50 as compared to 60% for the 5x25. The mask aligner zoom of 20x was thus found to allow reasonable accuracy for 10  $\mu\text{m}$  step alignment, but not 5  $\mu\text{m}$ .

Figure 30 shows a circle around the well-fabricated section on the 5x25 sample. The laser was focused on this spot during testing to obtain the desired affect. The width of the region is about 150  $\mu\text{m}$ , which is the same width as the well-fabricated sections on the 10x30 and 10x50 samples. Fortunately, the spot size of the laser was able to focus down to just a little less than this width, allowing the majority of the beam to reflect off the desired location.

Over most of the samples, there were certain steps that were unintentionally lifted off. According to the provider's charts [43], this should not be due to the phenomenon shown shown in Figure 23A because the LOR3A™ height was about 1.7 times the height of the gold deposited. This is well over the recommended minimum of 1.3. The cause was more likely that shown in Figure 23B, where a thin layer of LOR3A remained under the desired metal. The developing time of 75 seconds was probably not long enough. It



was also found that thinner, wider-spaced steps deposited much better than wider, thin-spaced steps with this method.



**Figure 30.** (A) A good array of seven periods is circled in the 5x25 sample. (B) The laser beam was focused to this area (view from top right) during testing. The usable area was approximately 150 μm wide for all samples.

### 3.5 Summary

In summary, multiple aspects of the fabrication process have been thoroughly discussed. The primary steps included LOR and PR deposition, exposure, development, metallization and lift-off. The samples were fabricated with just enough usable area (~150 μm width) to test under a focused beam. The step height achieved was therefore the highest attainable with the given equipment and supplies.

Many limitations of the photolithographic process used were discovered. A maximum metal-evaporation height of 0.5 μm was found achievable, using LOR3A™. The maximum alignment accuracy attainable was found to be  $\pm 2$  μm, using the Karl Süss MJB3 contact mask aligner. Also, a resist line width of 2 μm was found attainable, but only a minimum width of 4 μm was achievable for spacings between the resist. The modeling and experimental setup for testing these structures will now be presented.

## **IV. Modeling/Experimental Setup**

### **4.1 Chapter Overview**

The following chapter is devoted to the model and experimental setup. The results of each will be presented together for comparison in the following chapter. Coventorware® and MATLAB® were used for modeling, and an optical test bench with various components was used for the experiment.

### **4.2 Modeling Setup**

#### ***4.2.1 Coventorware®***

An initial model of the experiment was first developed in Coventorware®. There were several purposes of this model: to gain a visual, three-dimensional (3D) perspective of the device, to determine whether the PDMS provided a conformal or planar fill, and to model the steady-state temperature variation of the plate vs. the PDMS. Knowledge of these factors was necessary in determining how to accurately model the device in MATLAB®, so the Coventorware® results will be presented first.

##### ***4.2.1.1 Setup***

Coventorware® is a finite modeling software package, which can provide in-depth numerical analysis of MEMS under various stimuli (voltage, temperature, stress, *etc.*). Two items were necessary to build the 10x50 model: a layout and process file.

The layout file was developed in a CAD environment. It consisted of multiple layers, each corresponding to a particular fabrication method as defined in the process

file. The multiple layers were drawn with the appropriate spacing and widths necessary to model the 10x50 sample. These included a substrate layer, five gold layers and a PDMS layer.

The process file included several components: materials, fabrication steps, and thicknesses. The software contained the material parameters for Si and gold, but the PDMS values had to be entered. These values, as shown in Table 3, were obtained primarily from the Polymer Data Handbook [48], as well as the provider's information sheet [41]. Approximate values of the Si, gold steps and PDMS thicknesses were entered as 500, 0.5 and 15  $\mu\text{m}$ , respectively.

**Table 3. PDMS material properties [41], [48].**

<b>Property</b>	<b>Value</b>	<b>Units</b>
Density	0.97	$\text{kg/m}^3$
Young's Modulus	500	Kpa
Poisson Ratio	0.5	-
Specific Heat	1.46	$\text{kJ/kg}\cdot\text{K}$
Thermal Conductivity	0.15	$\text{W/m}\cdot\text{K}$
Thermal Expansion	310	$\mu\text{m/m}\cdot^\circ\text{C}$
Dielectric Constant	2.5	-
Index of Refraction	1.431	-
Electrical Conductivity	$4\cdot 10^{13}$	$\Omega\cdot\text{m}$
Viscosity	3900	$\text{mPa}\cdot\text{s}$

#### ***4.2.1.2 Conformal vs. Planar Fill***

The PDMS layer was modeled to be deposited in both a planar and conformal fill. The thickness of the PDMS was found to dwarf that of the gold steps, so that the conformal fill shows only a slight variance from the planar. This is shown in Figure 31, where the top of the PDMS is slightly conformed to the edges of the top gold step. It is

most likely that this slight conformality will be negated by the PDMS flow, since it acts as a viscous liquid. The PDMS is thus expected to form a planar fill. The planarity could have been confirmed or denied by a profile measurement over the PDMS surface. No such measurements were taken; however, due to concern that the PDMS would adhere to the profilometer tip.

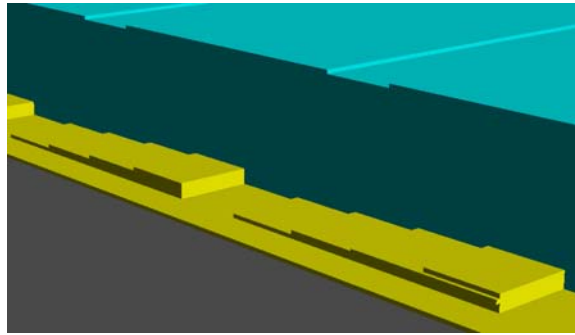


**Figure 31.** Conformal fill of PDMS. The top of the PDMS is shown slightly conformed to the edges of the top gold step. Modeling in Coventorware®.

#### ***4.2.1.3 Temperature Variance***

The device was then modeled at steady-state with a heat of 200 °C applied to the bottom of the substrate. This is the maximum serviceable temperature of PDMS according to the provider [41]. First, the device was modeled without the PDMS, to test the temperature variance in the top of the gold steps. A modest air flow of  $10^6 \mu\text{m/s}$  at 20 °C was applied to the sample top and sides to allow the air to convect heat away from these areas. The results are shown in Figure 32A, where the temperature of the gold varies by less than 0.1° from the bottom of the Si.

From the first test, we can assume the gold and Si are at the same temperature. The temperature variance was again modeled with the PDMS deposited as a planar fill

above the gold strips. As shown in Figure 32B, the top of the PDMS was heated to about 193 °C when the gold was heated to 200 °C.

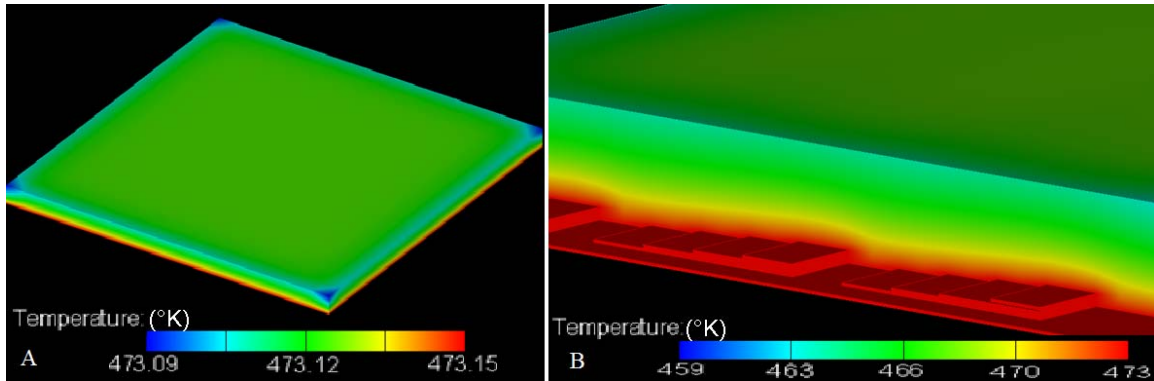


**Figure 32.** (A) Temperature model of gold layer on top of heated substrate. The temperature variance is less than 0.1°. (B) The top of the PDMS is heated to only 193 °C when the gold is heated to 200° C. Modeling in Coventorware®.

#### *4.2.1.4 Conclusions from Coventorware®*

The Coventorware® modeling provided a 3D perspective of the device as well as a temperature variance model. From the thickness of the PDMS, it is assumed to have a planar fill above the gold-step profile. Due to this thickness, it can also be concluded that the PDMS will expand upwards uniformly when heated. That is, the slight extra thickness of the PDMS corresponding to the lowest step height will not cause the top of the PDMS to expand more in the same area (although this was the initial intent of the design). The extra expansion would rather contribute to that of the entire top surface. It has also been shown that there exists a notable, steady-state temperature gradient in the PDMS, corresponding to its height off the underlying gold steps.

As shown by the blue lines in Figure 32A, the temperature of the gold is decreased at the corners, even in steady-state. This variation in the corner temperature is

expected to have a more pronounced impact for smaller feature sizes such as those on the 5x25 sample, because the temperature non-uniformity affects a proportionally larger part of each step. Access to a thermal imaging device could provide insight into this affect.

#### **4.2.2 MATLAB®**

The far-field intensity ( $I_{\text{total}}(x,y,T_{\text{plate}})$ ) of a coherent beam reflected off the VBG was modeled in MATLAB® by use of the Fraunhofer diffraction approximation [13]. The intensity was found for each of the three samples (10x30, 10x50 and 5x25) as a function of temperature ( $T_{\text{plate}}$ ) and x/y coordinates. The mathematics behind the code is traced from the culminating equation for intensity back to its temperature-dependent variables. The code is displayed and described in Appendix B.1.

##### **4.2.2.1 Assumptions/Approximations**

Several assumptions were made in creating the model. First, the impact of the PDMS thermal expansion is ignored. Although it will increase the OPL through the PDMS, it is expected to increase the OPL of each step height equally. The OPLs are then expected to remain constant with respect to each other in this regard, not contributing any change in the phase gradient with temperature. Instead, the negative  $\beta_{\text{PDMS}}$  value ( $dn_{\text{PDMS}}/dT$ ) was assumed to govern the OPL change with temperature. This assumption was confirmed experimentally by the direction the beam was steered (right instead of left).

Also, the step heights for each layer are modeled as perfectly planar, reflective surfaces. The average step heights, as shown in Figure 28, were used. The incident beam was also assumed to be planar. This is not technically accurate, as shown later in the

experimental setup, because the beam is actually focused onto the sample. Finally, the PDMS temperature was assumed equal to that of the plate. The Coventorware® modeling seemingly proved this an invalid assumption, but it was conducted with an air-flow of 1 m/sec simulated around the PDMS. There was no such air-flow applied during the experiment (other than the random flow through the lab). An analysis of this temperature gradient and its affect on the far-field pattern is presented in Appendix E.

#### 4.2.2.2 Coding

Several functions and parameters were initially defined as shown in Table 4.

**Table 4. MATLAB® coding parameters and definitions.**

<b><u>Parameter</u></b>	<b><u>Definition</u></b>	<b><u>Value</u></b>	<b><u>Units</u></b>
$T_{\text{plate}}$	hot plate temperature	20-200	°C
$T_0$	room temperature	20	°C
$n_{\text{PDMS}}(T_0)$	index of refraction	1.431	-
$n_{\text{PDMS}}(T_{\text{plate}})$	index of refraction	varies	-
$\beta_{\text{PDMS}}$	$dn_{\text{PDMS}}/dT_{\text{plate}}$	-0.0001	°C <sup>-1</sup>
$Z_{\text{offset}}(T_{\text{plate}})$	OPL from base to step height	varies	m
$Z_{\text{step}}$	step height	varies	μm
$\lambda$	laser wavelength	660	nm
$\theta$	off-perpendicular angle	13.5	°
$\alpha_{\text{Au}}$	thermal expansion rate of Au	$14.2 \cdot 10^{-6}$	μm/m•°C
$P$	number of periods	3 to 5	-
$z$	distance from diffractive source	1000	km
$t_{\text{step}}(\xi, \eta)$	transmittance function	0 or 1	-
$U_{\text{step}}(x, y, T_{\text{plate}})$	complex far-field	-	V/m
$I_{\text{total}}(x, y, T_{\text{plate}})$	far-field intensity	-	W/m <sup>2</sup>

$I_{\text{total}}(x, y, T_{\text{plate}})$  was found by adding and squaring the complex far-field ( $U_{\text{step}}(x, y, T_{\text{plate}})$ ) for each step height:

$$I_{\text{total}}(x,y,T_{\text{plate}}) = \left[ U_{\text{base}}(x,y,T_{\text{plate}}) + U_{\text{step1}}(x,y,T_{\text{plate}}) \dots + U_{\text{step4}}(x,y,T_{\text{plate}}) \right]^2 \text{ (W/m}^2\text{)} \quad (4.1)$$

The complex far-field for each step height,  $U_{\text{step}}(x,y,T_{\text{plate}})$ , was found for each step height according to Equation 2.2:

$$U_{\text{step}}(x,y,T_{\text{plate}}) = \frac{e^{\frac{j2\pi[z-2z_{\text{offset}}(T_{\text{plate}})]}{\lambda}} e^{\frac{j\pi}{\lambda[z-2z_{\text{offset}}(T_{\text{plate}})]}(x^2)}}{j\lambda[z-2z_{\text{offset}}(T_{\text{plate}})]} F\{t_{\text{step}}(\xi,\eta)\}_{f_x=x/\lambda z, f_y=y/\lambda z} \text{ (V/m)} \quad (4.2)$$

The two main parameters of this equation are the transmittance function ( $t_{\text{step}}(\xi,\eta)$ ) and the OPL from the base to step height ( $z_{\text{offset}}(T)$ ). The base is defined as the lowest, bottom step.

The  $t_{\text{step}}(\xi,\eta)$  function contains the width and spatial separation information for each step height. It has the value of one where the step is located and zero where the step is not. The step widths measured from the SEM (Figure 29) were used to define these regions with an accuracy of 512 pixels across the device. The Fourier transform of  $t_{\text{step}}(\xi,\eta)$  was found by the 2D fast Fourier transform function (fft2). The  $t_{\text{step}}(\xi,\eta)$  functions for all step-heights combined are shown in Figure 33, with offsets in the  $\eta$ -dimension to show each function separately. This dimension was included in the aperture-plane code to allow 3D visualization of the far-field pattern.

Notice each step array is spatially offset from the others. The number of periods (P) for each sample was entered to match the number of periods the 150  $\mu\text{m}$  beam waist was incident upon. These values were three, five and five for the 10x30, 10x50 and 5x25 samples, respectively, as shown in Figure 33. The far-field intensity corresponding to each  $U_{\text{step}}(x,y,T_{\text{plate}})$ , individually, would give a diffraction pattern with several fringes.



While this allows intensity distributed to several modes, the addition of the complex fields of all steps allows the intensity to be concentrated primarily into a single mode, given the required phase-matching.

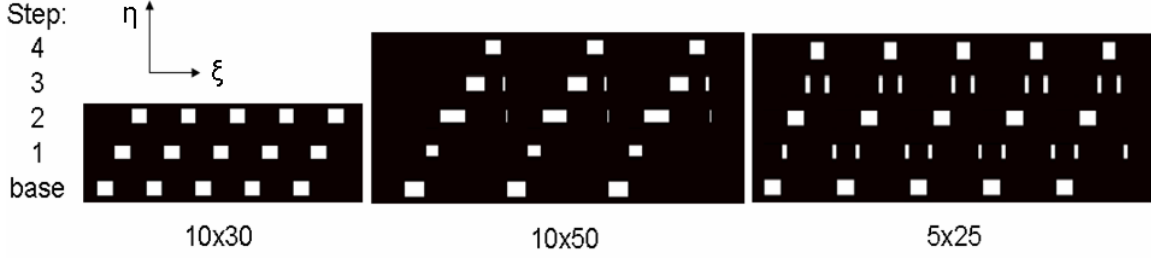


**Figure 33.** The width and spatial separation of each step for different samples (not to scale). Note that certain steps in the 10x50 and 5x25 samples are modeled in the flyback region as well. Widths correspond to the SEM measurements shown in Figure 29. Modeled in MATLAB® and combined.

The  $z_{\text{offset}}(T_{\text{plate}})$  value of Equation 4.2 is based on several parameters:

$$z_{\text{offset}}(T_{\text{plate}}) = \frac{n_{\text{PDMS}}(T_{\text{plate}}) z_{\text{step}} [1 + \alpha_{\text{Au}} (T_{\text{plate}} - T_0)]}{\cos(\theta)} \quad (\text{m}) \quad (4.3)$$

where the step height, thermal expansion of the gold steps and the angle of incidence are taken into account. The thermal expansion of gold only contributes noticeably at temperatures over 500 °C, but is taken into account for the sake of accuracy. Note that  $z_{\text{offset}}(T)$  is multiplied by two in Equation 4.2 because the device is in reflection-mode.

The  $n_{\text{PDMS}}$  value is a function of  $T_{\text{plate}}$  and  $\beta_{\text{PDMS}}$  [12]:

$$n_{\text{PDMS}}(T_{\text{plate}}) = n_{\text{PDMS}}(T_0) + \beta_{\text{PDMS}} (T_{\text{plate}} - T_0) \quad (4.4)$$

These equations were combined into  $U_{\text{step}}(x,y,T_{\text{plate}})$  for each step height over a range of temperatures from 20 to 200 °C.  $I_{\text{total}}(x,y,T_{\text{plate}})$  was then calculated separately for each sample at varying temperatures to yield the modeled results.

### 4.3 Experimental Setup

The basic setup is illustrated in Figure 34. An AlGaInP laser diode (660 nm) beam is focused to the desired spot on the sample after reflecting off mirror one. Not shown is a camera and TV screen set to show a 10x zoom of the sample. This allows fine tuning of the sample in the x, y and z direction to align it with the laser beam waist. The light is then diffracted off into different orders, each of which is diverging. The power detector was mounted on two stages to allow wide, precise movement in the x-direction. The intensity was captured in each order by translating the detector in that direction, repeating the process at increasing temperatures.

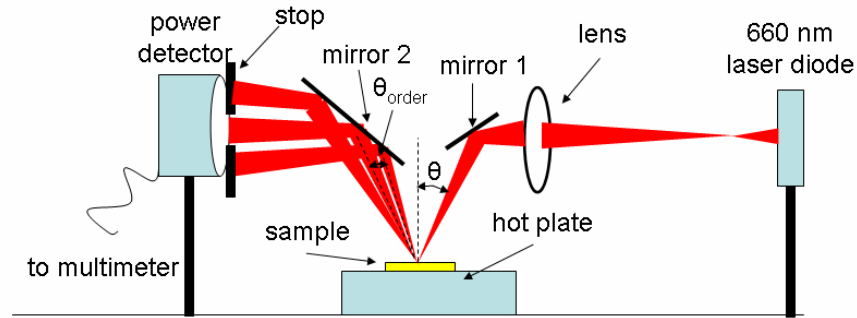


**Figure 34.** Setup one. The laser beam is focused towards the desired spot on the sample, which is laying on a hot plate. The light is diffracted off into different orders, each of which is diverging. The intensity in each order is then determined by the power detector as the hot plate temperature is increased.

The angles at which the beam diffracts are multiples of  $\theta_{\text{order}}$ , which is defined by Equation 2.8. This angle was measured experimentally by finding the distance from the

sample to the measuring point ( $z_{\text{path}}$ ) and the distance from the zero-order beam to the next order ( $d_{\text{order}}$ ):

$$\theta_{\text{measured}} = \tan^{-1} \left( \frac{d_{\text{order}}}{z_{\text{path}}} \right) \quad (4.5)$$

The angle of diffraction shown in Figure 34 is misleading in a sense, and is better-illustrated in Figure 35. The samples were aligned with their tops facing the power detector, so that the beams would actually diffract horizontally in the  $\xi$ -direction. This direction limits any unwanted reflection off the steps due to the incident angle,  $\theta$ .

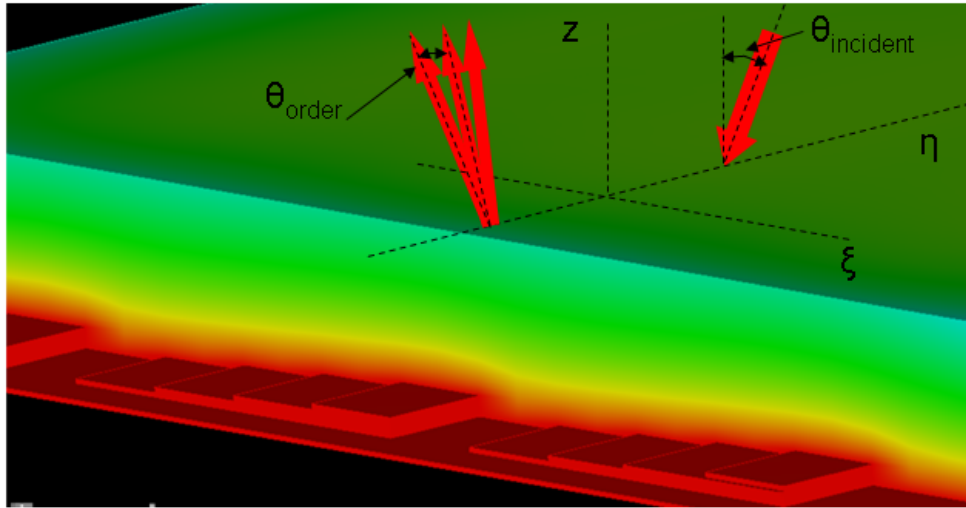


**Figure 35.** The beam is incident normal to the  $x$  axis and at the angle  $\theta$  between the  $z$  and  $y$  axis. The reflected beam is diffracted at multiples of angle  $\theta_{\text{order}}$  between the  $z$  and  $x$  axis.

One drawback of focusing the laser onto the sample was the divergence of the diffracted beams. This made it more difficult to distinguish one order from the next, as can be seen from the small separation of the beam widths shown in Figure 34. This was particularly important for the 10x50 sample, where  $\theta_{\text{order}}$  was only  $0.75^\circ$ . In order to

minimize the convergence angle of the incident beam, a large focal length was necessary for the lens (Lens 1 in Figure 36). It was also moved closer to the focal point of the incident beam, allowing a more-gradual convergence, which equates to less angular divergence of the reflected beams. This also aided the assumption of an incident planar wavefront, for which the VBG was designed.

Setup 2 (Figure 36) shows the second data-collection method. The diverging beams are sent through lens 2 to converge towards the CCD camera. The images were captured by PixelScope Lite software, and imported into MATLAB® for viewing of the beam profile (code in Appendix B.2).

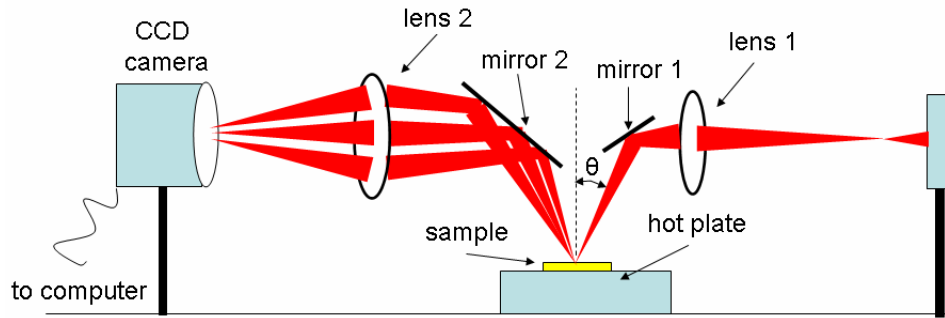


**Figure 36.** Setup two. The diverging beams are sent through lens 2 to converge towards the CCD camera.

A neutral density filter ( $ND = 3$ ) was placed in front of the CCD camera to limit the background noise in the images. The intensity of the laser was increased to around 32 mW ( $\sim 0.5$  mW) when the beam's reflected intensity met the camera's saturation limit. The hot plate temperature was increased from 20 to 199 °C in 25 °C increments. In order to ensure steady-state conditions, the sample was allowed to heat as the hot plate temperature increased, and to sit at the target temperature for two to five minutes.

#### **4.4 Summary**

The Coventorware® results were discussed in order to aid the MATLAB® modeling. One significant find from Coventorware® was that the thermal expansion of PDMS would have little if any affect on the far-field diffraction pattern. Now that the modeling and experimental setup has been defined, the results are presented together in the following chapter.

## **V. Results and Analysis**

### **5.1 Chapter Overview**

The modeled and experimental results of the 5x25 and 10x30 samples are presented. The beam profiles and efficiencies are closely analyzed. A standard variance was noted in the angular dispersion of intensity for both samples. An updated model follows, which accounts for these noticed variances. The effective PDMS parameters are thus determined from a combination of the experimental data and model.

In spite of various and repeated tests, the experimental 5x25 diffraction pattern showed little variation with temperature. The PDMS quality of the sample was likely compromised due to it inadvertently contacting the hot plate surface. The results of this sample are not included here, but are shown in Appendix D for completeness.

### **5.2 Initial Modeling Results**

#### ***5.2.1 Modeling at 20 °C***

Using the parameter values defined in Table 4, the far-field intensity was modeled for each sample at 20 °C. Figure 7 provides a good mathematical, visual explanation of how the intensity is distributed into the different orders. Based on Equation 2.8, the orders were expected to be separated by 1.26 and 0.76 ° for the 10x30 and 10x50 samples, respectively. These expected angles are confirmed by the model, as shown in Figure 37.

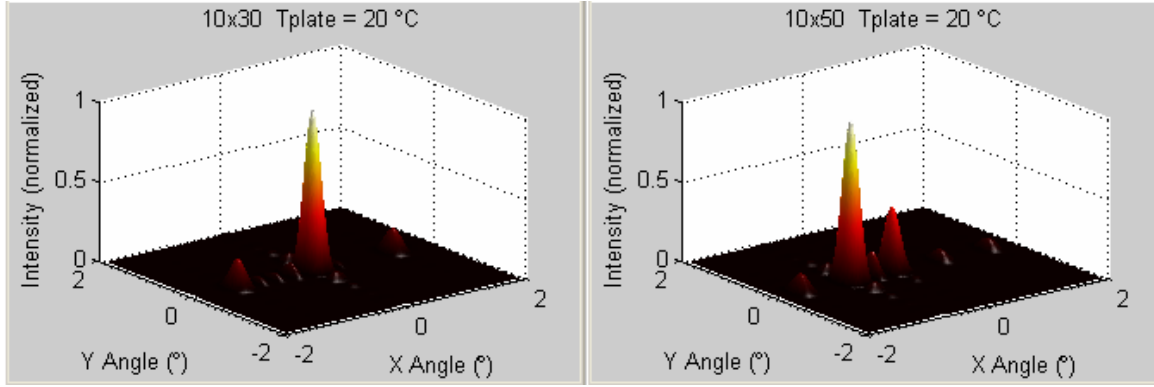


**Figure 37.** Far-field diffraction pattern modeled for the two samples at 20 °C. The angular intensity is shifted towards the negative first order for both.

The intensity from the 10x50 sample was contained mainly in the negative first order, while that of the 10x30 sample was concentrated mainly in the zero order. This was expected because the step heights were fabricated a little larger than was designed for zero-order diffraction. The phase increase ( $\Delta\Phi$ ) was expected to be between 0 and 72° for each step, which correlates to midway between 0 and negative first order for the 10x50 sample, and closer to the zero order for the 10x30 sample.

#### **5.2.1.1 Lobe Widths**

It may initially seem that since the 10x30 sample was modeled over five periods, it should have a tighter angular confinement. Figure 37 shows a similar beam width to that of the 10x50 sample; however, because the lobe width is actually  $2\lambda/Nw$ . Since  $Nw$  yields the same product for both samples ( $5 \cdot 30 = 3 \cdot 50$ ), their lobe widths are equivalent.

#### **5.2.2 Modeling at 199 °C**

The intensity was simulated again at 199 °C. The index of refraction decreases as the temperature increases, giving rise to shorter OPLs and therefore a decreased phase gradient ( $\psi$ ). This value is defined here as positive when the  $\Delta\Phi$  values are positive, as

shown in Figure 19B. The intensity was therefore expected to shift right, towards the positive-angle side, due to the negative  $\beta_{\text{PDMS}}$  value. The models exhibited this phenomenon at increased temperature, as shown in Figure 38.

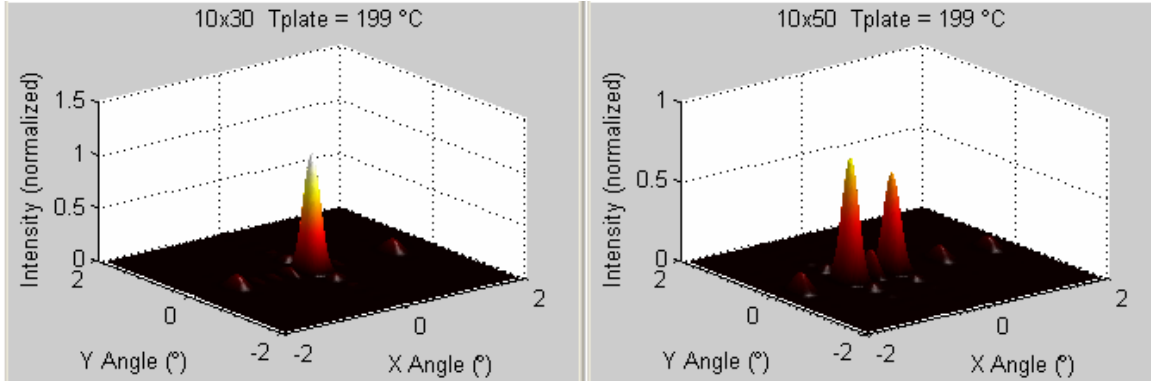


**Figure 38.** Far-field diffraction pattern modeled for the three samples at 199 °C. The intensity shifts slightly to the right at a higher temperature due to the negative value of  $\beta_{\text{PDMS}}$ .

The angular shift in the 10x30 sample is not readily apparent, but it can be seen that the intensity in the zero order is increased slightly from the model at 20 °C. More intensity is thus allowed in the zero order as  $\psi$  approaches zero.

Both samples have similar  $\psi$  values due to their similar step heights and widths. The 10x50 model offers a better estimate of the change in this variable with temperature; however, because its larger period allows shorter separation of angular orders. The shift of the envelope function is therefore more-readily apparent. The intensity in this sample went from mostly in the negative first order at 20 °C, to about half in the negative first and half in the zero order at 199 °C.

Also, upon closer examination, subsidiary maxima are found between the defined orders. These are governed by the number of periods, according to Equation 2.7 [16]. The 10x30 sample is modeled for five periods, which corresponds to three subsidiary



maxima. These are easier to spot in the side view of its diffraction pattern shown in Figure 39. The 10x50 model shows one subsidiary maxima, which correctly corresponds to its three modeled periods.

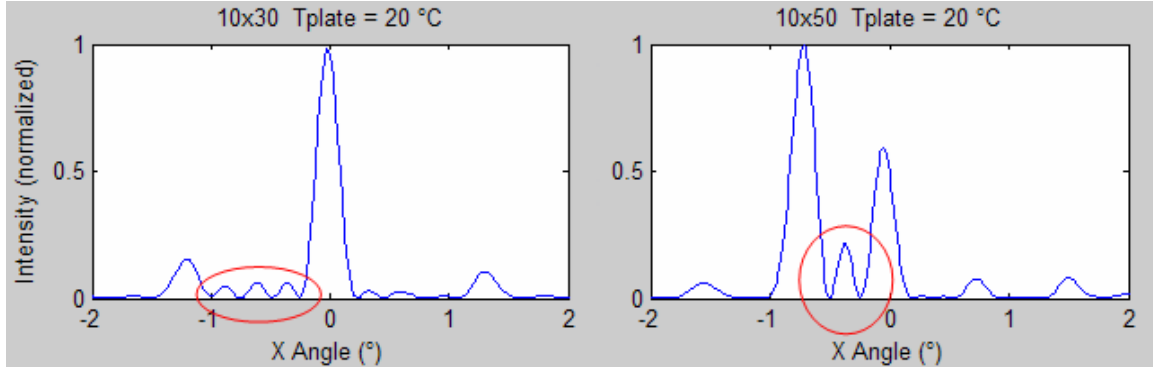


**Figure 39.** A side view of the 10x30 and 10x50 diffraction pattern across the  $y = 0^\circ$  line modeled at 20 °C. Three subsidiary maxima are shown between the zero and negative first orders for the 10x30 sample, and one for the 10x50. This correctly corresponds to the number of periods modeled for each (five and three).

### 5.2.3 Efficiency

The expected efficiency of the VBGs are both calculated and modeled. Equation 2.12 provides an estimate for the maximum efficiency of an ideal step-profile diffracting into the first order. This value, referred to here as  $\eta_{1\_calculated}$ , is based on the number of steps (N). The efficiency was also modeled assuming ideal heights and widths with perfect spacing, named  $\eta_{1\_ideal}$ , which was expected to correspond closely to  $\eta_{1\_calculated}$ .

Another model,  $\eta_{1\_ideal\_height}$ , assumed the actual widths and perfect heights. The last model,  $\eta_{1\_actual}$ , assumed the actual widths and heights with the temperature adjusted (non-realistically) to achieve negative first-order diffraction. The plots of these models are shown across the x-axis in Figure 40 for greater clarity.

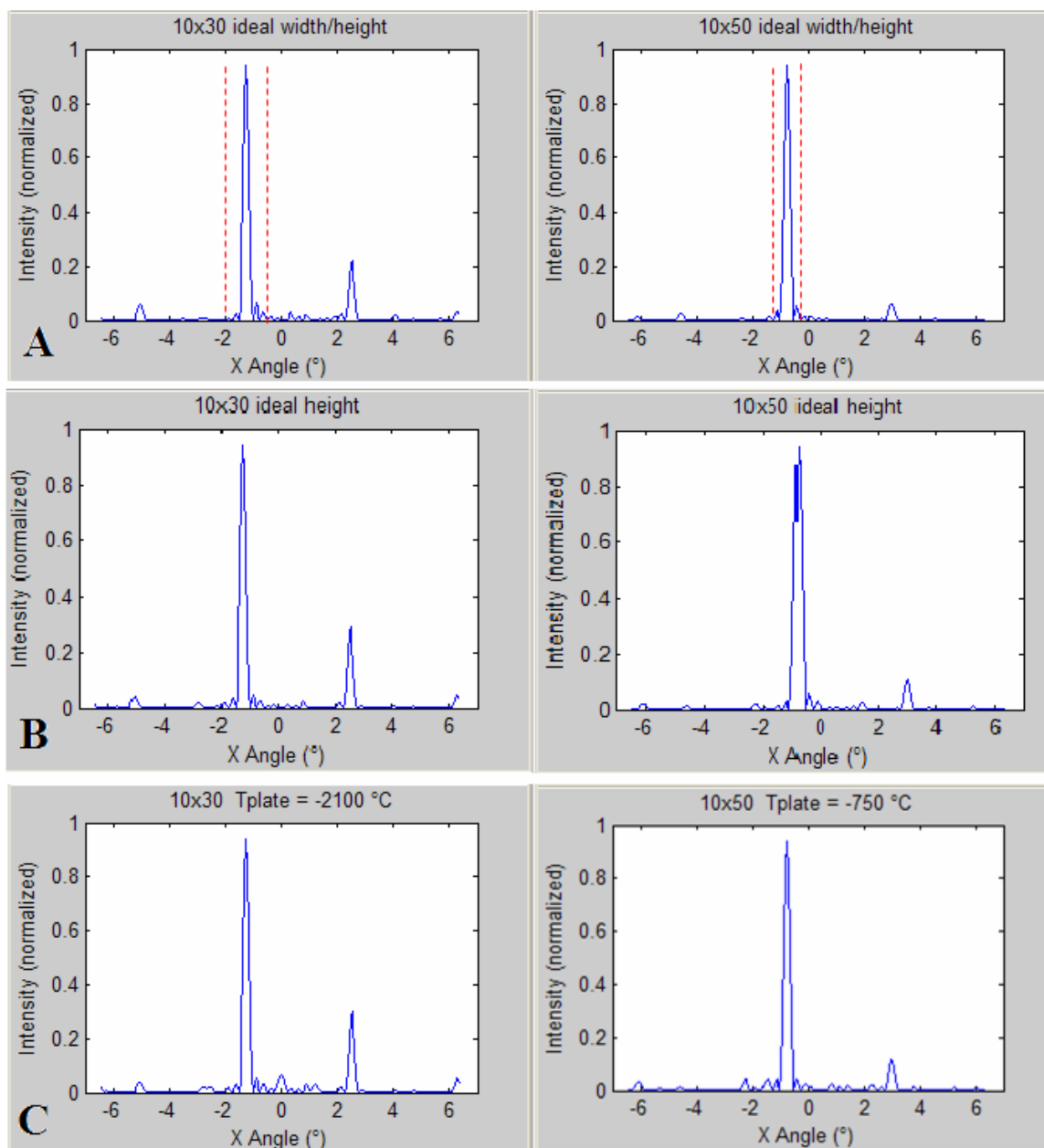


**Figure 40.** The modeled beam profiles of the 10x30 and 10x50 samples are shown across the x-axis when directed into the negative first order. They are modeled for ideal widths and heights (A), ideal heights and actual widths (B), and actual heights and widths (C). The dotted lines in part A show the region of integration for calculating the intensity in the negative first order.

The slight decrease in efficiencies as the actual parameters are included can be seen by the slight increase in intensities at angles outside of the negative first order.

Figure 40 shows that the efficiencies decrease slightly, but not very significantly, when the actual parameters are modeled.

Each model was integrated from the midpoint between the negative first and negative second orders, to the midpoint between the negative first and zero orders. This region is signified by the dotted red lines in part A. This value was then divided by the integral spanning  $\pm 7^\circ$  in the x-direction to give the total efficiency diffracted into the negative first order. The calculated and modeled efficiency values are displayed in Table 5.

**Table 5. Calculated and modeled efficiencies for diffraction into the first order.**

<b>Device</b>	<b><math>\eta_1</math> calculated</b>	<b><math>\eta_1</math> ideal</b>	<b><math>\eta_1</math> ideal height</b>	<b><math>\eta_1</math> actual</b>
10x30	0.684	0.6859	0.6718	0.6704
10x50	0.875	0.8152	0.7504	0.6837

$\eta_{1\_calculated}$  was very close to  $\eta_{1\_ideal}$  for the 10x30 sample. The slight variance in the actual step widths to the ideal case ( $\pm 4\%$ ) only decreased the first order efficiency by 2%. The difference in step heights (247 Å) was even less significant. The width fluctuation in the 10x50 sample ( $\pm 20\%$ ) decreased the efficiency by 8%. This is less than the 12% predicted by Equation 2.10 for the flyback region ( $\Lambda_F$ ) of 3  $\mu\text{m}$ . The 10x50 height fluctuation ( $\pm 123$  Å) was found to decrease the efficiency further by 9%.

### 5.3 Experimental Results

The experimental results from setups one and two will be presented and discussed for the 10x30 and 10x50 samples. The results from both setups corroborate each other, as they both show similar trends for increasing temperature. The results from setup two

do carry more weight, as they were not subject to the same magnitude of measurement error as the results of setup one.

### 5.3.1 Setup One

The results from setup one are shown in Figure 41. Both samples appear to start near the zero order at 25 °C and shift towards the first order angle as the temperature increases. The input current to the AlGaInP laser diode was 106.8 mA for both samples. The baseline laser power was detected at 47.5 mW after having reflected off the same optics (mirrors, lens) and a flat, gold sample.

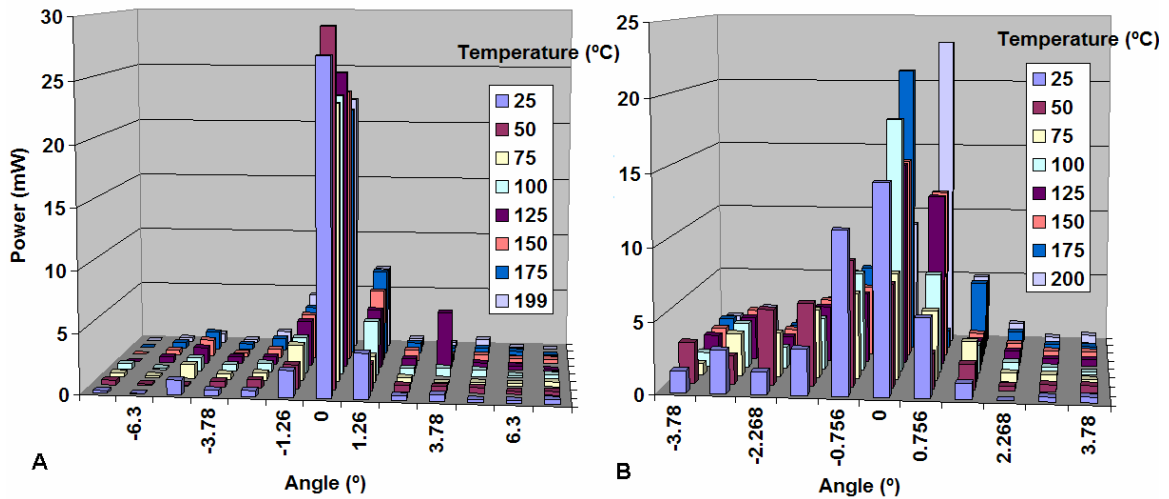


**Figure 41.** Experimental results of setup one for the 10x30 (A) and 10x50 (B) sample. Both samples appear to start near the zero-order at 25 °C, and shift towards the first-order angle as the temperature increases.

The highest efficiency measured was about 60% in the zero order for the 10x30 sample at 50 °C. The zero order efficiency should approach unity regardless of the number of steps, as long as the heights are well-matched. The efficiency does not approach its limit in any case here because the range of  $\psi$  did not allow the intensity to reside in a single order (see Figure 7A).

The wider, angular separation of the 10x30 diffraction orders allowed more consistent data collection. The separation of the stops in capturing the 10x50 data was likely too large, allowing power from the surrounding orders to be included in each measurement. This introduced a significant amount of error from inconsistencies in translating the power detector, which contributed to the high deviations of the 10x50 data. Also, the error margins from the detection alone were up to  $\pm 10\%$  in many cases due to the combined instability of the optical equipment.

### ***5.3.2 Setup Two***

Two beam profiles from setup two are shown in parts A and B of Figure 42 for the 10x30 sample and Figure 43 for the 10x50 sample. The beams shift towards the first order with increasing temperature as the model predicted. There are two or three, partially distinguishable, subsidiary maxima between the orders for the 10x30 sample, as shown in Figure 42B. This shows the majority of the beam was incident upon four or five periods.

Figure 43A shows that the beam reflected off the 10x50 sample at 20 °C is contained mainly in the zero and first orders. This shows a significant variance from the model, which predicts it to reflect mainly into the negative first order. Again, the beam shifts towards the first order with increasing temperature as the model predicted. There is one subsidiary maximum shown between the orders, which agrees with the model. This was expected because the area on the sample where the laser was focused was only three periods wide. The subsidiary maxima of both samples were found to be larger than predicted.

## 5.4 Updated Model

At 20 °C, the beam profiles were initially shifted more in the positive-angle direction than the modeling predicted. The experiment thus displayed a negative  $\psi$  value while the model displayed a positive value. This translates into the OPL for each step being less than that predicted by the model. It was originally proposed that the PDMS slightly conformed to each step, reducing the OPL for each step height proportionally; but the Coventorware® fill-modeling disproved this hypothesis.

Based on Equation 4.3, there are three parameters influencing the OPL ( $z_{\text{offset}}(T)$ ):  $z_{\text{step}}$ ,  $\theta$  and  $n_{\text{PDMS}}$ . The step heights were well-established from the Zygo® measurements, so  $z_{\text{step}}$  can be counted out. The  $\theta$  value determined from measuring the experimental setup (13.5°) was used in the modeling. Even if this measurement was off by two degrees, it would affect the OPL by less than 1% and  $\Delta\Phi$  by only 5° per step. This is not nearly sufficient to account for the difference. The only variable remaining is the index of refraction. There are a few possible explanations for a variance in this parameter: an alternate mixing ratio of 8:1 used instead of 10:1 and dispersion ( $dn/d\lambda$ ). The  $n_{\text{PDMS}}$  value of 1.431 was determined using a wavelength of 632.8 nm [12], but a slightly larger wavelength of 660 nm was used in this experiment.

The  $n_{\text{PDMS}}$  value is also defined as 1.4 [48], but an effective value of 1.29 was determined, by trial and error, to match the experimental results for both samples. The far-field intensity of both samples at 20 °C is modeled in part C of Figure 42 and Figure 43 using this value. Cross-referencing these plots with the experimental beam profiles in part A of the same figures shows an excellent correspondence for both samples.

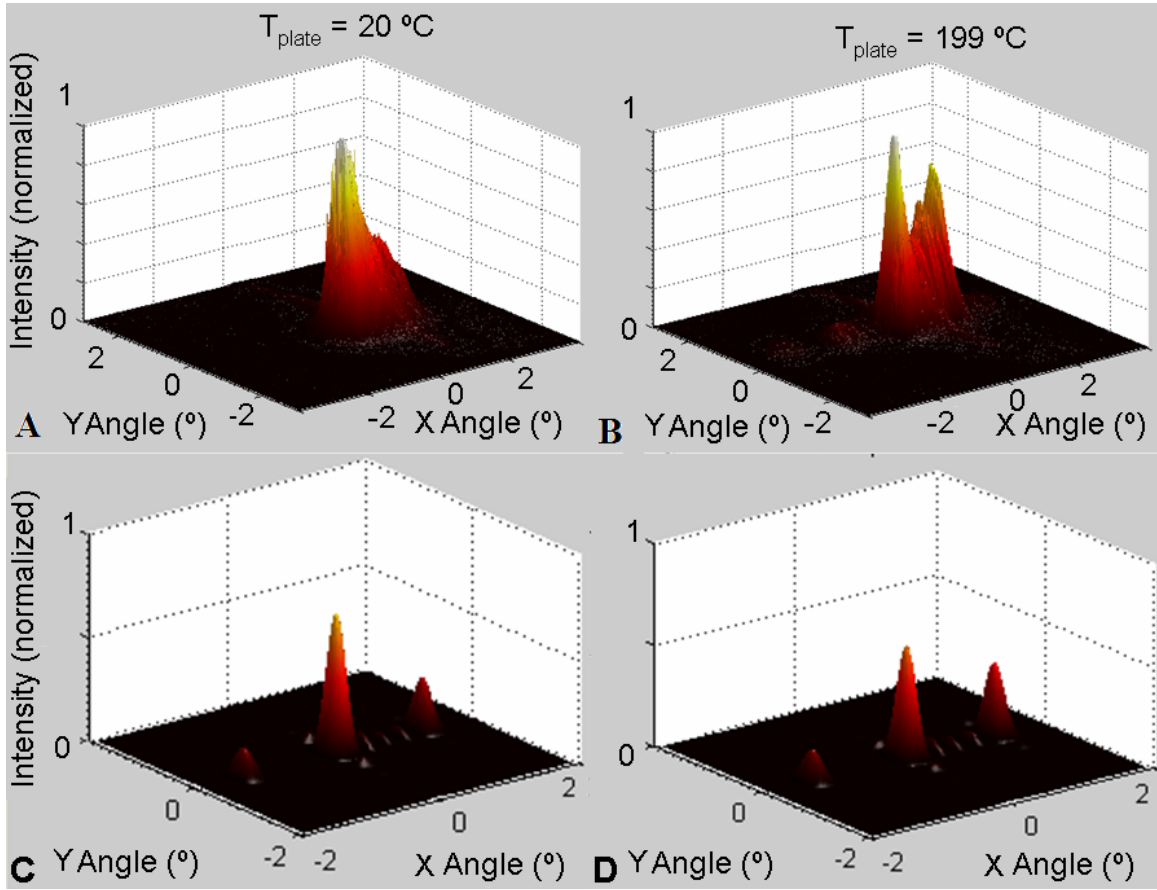


**Figure 42.** (A) Beam profile of reflection off the 10x30 sample at 20 °C. It is confined mainly to the zero order. (B) At 199 °C, the beam is partially shifted to the first order angle of 1.26°. (C) Far-field intensity model of the 10x30 sample with  $n_{\text{PDMS}} = 1.29$  and  $\beta_{\text{PDMS}} = -0.00012 \text{ } ^\circ\text{C}^{-1}$  at 20 °C and (D) 199 °C. These models correspond well with the experimental beam profiles shown in A and B.

From the starting point of  $n_{\text{PDMS}} = 1.29$ , the intensities were again modeled at 199 °C. It was found, again by trial and error, that with a  $\beta_{\text{PDMS}}$  value of -0.00012, the model matched the experimental results well in both samples. This value is just slightly higher than the published value of -0.00010 [12]. These models are shown in part D of Figure 42 and Figure 43. Again, cross-referencing these plots with the experimental beam profiles in part B of the same figures shows an excellent correspondence for both samples.

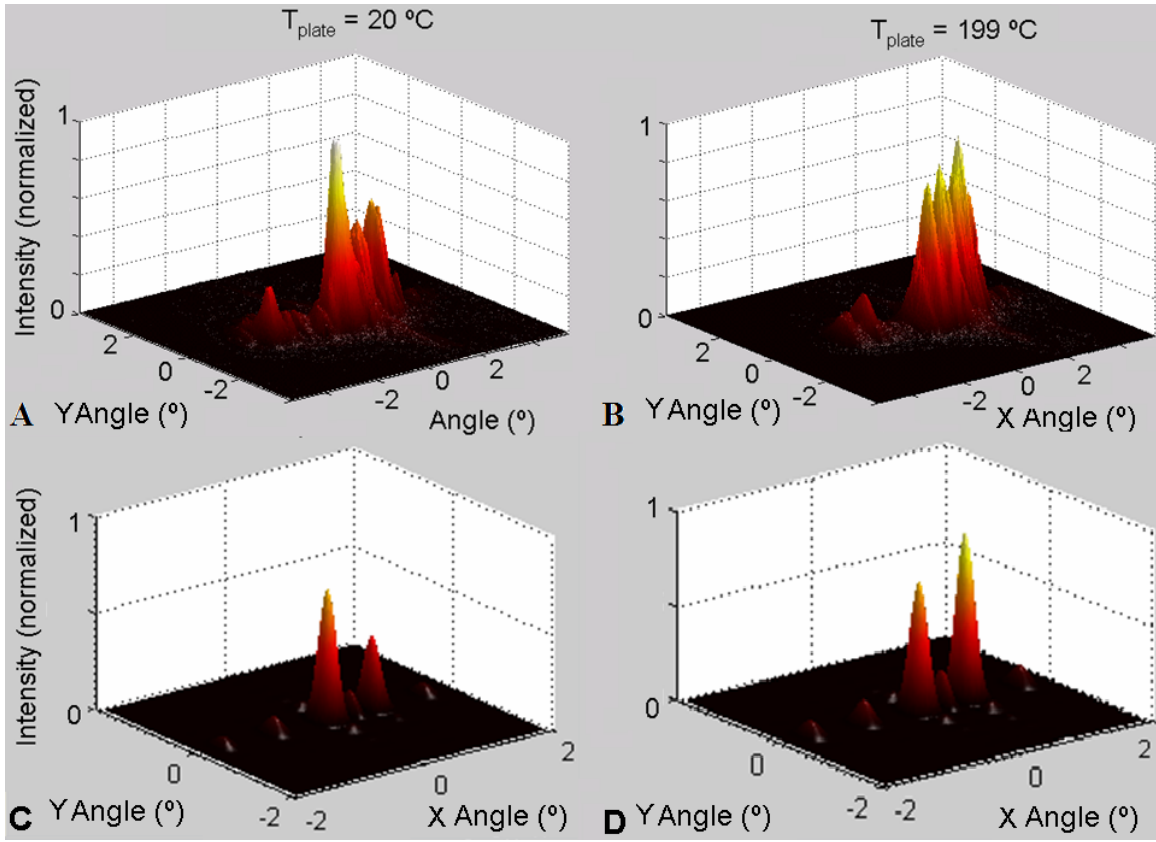


**Figure 43.** (A) Beam profile of reflection off the 10x50 sample at 20 °C. It is initially between the zero and first order. (B) At 199 °C, the majority of the beam is shifted to the first order angle of 0.75°. (C) Far-field intensity models of the 10x50 sample at 20 °C and (D) 199 °C with  $n_{\text{PDMS}} = 1.29$  and  $\beta_{\text{PDMS}} = -0.00012$ . These models correspond well with the experimental beam profiles shown in A and B.

## 5.5 Summary

Thermally-activated beam steering was successfully demonstrated for the 10x30 and 10x50 samples. The experimental efficiencies ( $\eta$ ) for the zero and first order of both samples at 20 and 199 °C are shown in Table 6. These values were found in a similar manner to that shown in Figure 40, except the intensity was integrated over the x and y axes. The intensity for the zero and first orders were integrated over the x-axis midpoints



between orders and over the entire y-axis. The data shows that the beam intensity shifted from primarily in the zero-order to primarily in the first-order for both samples, although it did not initially seem this was the case for the 10x30 sample (see Figure 42). The primary limiting factor of the efficiencies was that  $\psi$  did not steer the beam entirely towards either order, but instead directed the intensity between the orders over the temperature range of 20 - 199 °C.

**Table 6. Efficiencies in each order at different temperatures.**

<b>Device</b>	<b>T<sub>plate</sub></b>	<b><math>\theta_{\text{order}}</math></b>	<b><math>\eta_{\text{zero order}}</math></b>	<b><math>\eta_{\text{first order}}</math></b>
10x30	20° C	1.25°	54%	28%
	199° C		35%	45%
10x50	20° C	0.75°	33%	26%
	199° C		24%	40%
5x25	20-200° C	1.5°	N/A	N/A

The experimental beam profiles were initially found to disagree with the model because they were shifted towards the positive-angle side. This suggested a common error in the OPL modeled for the step heights of each sample. The index of refraction value was determined to be the most likely cause of the discrepancy. The modeling and experimental data at 20 °C for each sample was found to correspond very well when modeling with a room-temperature  $n_{\text{PDMS}}$  value of 1.29 instead of 1.431.

Using this updated  $n_{\text{PDMS}}$  value, the modeling of each sample at 199 °C was found to correspond very well to the experimental results when a value of  $-0.00012 \text{ }^{\circ}\text{C}^{-1}$  was used for  $\beta_{\text{PDMS}}$ . The difference in the  $n_{\text{PDMS}}$  value is likely due to the alternate mixing ratio of base to curing agent used in forming the PDMS. A plot of  $n_{\text{PDMS}}$  vs. T

shows that the determined  $\beta_{\text{PDMS}}$  value allows it to fit well within the error bars of the previous experiment [12].

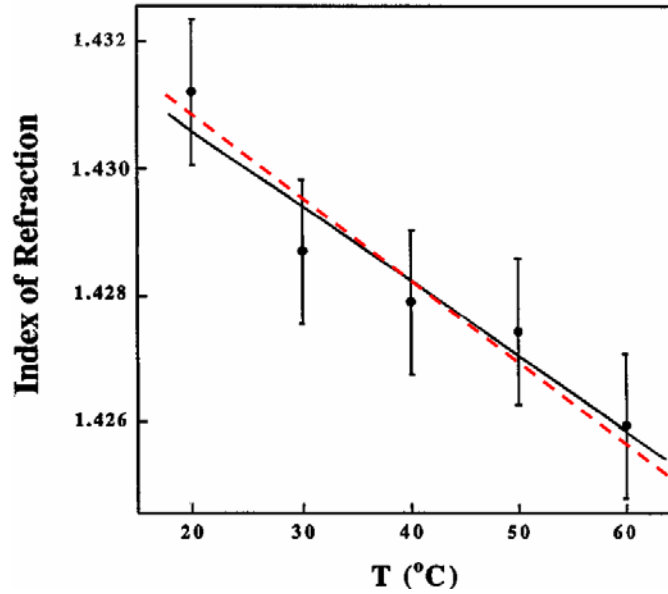


**Figure 44.** Data and error bars used for a previous determination of  $\beta_{\text{PDMS}}$  are shown in black [12]. The dashed red line shows the experimentally-determined  $\beta_{\text{PDMS}}$  value falls within the error bars of the previous research.

This and the agreement of two samples over a larger temperature range suggest the value determined here is more accurate. The  $\beta_{\text{PDMS}}$  value may have also been altered by the different mixing ratio, and it may slightly vary over the serviceable temperature range of PDMS (-45 to 200 °C). More tests would be necessary to confirm such standard fluctuations in  $n_{\text{PDMS}}$  and  $\beta_{\text{PDMS}}$ .

## **VI. Conclusions and Future Work**

### **6.1 Chapter Overview**

This chapter summarizes the major achievements and significance of the research presented herein. The thesis body then concludes with a discussion of potential methods for continuous steering, increasing the controllable FOR and alternate methods of temperature control.

### **6.2 Achievements**

There were several, significant achievements of this research:

- First fabrication and modeling of step-approximated blazed gratings with PDMS used as the active, phase-controlling agent
- First demonstration of thermally-activated beam steering on micro-scale
- Demonstration of a non-mechanical beam-steering method whose FOR is not limited by the fringing field effect
- A systematic model to determine the effective  $n_{\text{PDMS}}$  and  $\beta_{\text{PDMS}}$  values
- Determination of several photolithographic fabrication limits:
  - A maximum alignment accuracy of  $\pm 2 \mu\text{m}$  using the Karl Süss MFB3 contact mask aligner
  - A maximum metal-evaporation thickness of  $0.5 \mu\text{m}$  using LOR3A<sup>TM</sup> as the lift-off resist
  - Minimum line width of  $2 \mu\text{m}$
  - Minimum line spacing of  $4 \mu\text{m}$

### ***6.2.1 Significance***

The primary significance of this research lies in the ability to achieve beam steering without the FOR limitations of the fringing field effect. This effect is caused by the necessary variation of the material index across the length of the device, and is circumvented here by depositing the index-varying material on a blazed grating. In this way the material index is allowed to change uniformly, but still control the phase gradient. The fringing field effect is thus negated because there is no change in index across the device.

The fabricated device was limited; however, to a small FOR and discrete steering angles. As the device was designed only for an initial proof of concept, these limitations were expected. Methods for increasing the device performance, as well as alternate methods of heating, are suggested below.

## **6.3 Recommendations for Future Work**

### ***6.3.1 Increased FOR***

Although the VBG devices were shown to circumvent the fringing field effect, the FOR demonstrated was less than one degree. The temperature sensitivity of the device was not enough to shift the phase gradient completely from one order to another. This ability would be desirable for even the most basic of functions, such as a switch.

This small FOR was dictated by two fabrication limits: the step height and width. The step widths were limited to about 5-10  $\mu\text{m}$  due to the photolithographic method used, and the step heights were limited to about 0.5  $\mu\text{m}$  by the LOR3A™ thickness. The same

photolithographic method could be used with LOR30B™ instead, which would provide a much thicker base layer (2.7  $\mu\text{m}$  at 4000 RPM), allowing larger step heights [43].

Other, more effective, ways of creating blazed grating include X-ray and e-beam lithography [39], [29]. These more-advanced methods would enable steeper angles and blazed profiles rather than stair-step approximations. The major tradeoff with having a steeper base profile would be response time. As the active material gets thicker, it takes more time to fully respond. While the dynamic response of PDMS to thermal excitation has not yet been investigated, it would be a key figure of merit for potential applications requiring rapid switching and/or scanning.

Another method of increasing the FOR would be to exploit the thermal expansion of PDMS. Although this was the original aim of the research, the fabrication method did not allow it to contribute. Although the coefficients oppose each other, the net affect of  $\alpha_{\text{PDMS}}$  and  $\beta_{\text{PDMS}}$  combined is greater than that of  $\beta_{\text{PDMS}}$  alone. The  $\beta_{\text{PDMS}}$  value, by itself, allows the OPL to decrease by 0.7% over an 80° temperature increase. The coefficients combined would allow the OPL to increase 1.8% over the same temperature increase. Utilizing  $\alpha_{\text{PDMS}}$  would then more-than-double the temperature sensitivity.

This could be achieved by adding another minor step in the fabrication process. A flat, non-binding surface could be placed over the blazed grating after the PDMS is deposited. The excess PDMS would then be forced to exit out the sides as the surface is pressed down. After curing, the flat surface could be lifted, and the upper surface of the PDMS would be level with the upper part of the grating, as shown in Figure 45A. This would allow the PDMS to expand higher over its thicker parts (Figure 45B), enabling  $\alpha_{\text{PDMS}}$  to factor into the OPL equation. The separation of the PDMS between periods

would also disallow an unwanted flyback region. One factor that should be considered for such a design would be whether the reflection coefficient of gold changes when reflecting through a PDMS layer. If so, the intensity of reflection off the top step would vary from that of the lower steps, affecting the far-field pattern.

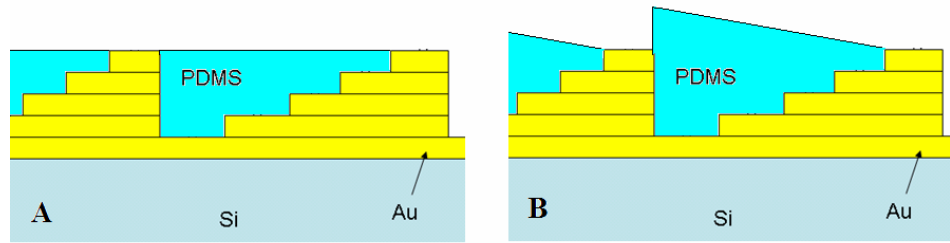


**Figure 45.** (A) Cross section showing a PDMS layer fabricated to align with the top part of the blazed grating. (B) Upon heating the PDMS would expand more where it's thicker, allowing  $\alpha_{\text{PDMS}}$  to factor into the OPL equation.

### 6.3.2 Continuous Steering

The VBG method of beam steering demonstrated here confines the beam to discrete, angular orders. This is a good feature for switching devices, but not for most beam steering requirements. Continuous control is necessary for functions such as scanning or random accessibility. Therefore, the angular confinement is generally a limitation rather than a benefit.

This angular confinement is determined by Equation 2.7, and is dependent on two parameters: the number of periods ( $N$ ) and period width ( $a$ ). Larger  $N$  means sharper angular confinement, and a larger  $a$  translates into less angular separation between orders. The only way to get continuous, or at least quasi-continuous, steering is to either decrease  $N$  to 1 (no periodicity) or to increase  $a$  until the angular separation between orders is sufficiently minimized.

The value of  $a$  could be increased, making the phase-reset distance very large. This requires the grating to maintain a sufficiently steep angle over a long period, which does pose a challenge in fabrication. A more pronounced drawback of this strategy would again be the tradeoff in response time. A larger period also decreases the maximum steering angle when a maximum phase shift of  $2\pi$  is achievable (a constraint of most LC steering devices).

An alternate method is to condense the beam. If it is incident on only one period, it will be continuously steerable. One of the challenges faced in simply focusing the beam to the desired spot is its divergence upon reflection. The challenge is shown in the diagram of setup two in Figure 36. A lens is placed a focal length away from the sample to re-focus the diverging beam into a relatively parallel wavefront. This has the added, and likely undesired, effect of also canceling the diffracted angle of the beam! This is because the origin of the diffraction is also a focal length away from the lens.

Rather than focus the beam onto the sample, it is likely desirable to condense it into a compact, but parallel form. There are multiple, commercially-available devices to perform this task for laser diodes [49], such as those shown in Figure 46.

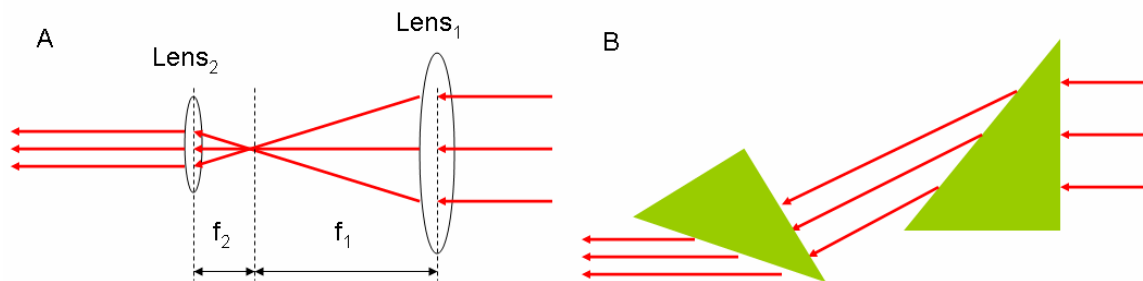


**Figure 46.** Beam condensing methods. A dual lens system (A) and anamorphic prisms (B).

This method has been considered for LC beam steering. Unfortunately, the steered angle of a condensed beam decreases when the beam is expanded due to Lagrangian principles [50].

### ***6.3.3 Alternate Methods of Temperature Control***

Three primary methods of heating control are discussed: Joule, radiated and microfluidic.

#### ***6.3.3.1 Joule Heating***

Joule heating is caused by a resistor absorbing power from current. The steady-state temperature,  $T_{ss}$ , of a material with resistance  $R_0$  and temperature coefficient of resistance,  $\alpha_R$ , can be described [51]:

$$T_{ss} = \frac{R_T V^2 / R_0}{1 + \alpha_R R_T V^2 / R_0} \text{ (°K)} \quad (6.1)$$

where  $V$  is the applied voltage and  $R_T$  is a thermal resistor representing the heat conduction from the resistor to a thermal reservoir.

Although gold is usually used as a conductor; long, thin wires can be used as resistors as well [52]. In this way, the underlying gold profile could be used for ohmic heating. This is provided it is sufficiently thin, isolated and connected to a source and ground. The current would not conduct through the PDMS because it is a very good insulator ( $\sigma_{PDMS} = 2.5 \cdot 10^{-14}$  S/m) [48]. The phase gradient of each period could likewise be controlled individually. A major constraint of this method would be that the phase change across each period would have to be a multiple of  $2\pi$  to ensure a continuous phase profile.



Another method would be to surround the PDMS with Joule-heated resistors on three sides. This would serve to maximize the PDMS surface area exposed to heat, maximizing the response time. A thick layer of PDMS could then be used to maximize the phase control with temperature. A diagram of such a design is shown in Figure 47.

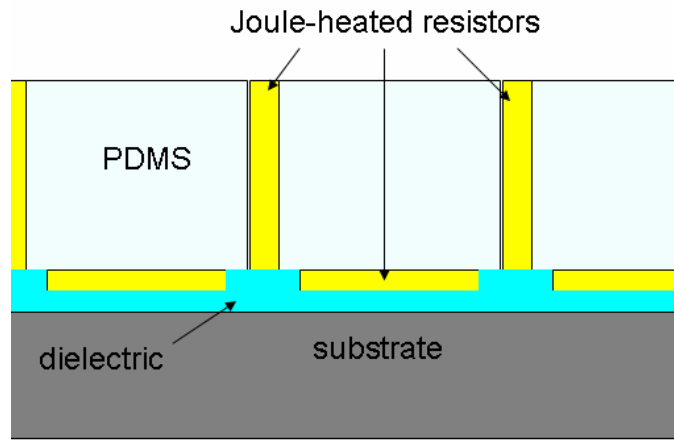


**Figure 47.** Thick PDMS layers are surrounded by isolated Joule-heaters on three sides, maximizing the dynamic response.

The resistors could be isolated by a dielectric material to heat individually. A deep reactive-ion etching (DRIE) process could allow the large aspect ratio (height-to-width). In this design, the temperature increase would increase the OPL through the PDMS because  $\alpha_{\text{PDMS}}$  would override  $\beta_{\text{PDMS}}$  [12]. The OPL for each PDMS layer could then be electrically controlled while maintaining isolation from adjacent layers, allowing period and phase-gradient control. A drawback of this method is that the interstitial resistors would detract from the efficiency of the far-field pattern. Also, the dimensions of such a device would likely limit it to angles less than those achievable by current LC technology.

Another similar method could use a trough or ‘corner-cube’ method with a PDMS fill and underlying Joule-heaters. The design would have to be such that the OPL for light entering, reflecting twice and leaving each pixel was the same for each entry point. This could be accomplished by bulk-etching pixels at 45° angles from the surface.

### 6.3.3.2 Radiation Heating

Another method of heating the PDMS is by thermal radiation, bypassing the need for the underlying, blazed profile. PDMS absorbs most in the long-wave IR (LWIR) as shown in Figure 48A. A periodic phase gradient could be defined in the PDMS by thermal diffraction patterns through multiple slits. The number of slits define the width of the diffraction fringes, so an effective step pattern could be radiated onto the PDMS as shown in Figure 48B. The blue and red radiation would likely be of the same LWIR wavelength, but are distinguished by colors for clarity.

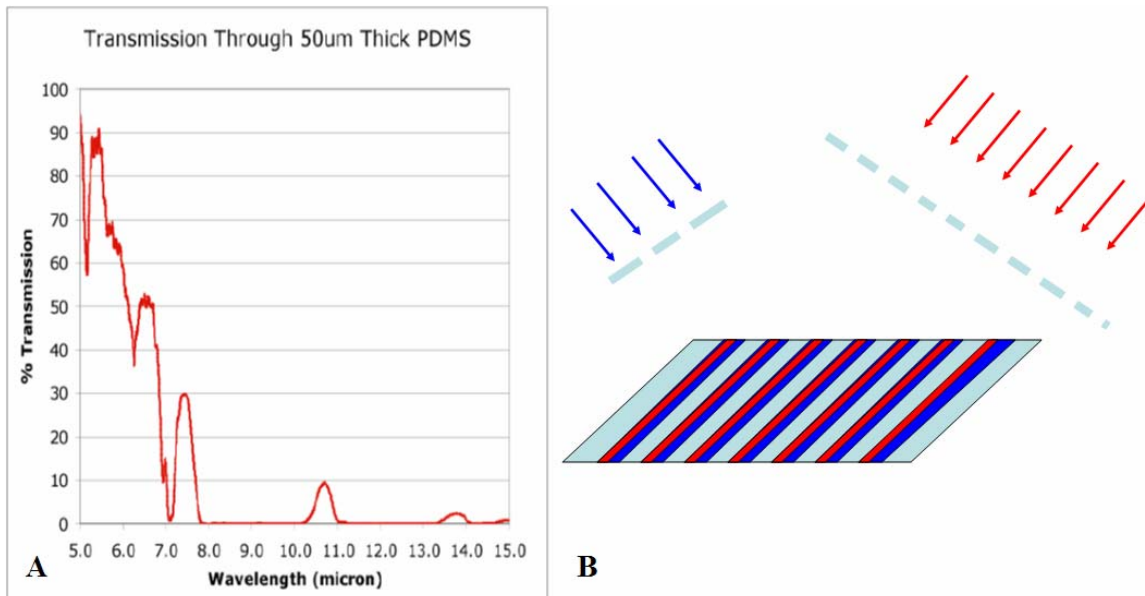


**Figure 48.** (A) Transmission spectrum of PDMS [53]. (B) Radiated heating of the PDMS layers by diffractive gratings. The red radiation is incident on more slits, so it creates a tighter fringe pattern.

The blue radiation is incident on two slits, creating relatively wide fringes. The separation to width ratio of the slits would be large enough ( $\sim 20$ ) to ensure similar amounts of power into each fringe. The red radiation would travel through more slits to create thinner fringes. The blue and red diffraction patterns would have matching periods as long as their slit separation is the same. The red pattern would then be offset slightly from the center of the blue to form a periodic stair-step temperature gradient in the PDMS. This of course translates into a periodic phase gradient for beam steering.

The gratings could be fabricated by MEMS technology, allowing electrical control of the slit separation, which would allow adjustment of the fringe pattern periodicity. An example of such a MEMS structure was presented in Chapter II [37]. Therefore, the period could be controlled by the MEMS, and the phase gradient could be determined by the intensity of the LWIR radiation.

#### ***6.3.3.3 Microfluidic Heating***

Microfluidic heating would allow very precise temperature control. Reservoirs of liquids at Joule-heating-controlled temperatures could be held outside the sample. The high heat-transfer rates in micro-scale allow easy implementation of uniform temperature conditions [54]. The fluid would be allowed to enter the PDMS through microscopic channels and a pumping mechanism. To maximize the surface area contact of the fluid and PDMS, and to minimize the adverse effect on reflection, a design similar to that of Figure 47 could be adopted. Rather than Joule-heated resistors, the interstitial layers would be tall, thin, microfluidic heating/cooling channels.

PDMS has actually become increasingly popular for creating microfluidic channels [55]! This is because its inexpensive and easy to fabricate by replica-molding under non-cleanroom conditions. When cured, PDMS faithfully replicates to its master with nm resolution (see Figure 49 for replication process). The master could be fabricated with an aspect ratio approaching 20 by DRIE or by using the negative PR, EPON SU-8, on a silicon wafer [56].

There are several methods used for microfluidic pumping: including electroosmosis, hydrodynamic focusing and valves. Electric fields can be used to separate species electrophoretically, creating a bulk flow known as electroosmosis [55]. Hydrodynamic focusing is achieved by applied pressure, or ‘squeezing’. Lastly, microfluidic chips have been developed with thousands of valves and hundreds of individually-addressable microchambers [57]. Given the necessary supplies and equipment, the realization of such a microfluidic mechanism of temperature control should be attainable.

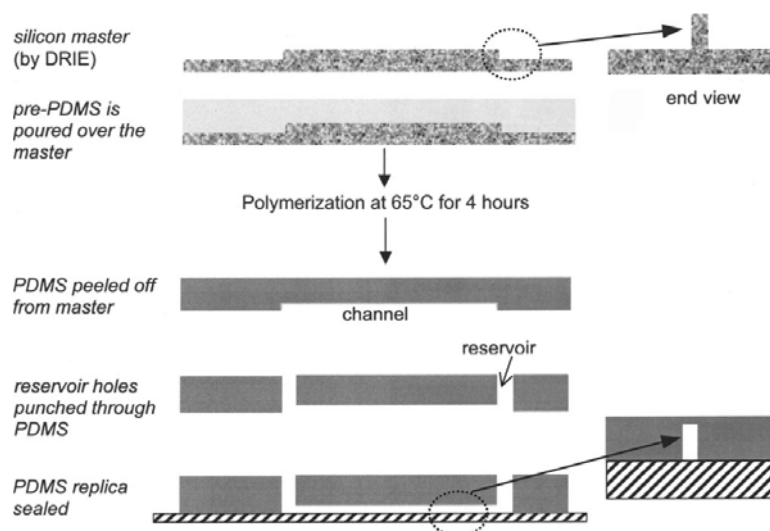


**Figure 49.** Replication of microchannels in PDMS using a Si master [58].

## **6.4 Summary**

A novel method for non-mechanical beam steering has been presented using a micro-scale device. It has been shown that a thermally-activated material can be used in this endeavor. Despite the limits of this proof-of-concept device, alternate designs and fabrication methods could be used to maximize the FOR and temperature sensitivity, as well as negate the discrete, angular limitations and response time. Further, this research demonstrated a method to circumvent the fringing field effect by negating the necessity for abrupt changes in the index of refraction. Lastly, the method demonstrated is orders of magnitude less complex and expensive than typical LC devices.



## Appendix A: Mask Design

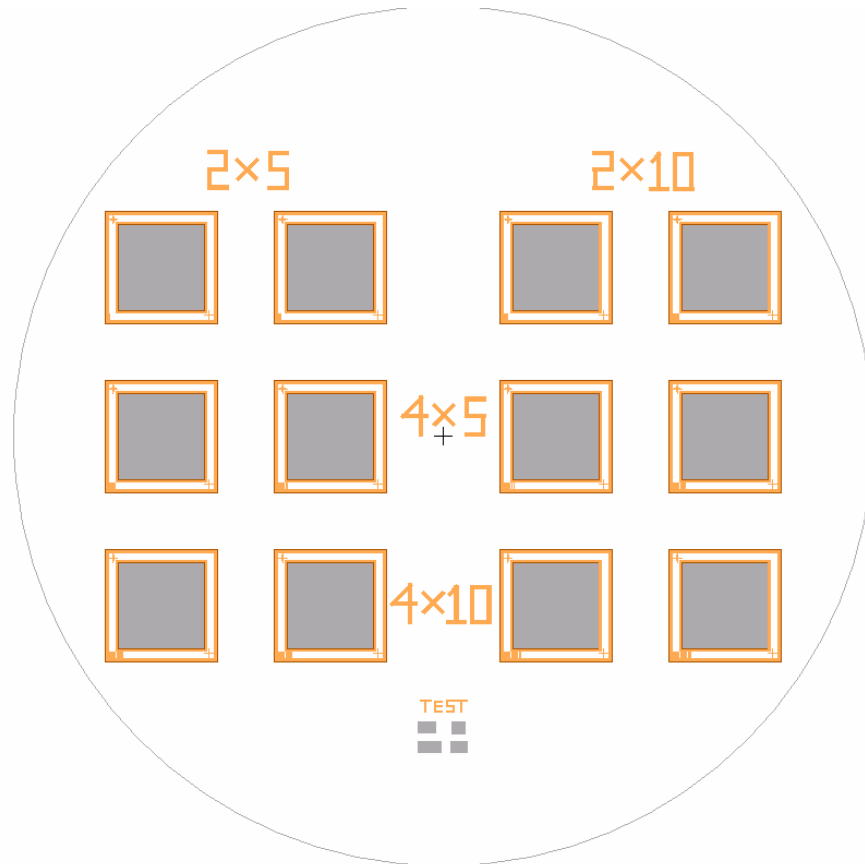


Figure A.1: Mask design

Manufacturer: Photo Science, Inc.

Layout: Designed using MEMSPRO L-edit ® layout editor. Used a single layer (Poly 0) for placement of metal on mask.

Mask Parameters: The substrate was soda lime, and the UV-blocking layer was chrome. The chrome layer was written with an L625 Heidelberg DWL 200/400 laser pattern generator.

Comments: The numbered labels correlate to the number of metal layers and spacing of each step. A pattern with 5  $\mu\text{m}$  spacing and a 15  $\mu\text{m}$  period corresponds to  $2 \times 5$ . The test section had 2 and 4  $\mu\text{m}$  patterns with 2 to 12  $\mu\text{m}$  spacing to determine the minimum thicknesses able to be exposed and developed well.





## Appendix B: MATLAB® Code

This appendix includes the MATLAB® m-files used in this thesis.

### B.1 Modeling of reflection off 10x30 sample

```
%Program:    Modeling of reflection off 10x30 sample
%Author:     1 Lt Matthew Johnson
%Project:    Master's Thesis
%Date:       3 Jan 2007
%Reference:  Master's Thesis, Lt Daniel Denninghoff, 11 Nov 2005

%The 10x30 sample is modeled alone here.  Similar methods were used for
%modeling the 10x50 and 5x25 samples

%% constants %%

lambda = 660*10^-9;           %660nm wavelength
k = 2*pi/lambda;
z = 1000*10^3;
T_room = 20;                  %degrees celcius

%% variable parameters %%

P = 3;                         %number of periods to simulate
theta = 13.5;                  %(degrees)
theta_radians = theta*2*pi/360; %converting from degrees to radians
T_plate = 20;                  %Temperature to simulate
alpha_Au = 14.2*10^-6;         %including gold expansion rate
Beta = -0.00010;               %beta value from literature
%Beta = -0.00012;              %experimentally determined beta value
n_PDMS_0 = 1.431;              %n value from literature
%n_PDMS_0 = 1.29;              %experimentally determined n value
N = 256;                       %number of pixels in x and y direction
grid_size = 2500*10^-6;        %optimized to desired angular range
width_x=10*10^-6;              %step width for modeling periodicity
width_y=100*10^-6;             %transmittance width in y-dimension
z_factor = 1                   %for setting normalized z axis limits

%% entering values from measurements %%

z_offset1 = 0.4504*10^-6;       %measured step heights (see Figure 28)
z_offset2 = 0.93578*10^-6;

w0 = 9.2125*10^-6;              %measured step widths (see Figure 29)
w1 = 9.673267*10^-6;
w2 = 8.960396*10^-6;

w_step1 = 0.77228*10^-6;        %widths between steps
w_step2 = 0.50495*10^-6;

w_step1_2_fb = 0*10^-6;         %step width in flyback region
```

```

w0 = w0*10^5; %adjusting widths to match coding scale
w1 = w1*10^5;
w2 = w2*10^5;
w_step1 = w_step1*10^5;
w_step2 = w_step2*10^5;
w_step1_2_fb = w_step1_2_fb*10^5;

%% defining n(T) and zoffset(T) %%

n_PDMS = n_PDMS_0 + Beta*(T_plate-T_room); %from equation 4.4
H = (1 + alpha_Au*(T_plate-T_room))*n_PDMS; %from equation 4.3
z2 = z-2*z_offset1*H/cos(theta_radians); %z_offset values for steps
z3 = z-2*z_offset2*H/cos(theta_radians); %2 and 3 (equation 4.3)

%% defining sample and detector grids %%

dx=grid_size/N;
[xs ys] = meshgrid((-N/2:N/2-1).*dx);

dx_det = lambda*z/grid_size;
[x_det y_det] = meshgrid((-N/2:N/2-1).*dx_det);

%% defining base step %%

U_ap1 = zeros(N);
for p = 1:P
    U_ap1((xs<(width_x*((p-1)*3+w0/2)) & xs>(width_x*((p-1)*3-w0/2))...
    & (abs(ys)<width_y/2))) = 1;
    U_ap1((xs>(-width_x*((p-1)*3+w0/2)) & xs<(-width_x*((p-1)*3-w0/2))...
    & (abs(ys)<width_y/2))) = 1;
end; %for loop defines step widths and periods
Angular_Spectrum = fftshift(fft2(fftshift(U_ap1)));
U1 = exp(i*k*z)*exp(i*k*(xs.^2+ys.^2)/(2*z)).*Angular_Spectrum...
/(i*lambda*z); %from equation 4.2

%% defining 2nd step %%

U_ap2 = zeros(N);
for p = 1:P
    U_ap2((xs<(width_x*((p-1)*3+w0/2+w_step1+w1)) &...
    xs>(width_x*((p-1)*3+w0/2+w_step1)) & (abs(ys)<width_y/2))) = 1;
    U_ap2((xs>(-width_x*((p-1)*3-(w0/2+w_step1))) &...
    xs<(-width_x*((p-1)*3-(w0/2+w_step1+w1))) & (abs(ys)<width_y/2))) = 1;
end;
Angular_Spectrum2 = fftshift(fft2(fftshift(U_ap2)));
U2 = exp(i*k*z2)*exp(i*k*(xs.^2+ys.^2)/(2*z2))...
.*Angular_Spectrum2/(i*lambda*z2);

%% adding 3rd step %%

U_ap3 = zeros(N);
for p = 1:P
    U_ap3((xs<(width_x*((p-1)*3+w0/2+(w_step1+w1+w_step2+w2))) &...
    xs>(width_x*((p-1)*3+w0/2+(w_step1+w1+w_step2))) &...
    (abs(ys)<width_y/2))) = 1;
    U_ap3((xs>(-width_x*((p-1)*3-(w0/2+(w_step1+w1+w_step2))) &...
    xs<(-width_x*((p-1)*3-(w0/2+(w_step1+w1+w_step2+w2))) &...
    (abs(ys)<width_y/2))) = 1;
end;

```

```

Angular_Spectrum3 = fftshift(fft2(fftshift(U_ap3)));
U3 = exp(i*k*z3)*exp(i*k*(xs.^2+ys.^2)/(2*z3))...
.*Angular_Spectrum3/(i*lambda*z3);

%% adding complex fields and solving for far-field intensity %%

U_total = U1 + U2 + U3; %from equation 4.1
Intensity_total = U_total.^2; %from equation 4.1
if T_plate == 20
    I_max_10x30 = z_factor*max(max(abs(Intensity_total)));
end;
Intensity_total = Intensity_total./I_max_10x30;
%normalized intensity relative to value at T_plate = T_room

%% plotting in 3D %%

figure (1)
clf reset;
colormap hot;
angle_steered_x = atan(x_det/z)*360/(2*pi); %translating from x and y
angle_y = atan(y_det/z)*360/(2*pi); %values to angular values
surfl(angle_steered_x, angle_y, abs(Intensity_total), 'light');
shading interp; colormap hot; caxis([0 1]);
title(['10x30 Tplate = ' num2str(round(T_plate)) ' \circC']);
zlabel('Intensity (normalized)');
xlabel('X Angle (\circ)');
ylabel('Y Angle (\circ)');

```

## B.2 CCD camera data display

```

%Program:    CCD camera display
%Author:     1Lt Matthew Johnson
%Project:    Master's Thesis
%Date:       3 Jan 2007
%Reference:  Master's Thesis, Lt Daniel Denninghoff, 11 Nov 2005

File_name = '5x25/5x25_32mA_3ND_175C.bmp'; %input file name here
sample = '10x50';
I = 32; %intensity in mA
T = 175; %temperature in Celcius
scale_factor = 1/80; %converting from pixels to
degrees

A = importdata(File_name); %get data
B = double(A.cdata); %convert data
B(480,1:640) = 0; %shifting data to put zero
order in middle
C = zeros(480,640);

C(1:480,600:640) = B(1:480,562:602);
C(1:480,1:38) = B(1:480,603:640);
C(1:480,39:599) = B(1:480,1:561);

X_axis = 1:640;
X_axis_scaled = (X_axis-320)*scale_factor;

```

```

Y_axis = 1:480;
Y_axis_scaled = (Y_axis-240)*scale_factor;

C_scaled = C/256;

%% plotting surface graph %%

figure(2)
clf;

surfl(X_axis_scaled, Y_axis_scaled, C_scaled, 'light');
shading interp; colormap hot; caxis([0 1]);
title([sample, ' sample'],...
      ['Diffraction Pattern at ',num2str(T),'\circ C'],...
      ['I = ',num2str(I), ' mA ND = 3.0 Filter']],...
      'fontsize',12);
AXIS([-320*scale_factor 320*scale_factor -240*scale_factor
240*scale_factor 0 1]);
zlabel('Intensity (normalized)');
xlabel('Angle (\circ)');
ylabel('Angle (\circ)');

%% plotting imagesc graph %%

figure(1)
clf;
imagesc(X_axis_scaled, Y_axis_scaled, C); colormap hot; caxis([0 256])
title([sample, ' sample'],...
      ['Diffraction Pattern at ',num2str(T),'\circ C'],...
      ['I = ',num2str(I), ' mA ND = 3.0 Filter']],...
      'fontsize',12);
axis xy;
xlabel('Angle (\circ)');
ylabel('Angle (\circ)');

```

## Appendix C: Alternative Fabrication Method and Results

An alternate fabrication method was performed due to the difficulties initially encountered with using the lift-off method. Rather than lifting off the gold on top of the PR, it was allowed to stay. The fabrication concept is shown in Figure 50. The benefit of this process was simplicity and large step heights.

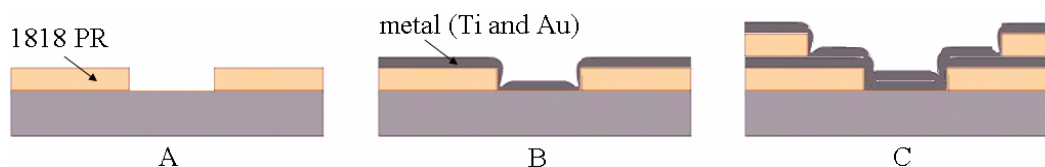


**Figure 50.** Alternative fabrication method. Metal is deposited on top of the patterned PR. The metal is left and another layer is added for the next step.

The 1818 PR provides a fairly even layer,  $1.9\text{ }\mu\text{m}$  thick, at 4000 RPM with a standard thickness deviation of  $207\text{ }\text{\AA}$ . The PR was exposed at  $275\text{ Watts/cm}^2$  for 15 seconds. It was then developed in a 1:5 mixture of 351 and deionized water. Finally, Ti and gold layers were deposited in the EBE.

In this way, the steps were created out of 1818 PR. The PR provides a large step height that would have taken several hours to create by depositing metal. Only one layer of resist was deposited, as compared to the four or five layers necessary for the lift-off method. Another benefit of this method was that none of the steps were inadvertently lifted off. The periodic step profile was therefore continuous across the sample, as partly shown in Figure 51.

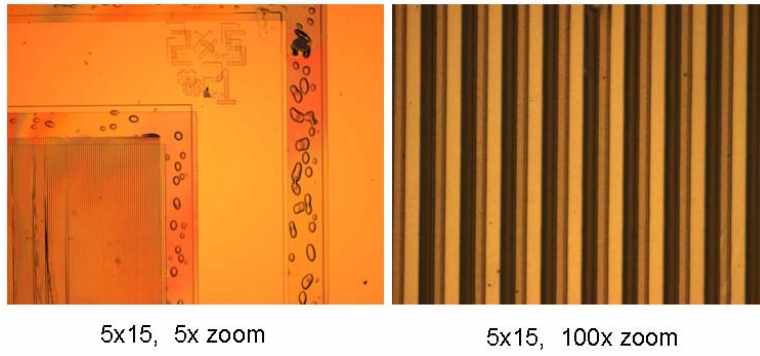


**Figure 51.** Microscope pictures before the second metallization step. Although the periods matched, the 5K zoom shows the sample was not aligned exactly in the x and y directions. The 100x zoom shows good alignment for the second step, with the new 1818 PR layer covering half of the first-step mesa.

The step profile achieved by the alternative method for the 5x15 and 10x30 samples is shown in Figure 52.

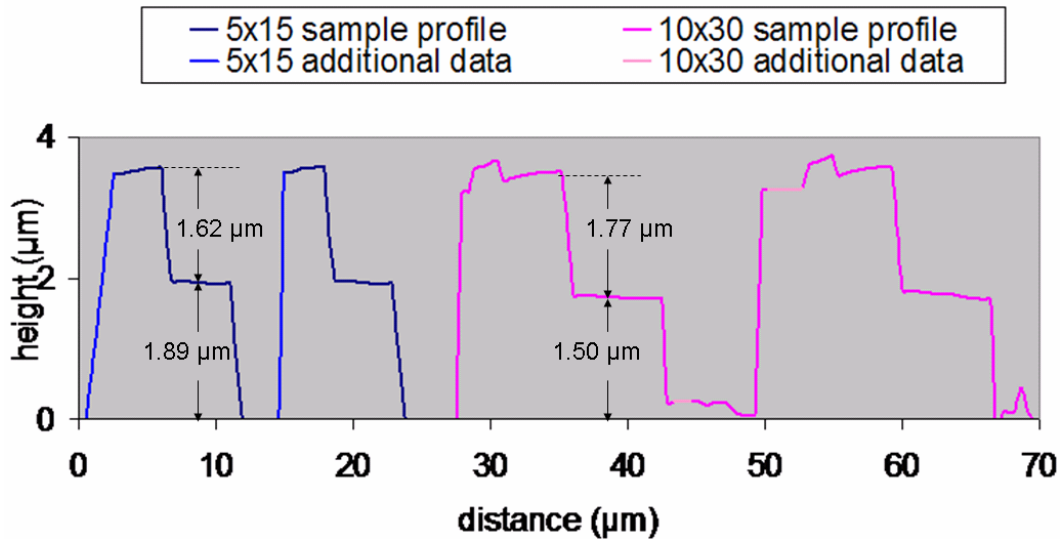


**Figure 52.** Step profile of 5x15 (blue) and 10x30 (magenta) samples fabricated using the alternative method. Because the Zygo ® interferometer was not able to capture the entire profile at this small scale, the expected profile is added (lighter colors).

The phase shifts (assuming  $n = 1$ ) at 660 nm for the 1<sup>st</sup> and 2<sup>nd</sup> steps are 266 and 171 ° for the 5x15 sample and 196 and 33 ° for the 10x30 sample, respectively.

Although the steps appear relatively similar in height, they do not provide the desired

linear phase profile. This significantly inhibits the ability of the device to provide predictable, concentrated diffraction. The lack of step-height accuracy is due to the fabrication method, because the PR thickness cannot be accurately controlled to the necessary level of fidelity.

The 10x30 sample was tested under a setup similar to that shown in Figure 34. The laser was not focused on the chip; however, because the periodic profile was consistent across the device. The beam was therefore allowed to cover about half of the  $\text{cm}^2$  sample.

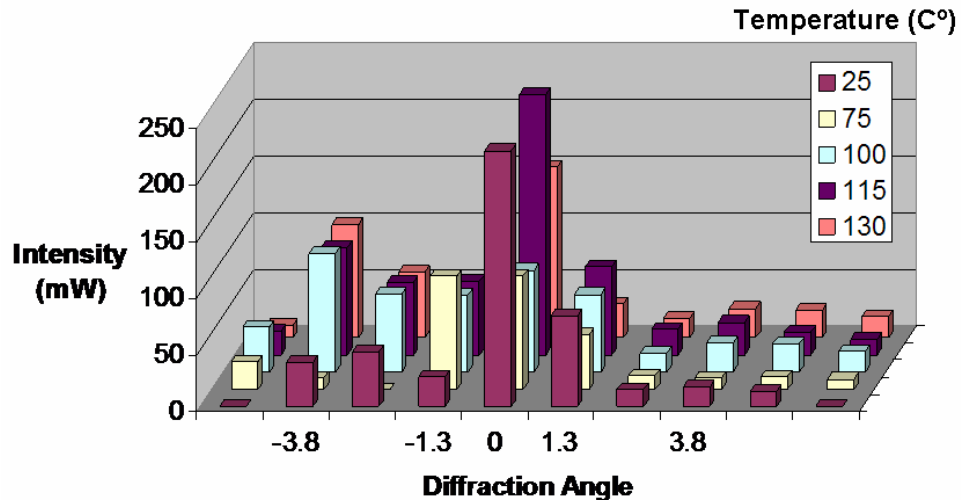


**Figure 53.** Experimental intensity measurements from the 10x30 sample, fabricated with the alternate method. There is a shift towards the negative third order with increasing temperature.

The beam was diffracted into orders separated by  $1.26^\circ$  as was expected from the  $\lambda$  and  $w$  values. There is a notable shift from the zero to the negative third order as the temperature increases. As shown in chapter V, the  $\beta_{\text{PDMS}}$  value causes the beam to shift to the right. The shift to the left seen here must therefore be from the competing thermal

expansion of the PDMS. This leads to the conclusion that  $\alpha_{\text{PDMS}}$  was overriding  $\beta_{\text{PDMS}}$  for this sample. The  $\alpha_{\text{PDMS}}$  value is allowed to contribute in this setup because the step heights are much larger proportionally to the PDMS thickness. This allows the PDMS to ‘conformally’ expand more where it is thicker, as shown in Figure 19B.



## Appendix D: Modeling and Experimental Results of the 5x25 Sample

The results from setup one for the 5x25 sample are shown in Figure 54. The intensity is a little towards the first order at 20 °C, then shifts slightly towards the negative first order with increasing temperature.

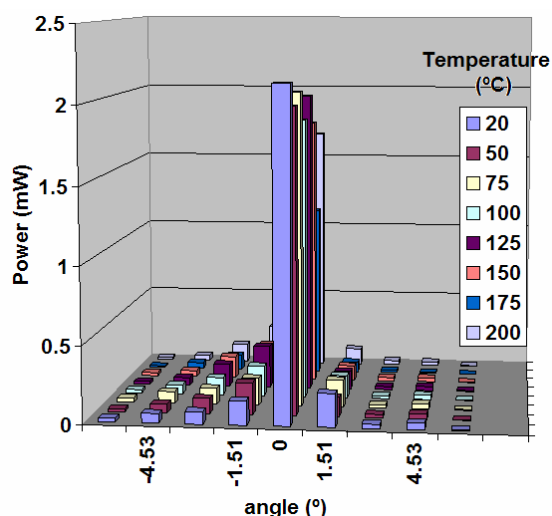


**Figure 54.** Experimental results of setup one for the 5x25 sample. The intensity seems to be a little towards the first order at 20 °C, then shifts slightly towards the negative first order with increasing temperature.

The beam was expected to shift left because the step profile for the 5x25 sample was actually fabricated in the reverse direction. Figure 55 shows that the first order intensity slightly decreased, and the negative first order intensity slightly increased with temperature. The shift was considerably less than expected. This is likely due to the PDMS layer being compromised by inadvertently contacting the hot plate surface. For more conclusive results; a new PDMS layer could be deposited and the sample retested.

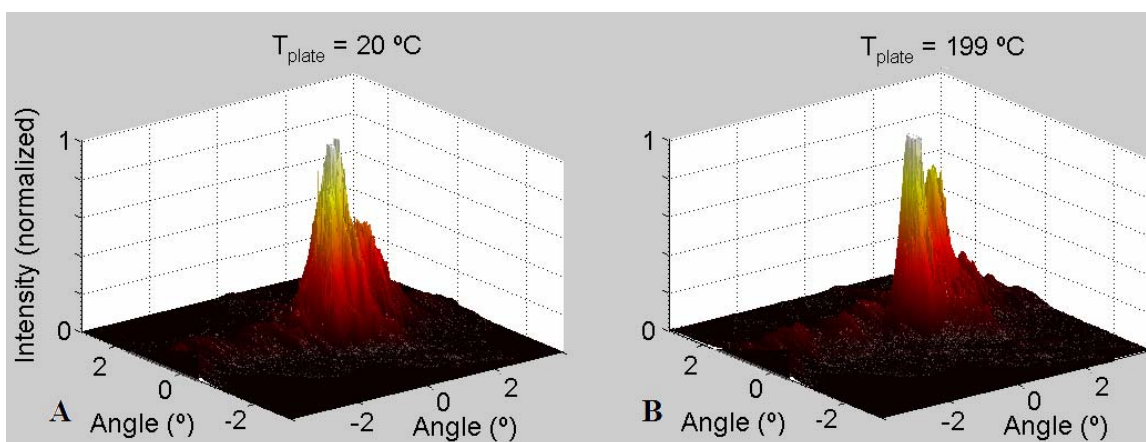


**Figure 55.** Beam profile of reflection off the 5x25 sample at 20 and 199 °C.

## Appendix E: Temperature-Variance Modeling

The temperature gradient of the PDMS was modeled through Coventorware™, a finite-element modeling program. This temperature gradient is shown here to provide a more accurate value for the OPL of each step. The model was updated from the one shown in Figure 32B by using the exact heights measured for each step of the 10x50 sample. The model was then divided into several elements as shown by the mesh model in Figure 56A. The The elements were 5 and 0.5  $\mu\text{m}$  wide in the x and z direction, respectively. The z direction was divided with the most fidelity, because  $dT/dz$  is primary value being sought. The  $dT/dx$  values are also important because the OPL's are found for the steps, which are separated in the x direction. The y direction is least relevant. This is reflected in the few divisions along this dimension in the mesh model, which saves computation time.

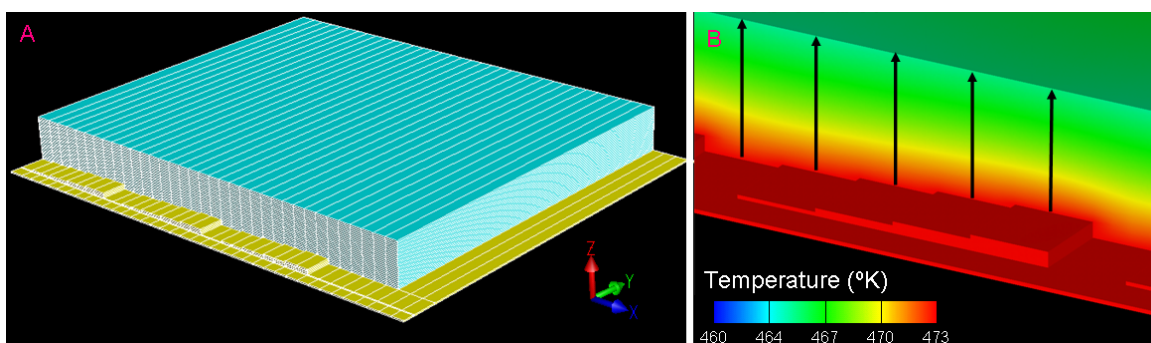


**Figure 56.** (A) Mesh model for 10x50 sample. (B) Model of temperature gradient when the substrate is heated to 473 °K (200 °C). The black arrows show where the temperature gradient was extracted for calculation of the OPL through each step. Modeled in Coventorware™.

Figure 56B shows the steady-state temperature gradient with the underlying substrate is heated to 200 °C. The ambient temperature surrounding the PDMS was set to

20 °C (room temperature), and an ambient air flow of 1 m/sec was simulated. The black arrows show where the temperature values,  $T(z_p)$ , were extracted for calculation of the OPL through each step, where  $z_p$  is the  $z$  distance for the  $p$ , the extracted point number. The data was taken over 200 points for each OPL and is shown in Figure 57.

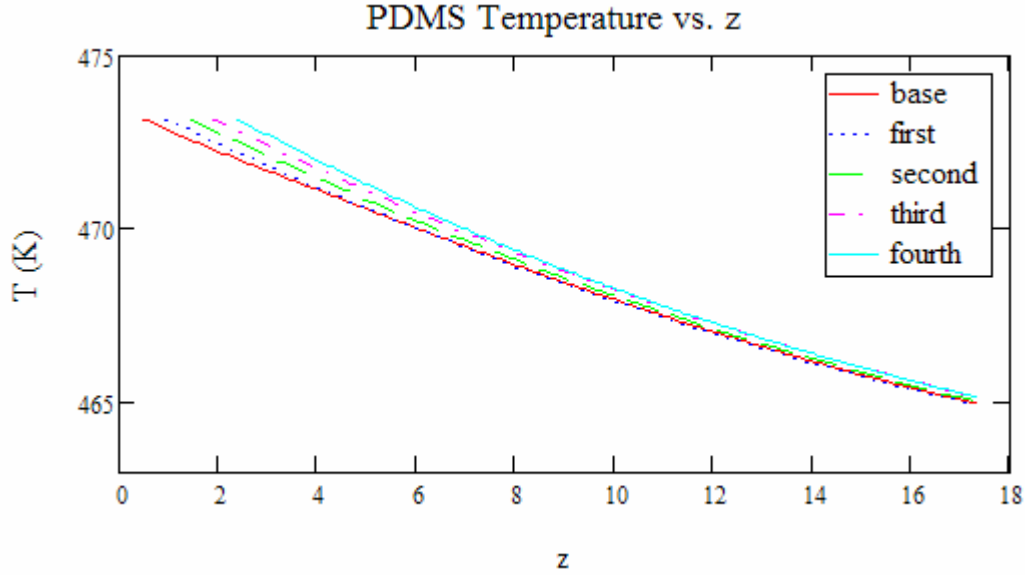


**Figure 57.** The temperature vs. height ( $z$ ) from the gold bottom is shown for each step.

The OPLs were calculated by integrating the changing  $n_{\text{PDMS}}(T(z_p))$  values over  $z_p$ :

$$\text{OPL} = \sum_{p=1}^{200} \frac{2n_{\text{PDMS}}[T(z_p)] \Delta z(z_p)}{\cos(\theta_{\text{incident}})} \quad (\text{E.1})$$

where  $\Delta z(z_p)$  is the  $z$  distance between midpoints surrounding each extracted point and  $n_{\text{PDMS}}[T(z_p)]$  is found by Equation 4.4. The OPLs for each step were then entered into the MATLAB™ code explained in Chapter IV. The far-field intensity is shown in Figure 58 when the temperature gradient is included and when it is not. The modeling shows a

slight decrease in the steering angle of the envelope function (more intensity remains in the zero order) when the temperature gradient is included.

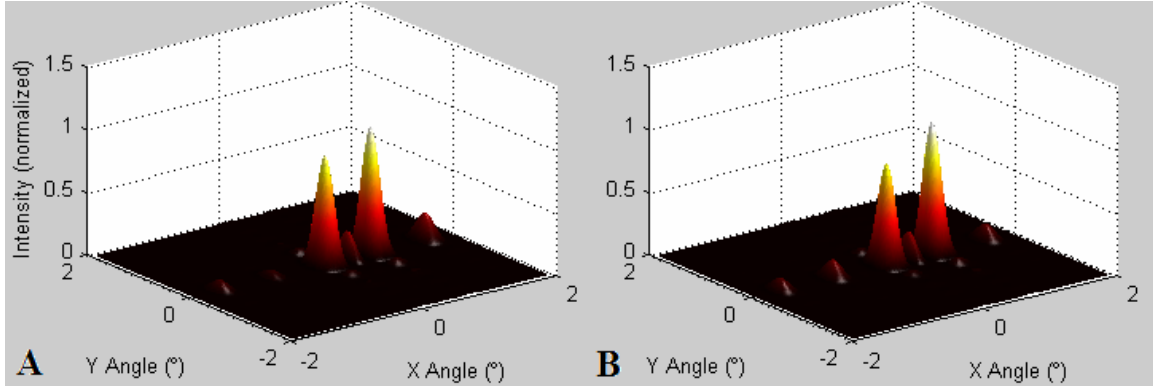


**Figure 58.** (A) The far-field intensity pattern modeled when the temperature gradient is included and (B) when a constant temperature is used. A slightly decreased steering angle of the envelope function is shown when the temperature gradient is included.

The OPL difference for each step at increasing temperatures is therefore slightly smaller when the temperature gradient is modeled than when it is not. This cannot be safely applied to the experimentally-determined  $\beta_{\text{PDMS}}$  value because an air flow was not established across the device during testing. If it was, the air flow could be accurately simulated to provide the temperature gradient.

A higher-fidelity model could integrate the temperature over both the x and z axes. Several OPLs could be found at different x values across each step. Each of these would then be modeled for its given width ( $\Delta x$ ) by its own reflectance function.

## Bibliography

- [1] Yuichi Ninomiya, "Ultrahigh Resolving Electrooptic Prism Array Light Deflectors," *IEEE Journal of Quantum Electronics*, vol. QE-9, no. 8, August 1973, pp. 791-795.
- [2] Paul McManamon, Terry Dorschner, David Corkum, Larry Friedman, Douglas Hobbs, Michael Holz, Sergey Liberman, Huy Nguyen, Daniel Resler, Richard Sharp, and Edward Watson, "Optical Phased Array Technology," in *Proceedings of the IEEE*, vol. 84, no. 2, February 1996, pp. 268-298.
- [3] Michael Holz and Terry Dorschner, "Optical multi-access satellite communications, leveraging emerging OPA technology for laser communications," *Technology today, highlighting Raytheon's technology*, Issue 2, 2005.
- [4] "Adaptive Optics," class notes for Astronomy 289C, Department of Astronomy and Astrophysics, University of California, Santa Cruz, CA, Spring 2006.
- [5] Iam-Choon Khoo. *Liquid Crystals, Physical Properties and Nonlinear Optical Phenomena*. Canterbury, UK: John Wiley and Sons, Inc., Ch 1-3, 1995.
- [6] Paul McManamon, "An overview of optical phased array technology and status," in *Proceedings of SPIE*, vol. 5947, 59470I, 2005.
- [7] Boulder Nonlinear Systems, Inc. Technical Staff, *Spatial Light Modulators 1 x 12,488 Linear Series Draft Data Sheet*, Boulder Nonlinear Systems, Inc., April 2006.
- [8] Hans Dieter Tholl, "Novel laser beam steering techniques," in *Proceedings of SPIE*, Vol. 6397, 639708, 2006.
- [9] U. Efron, B. Apte3r, R. Israeli, I. David, and Baal-Zedaka, "Recent studies in LC devices and technology," in *Proceedings of SPIE*, Vol. 6332, 63320K, 2006
- [10] Boulder Nonlinear Systems, Lafayette, CO, "Boulder Nonlinear Systems developing optical technology for NASA Langley," August 2003, <http://www.bnonlinear.com/news/0803.htm>.
- [11] Wikipedia, the Free Encyclopedia, "Polydimethylsiloxane," Jan 2007, <http://en.wikipedia.org/wiki/Polydimethylsiloxane>
- [12] Bartosz A. Grzybowski, Scott T. Brittain, and George M. Whitesides, "Thermally actuated interferometric sensors based on thermal expansion of transparent

elastomeric media,” *Review of Scientific Instruments*, vol. 70, no. 4, April 1999, pp. 2031-2037.

- [13] Joseph W. Goodman, *Introduction to Fourier Optics*. Englewood, Colorado: Roberts and Company Publishers, 2005.
- [14] Mark Gruneisen, Lewis DeSandre, James Rotge, Raymond Dymale, and Donald Lubin, “Programmable diffractive optics for wide-dynamic-range wavefront control using liquid-crystal spatial light modulators,” *Optical Engineering*, vol. 43, no. 6, June 2004, pp. 1387-1393.
- [15] "Fraunhofer Diffraction," class notes for PHYS 640, Department of Engineering Physics, Air Force Institute of Technology, Fall 2005.
- [16] Eugene Hecht, *Optics*. San Francisco, CA: Pearson Education, Inc., 2002.
- [17] Matthew Hunwardsen, Rockwell Scientific Company, Thousand Oaks, CA, “Optical phased array improves liquid crystal devices used in laser beam steering subsystems,” March 2004, <http://www.nasatech.com/Briefs/Mar04/UEI0304.html>.
- [18] Paul McManamon, Jianru Shi, and Philip J. Bos, “Broadband optical phased-array beam steering,” *Optical Engineering*, vol. 44(12), 128004, December 2005.
- [19] Edward A. Watson and Paul F. McManamon, “Application of dynamic gratings to broad spectral band beam steering,” in *Proceedings of the SPIE*, vol. 2120, 1994, pp. 178-185.
- [20] Edward A. Watson and Lawrence J. Barnes, “Optical design considerations for agile beam steering,” in *Proceedings of the IEEE*, vol. 2120, 1994, pp. 186-192.
- [21] H. Damman, “Spectral characteristics of stepped-phase gratings,” *Optik*, vol. 53, 1979, pp. 409-417.
- [22] Wikipedia, the Free Encyclopedia, “Phased Array ,” Jan 2007, [http://en.wikipedia.org/wiki/Phased\\_array](http://en.wikipedia.org/wiki/Phased_array)
- [23] R. A. Meyer, “Optical beam steering using a multichannel lithium tantalite crystal,” *Applied Optics*, vol. 11, no. 3, March 1972, pp. 613-616.
- [24] Roy M. Matic, “Blazed phase liquid crystal beam steering,” in *Proceedings of the SPIE*, vol. 2120, 1994, pp. 194-205.
- [25] Terry A. Dorschner, Larry J. Friedman, Michael Holz, Daniel P. Resler, Richard C. Sharp, and Irl W. Smith, “An optical phased array for lasers,” in *Proceedings of the*

*IEEE International Symposium on Phased Array Systems and Technology*, 1996, pp. 5-10.

- [26] David M. Burns, Victor M. Bright, Steven C. Gustafson, and Edward A. Watson, "Optical beam steering using surface micromachined gratings and optical phased arrays," in *Proceedings of the SPIE*, vol. 3131, 1997, pp. 99-110.
- [27] Xu Wang, Optical Information Processing Laboratory, Dept. of Electrical Engineering, California Institute of Technology, Pasadena, CA, "Liquid crystal used in beam steering device," December 1998, <http://www.spie.org/web/oer/december/dec98/opctg.html>.
- [28] Xu Wang, Daniel Wilson, Richard Muller, Paul Maker, and Demetri Psaltis, "Liquid-crystal blazed-grating beam deflector," *Applied Optics*, vol. 39, no. 35, December 2000, pp. 6545-6555.
- [29] Sang Hwa Kim and Liang-Chy Chien, "Liquid crystal blazed gratings formed in a single step through photo-induced localization of polymer into a prismatic structure," *Optics Express*, vol. 12, no. 7, April 2004, pp. 1238-1242.
- [30] K. E. Peterson, "Silicon as a Mechanical Material," in *Proceedings of the IEEE*, vol. 70, no. 5, pp. 420-457, May 1982.
- [31] Asif Godil, Lightconnect, Newark, CA, "Diffractive MEMS," 2002, [http://www.lightconnect.com/technology/Diffractive\\_MEMS.pdf](http://www.lightconnect.com/technology/Diffractive_MEMS.pdf).
- [32] Lightconnect, Newark, CA, "Diffractive MEMS," <http://www.lightconnect.com/technology/DMEMSWhitePaper3.pdf>.
- [33] Jahja I. Trisnadi, Clinton B. Carlisle, and Robert Monteverde, "Overview and applications of Grating Light Valve™ based optical write engines for high-speed digital imaging," presented at Photonics West 2004 – Micromachining and Microfabrication Symposium, San Jose, CA, 2004.
- [34] S. Kim, G. Barbastathis, and H. L. Tuller, "MEMS for optical functionality," *Journal of Electroceramics*, vol. 12, 2004, pp. 133-144.
- [35] Larry J. Hornbeck, "From Cathode Rays to Digital Micromirrors: A History of Electronic Projection Display Technology," *TI Technical Journal*, pp. 7-46, Jul-Sep 1998.
- [36] G. B. Hocker, D. Youngner, E. Deutsch, A. Volpicelli, S. Senturia, M. Butler, M. Sinclair, T. Plowman, and A. J. Ricco, "The polychromator, a programmable MEMS diffraction grating for synthetic spectra," DOE's Office of Scientific and Technical Information, Office of Science, Oak Ridge, TN, Tech. Rep. 0975C, 2000.



- [37] Maurizio Tormen, Yves-Alain Peter, Philippe Niedermann, Arno Hoogerwerf, Herbert Shea, and Ross Stanley, "Deformable MEMS grating for wide tunability and high operating speed," in *Proceedings of SPIE*, vol. 6114, 61140C, 2006.
- [38] AGILOPTICS, Albuquerque, NM, "Superior AO technology, solving today's most demanding optical problems," no date [February 2006], [http://www.optoprim.de/catalogs/AgilOptics\\_brochure.pdf](http://www.optoprim.de/catalogs/AgilOptics_brochure.pdf)
- [39] Pantazis Mouroulis, Frank Hartley, Daniel Wilson, Victor White, Aidan Shori, Steven Nguyen, Min Zhang, and Martin Feldman, "Blazed grating fabrication through gray-scale Xray lithography," *Optics Express*, Vol. 11, Issue 3, pp. 270-281, Feb 2003.
- [40] Guna Seetharaman, PhD (private communication), 2006.
- [41] Dow Corning Technical Staff, "Information about Dow Corning® brand silicone encapsulants," Dow Corning Electronics Solutions, Form No. 10-898F-01, 2005
- [42] Gregory T.A. Kovacs, *Micromachined Transducers Sourcebook*. United States of America: The McGraw-Hill Companies, Inc., 1998.
- [43] MicroChem Corp. Technical Staff, *LOR Lift-Off Resists*, MicroChem Corp., 2002
- [44] "Standard Photolithography and Pre-Metallization Recipes," class notes for EENG 717, Department of Electrical Engineering, Air Force Institute of Technology, Dayton, OH, Spring 2006.
- [45] Matthew Johnson and Karl Schwenn, "EENG 717, Lab Report 3 and 4," Air Force Institute of Technology, Dayton, OH, 2006.
- [46] J. Cooper Mcdonald and George M. Whitesides, "Poly(dimethylsiloxane) as a material for fabricating microfluidic devices," *Accounts of Chemical Research*, vol. 35, no. 7, pp. 491-499, July 2002.
- [47] Lalgudi Natarajan, PhD (private communication), 2006.
- [48] Carol Livermore and Joel Voldman, Massachusetts Institute of Technology, "Material Property Database, Material: PDMS" March 2004, <http://web.mit.edu/6.777/www/matprops/pdms.htm>.
- [49] Melles Griot Technical Staff, "Characteristics of Efficient Diode Laser Collimators," Melles Griot.
- [50] Edward Watson, PhD (private communication), 2007.

- [51] Stephen D. Senturia, Microsystem Design, Kluwer Academic Publishers, 2000.
- [52] Major LaVern Starman, PhD (private communication), 2006.
- [53] Raviv Perahia and Thomas Watson, “Design and Fabrication of Integrated Microfluidic and Mid-IR Quantum Cascade Laser Chips,” presented at DARPA Center for Optofluidic Integration Retreat, Harvard University, 2006.
- [54] K. Jensen, “Microreaction engineering—Is smaller better?,” *Chemical Engineering Science*, vol. 56, pp. 293-303, 2001.
- [55] Elisabeth Verpoorte and Nico De Rooij, “Microfluidics and MEMS,” in *Proceedings of the IEEE*, vol. 91, no. 6, pp. 930-953, June 2003.
- [56] H. Lorenz, M. Despont, N. Fahrni, N. LaBianca, P. Renaud, and P. Renaud, “High-aspect-ratio, ultrathick, negative-tone near-UV photoresist and its applications for MEMS,” *Sensors and Actuators A*, vol. 64, pp. 33-39, 1998.
- [57] T. Thorsen, S. Maerkl, and S. Quake, “Microfluidic large-scale integration,” *Science*, vol. 298, pp. 580-584, 2002.
- [58] B. Jo, L. Van Lerberghe, K Motsegood, and D. Beebe, “Three-dimensional micro-channel fabrication in polydimethylsiloxane (PDMS) elastomer,” *Journal of Microelectromechanical Systems*, vol. 9, pp. 76-81, 2000.

## **Vita**

Matthew Johnson was born in Oregon in 1980 and raised with his two brothers in Roseburg, Oregon. Upon graduating from Roseburg High School in 1998, Matthew attended Oregon State University. After receiving his Bachelor of Science Degree in Electrical Engineering in 2002, he was commissioned in the US Air Force in 2003. His first assignment was as a program manager in the Electronic Systems Center at Hanscom AFB, Massachusetts. He was then selected for the electro-optics master's degree program at AFIT. Following graduation, he is assigned to work as a developmental engineer in the Air Force Research Laboratory Munitions Directorate at Eglin AFB, Florida.

REPORT DOCUMENTATION PAGE				Form Approved OMB No. 074-0188	
<p>The public reporting burden for this collection of information is estimated to average 1 hour per response, including the time for reviewing instructions, searching existing data sources, gathering and maintaining the data needed, and completing and reviewing the collection of information. Send comments regarding this burden estimate or any other aspect of the collection of information, including suggestions for reducing this burden to Department of Defense, Washington Headquarters Services, Directorate for Information Operations and Reports (0704-0188), 1215 Jefferson Davis Highway, Suite 1204, Arlington, VA 22202-4302. Respondents should be aware that notwithstanding any other provision of law, no person shall be subject to a penalty for failing to comply with a collection of information if it does not display a currently valid OMB control number.</p> <p><b>PLEASE DO NOT RETURN YOUR FORM TO THE ABOVE ADDRESS.</b></p>					
1. REPORT DATE (DD-MM-YYYY) 22-03-2007		2. REPORT TYPE Master's Thesis		3. DATES COVERED (From - To) Aug 2005 - March 2007	
4. TITLE AND SUBTITLE  THERMALLY ACTIVATED, VARIABLE BLAZED GRATING FOR COHERENT BEAM STEERING				5a. CONTRACT NUMBER	
				5b. GRANT NUMBER	
				5c. PROGRAM ELEMENT NUMBER	
6. AUTHOR(S)  Johnson, Matthew, T., First Lieutenant, USAF				5d. PROJECT NUMBER N/A	
				5e. TASK NUMBER	
				5f. WORK UNIT NUMBER	
7. PERFORMING ORGANIZATION NAMES(S) AND ADDRESS(S) Air Force Institute of Technology Graduate School of Engineering and Management (AFIT/EN) 2950 Hobson Way, Building 640 WPAFB OH 45433-8865				8. PERFORMING ORGANIZATION REPORT NUMBER  AFIT/GEO/ENG/07-04	
9. SPONSORING/MONITORING AGENCY NAME(S) AND ADDRESS(ES) N/A				10. SPONSOR/MONITOR'S ACRONYM(S)	
				11. SPONSOR/MONITOR'S REPORT NUMBER(S)	
12. DISTRIBUTION/AVAILABILITY STATEMENT  APPROVED FOR PUBLIC RELEASE; DISTRIBUTION UNLIMITED.					
13. SUPPLEMENTARY NOTES					
14. ABSTRACT <p>The ability to perform non-mechanical optical beam steering is of critical importance in laser communication and remote sensing; it is as vital as a phased-array antenna is for RADAR. Directed energy transmission and direction-selective reception increase performance and produce tactical advantage in DoD applications. However, specific geometric features of non-mechanical beam steering devices must be designed in proportion to the wavelength of the monochromatic light to be steered. Also, the ability to handle higher energies by reducing the energy per unit requires large areas of uniform properties on the micrometer scale. These challenges have been addressed in the past using liquid crystals (LC) to produce a peak steering angle of 4 degrees, albeit limited by problems due to the fringing field effect. Recent advances in micro-fabrication techniques, including the synthesis and manipulation of certain electro- and thermo-optic materials, hold new opportunities for efficient beam steering solutions. The objective of this thesis research is to demonstrate thermally controllable beam steering, and enable further investigation of efficiency and response time and their dependence on geometry. The design, fabrication and performance of such a thermally-activated, non-mechanical beam steering device is demonstrated for the first time herein. The elastomeric media, polydimethylsiloxane (PDMS), was used as the active, phase-controlling agent. Its temperature-dependent index of refraction was employed in a reflection-mode device by depositing it on a stair-step-approximated, blazed grating. The periodic nature of the device contains the reflected beam within discrete, angular orders. The proof-of-concept device is modeled, tested and analyzed to explain its observed performance. Angular control of up to 1.2 degrees has been experimentally demonstrated. This approach promises simplicity of design and fabrication without the fringing field affect of LCs, allowing larger, discrete angular control. Moreover, the underlying fabrication is less expensive and can more easily be scaled to larger areas.</p>					
15. SUBJECT TERMS beam steering, phased arrays, gratings (optics), optical switching, differential thermal analysis					
16. SECURITY CLASSIFICATION OF:			17. LIMITATION OF ABSTRACT	18. NUMBER OF PAGES	19a. NAME OF RESPONSIBLE PERSON
a. REPORT	b. ABSTRACT	c. THIS PAGE			Guna S. Seetharaman, PhD (ENG)
U	U	U	UU	122	19b. TELEPHONE NUMBER (Include area code) (937) 255-6565, ext 4612 (Guna.Seetharaman@afit.edu)